FABRICATION AND ELECTRONIC TRANSPORT PROPERTIES OF UNDERDOPED HIGH TEMPERATURE SUPERCONDUCTOR NANOWIRES

BY

JOSEPH ANTHONY BONETTI

B.S., Georgia Institute of Technology, 1996
M.S., University of Illinois at Urbana-Champaign, 2000

THESIS

Submitted in partial fulfillment of the requirements
for the degree of Doctor of Philosophy in Physics
in the Graduate College of the
University of Illinois at Urbana-Champaign, 2002

Urbana, Illinois

FABRICATION AND ELECTRONIC TRANSPORT PROPERTIES OF UNDERDOPED HIGH TEMPERATURE SUPERCONDUCTOR NANOWIRES

Joseph Anthony Bonetti
Department of Physics
University of Illinois, 2002
Dale J. Van Harlingen, Advisor

In order to help unravel the mysteries surrounding the superconducting and pseudogap states in the high-T_c cuprates, we have measured the electronic transport properties of underdoped, high-T_c nanowires and nanostructures. The sizes of the samples involved allow for the investigation of the electronic structure on a mesoscopic length scale. We have measured current-voltage characteristics, resistivity, and critical current density all as a function of temperature, width, and orientation relative to the crystal axes. The resistivity displays large fluctuations within a temperature regime from T_c to ≈ 200K, and the current-voltage characteristics exhibit hysteretic steps. These features are difficult to explain within the context of known models and may indicate the presence of intrinsic inhomogeneities, charge stripes, or other electronic domain structures that have been proposed for the cuprates.

To my parents and grandparents whose support and encouragement made all of this possible

Acknowledgements

First and foremost a special thanks goes to my research advisor, Professor Dale Van Harlingen. The work for this thesis would not have been possible without the guidance, support, insight and friendship he provided over the last several years. I thank Professors Mike Weissman, Eduardo Fradkin, and Mohit Randeria for discussions, suggestions, and theoretical collaboration. I also thank Weissman for serving as a co-advisor while Dale was away on sabbatical leave. An important thanks also goes out to Tony Banks for his continual help and support with using and repairing lab equipment.

The number of people I have met over the years who have impacted my life is quite large. In addition to those friends and colleagues listed above, I thank the following friends who are all fellow members of the DVH research group (past and present): Bill Neils, Trevis Crane, Sergey Frolov, Britton Plourde, Brian Yanoff, Joe Hilliard, Kevin Osborn, Mark Wistrom, Jack Sadleir, Francoise Kidwingira, Madalina Colci,Micah Stoutimore, Martin Stehno, and Adele Ruosi.

I would like to thank the following list of friends, many who are fellow scientists: Brian Wiemeyer, Dylan Smith, Maria Hernandez, Yung Tae Kim, Valentin Prisecaru, Sorin Lazar, Lia Kaplan, Peter Ellis, Liz Shefter, Emily Wee, Nathan and Jessa Ovitt, Greg Snyder, Kevin Paul, Yu Wen Huang, Paul Voyles, and finally all members of the bands I have been a part of: The Conduction Band, Lotrel, and Trademark.

Finally I would like to thank and acknowledge those institutions that funded this work and made it all possible. This project was funded by the U.S. Department of Energy, Division of Materials Sciences Award No. DEFG02-91ER45439. I would also like to thank the UIUC Center for Nanoscale Science and Technology for fellowship support.

Contents

List of Figures

Chapter 1

Introduction to Conventional and High Temperature Superconductivity

1.1 Introduction and History

Superconductivity is an amazing phenomenon in which the laws of quantum mechanics make themselves macroscopically observable. The phenomenon is defined by two features. One is perfect conductivity, or truly zero electrical resistivity. Two is perfect diamagnetism, the ability to exclude and expel magnetic flux. To date, superconductivity only occurs when a material is cooled below a phase transition temperature, T_c, which ranges from a few milliKelvin to about 135 Kelvin (K) depending on the material. Superconductivity is not rare, or only existent in synthetic materials. In fact roughly half of the pure elemental metals, such as lead, aluminum, and tin are superconductors.

The first property of superconductivity (SC), zero resistivity, was discovered by Kamerlingh Onnes [1] in 1911 shortly after he successfully liquified helium. The material in which he observed SC was pure mercury with a T_c of 4.15 K. This event gave birth to an entire subfield of condensed matter and fundamental physics. Twenty-two years later, the second defining property, perfect diamagnetism, was discovered by Meissner and Ochsenfeld [2] and is known as the Meissner Effect. Over years and decades of study, researchers have discovered more and more SC's with higher and higher $T_c's$. In 1986 a new class of intriguing SC's with considerably higher $T_c's$ was discovered. These are known as the high temperature or high-T_c superconductors.

1.2 Phenomenology and Theory

Early models of SC were phenomenological and assumed two types of charge carriers, super electrons, and normal electrons. These are the so called two-fluid models. In 1957, Bardeen, Cooper, and Schrieffer created a successful microscopic theory of SC, the BCS theory [3]. Cooper was able to demonstrate the Fermi sea of electrons is unstable in the presence of a net attractive interaction between electrons. The BCS theory predicted an interaction of electrons with lattice excitations known as phonons. The result of this electron-phonon interaction is an effective attractive interaction between electrons near the Fermi level. After many experimental verifications of BCS theory it became clear that the super electrons from the two-fluid models are in fact pairs of electrons now called Cooper pairs. These pairs are Bosons and thus the SC state can be thought of as a Bose condensate of Cooper pairs. This condensate can be represented by a superfluid wavefunction, or order parameter given by,

$$\Psi(r,\phi) = \Psi(r)e^{i\phi(r)} \tag{1.1}$$

where the quantity $\Psi^*\Psi$ is the density of Cooper pairs, or the superfluid density, and ϕ is the phase of the wavefunction. For a superconductor, the current is a supercurrent, J_s. The supercurrent turns out to have the same form as the probability current density from quantum mechanics.

$$\mathbf{J_s} = \frac{ie\hbar}{2m_e}(\Psi^*\nabla\Psi - \Psi\nabla\Psi^*) \tag{1.2}$$

One of the defining properties of superconductivity involves the response to a magnetic field. When a magnetic vector potential $\mathbf{A}$ is present the momentum operator has an extra term and is given by $\hat{p} = -i\hbar\nabla + q\mathbf{A}$. This modifies the supercurrent expression and gives

$$\mathbf{J_s} = \frac{ie\hbar}{2m_e}(\Psi^*\nabla\Psi - \Psi\nabla\Psi^*) - \frac{2e^2}{m_e}\Psi\Psi^*\mathbf{A}. \tag{1.3}$$

If the wavefunction is a product of amplitude and phase then Equation (1.3) simplifies to

$$\Lambda\mathbf{J_s} = -(\frac{\hbar}{2e}\nabla\phi + \mathbf{A}) \tag{1.4}$$

where Λ is the London parameter given by $\Lambda = m_e/(n_s e^2)$, and n_s is the density of Cooper pairs, $\Psi^*\Psi$.

By taking the curl of Equation (1.4) and remembering the curl of a gradient is zero, an expression relating $\mathbf{J_s}$ and $\mathbf{B}$ is obtained

$$\nabla \times (\Lambda\mathbf{J_s}) = -\mathbf{B} \tag{1.5}$$

Equation (1.5) is known as the London equation (or by some as the 2nd London equation). It is analogous to Ohm's law and shows that a steady magnetic field rather than an electric field creates a steady supercurrent.

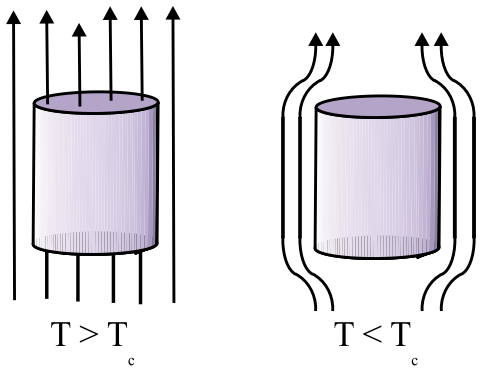

Figure 1.1: For $T > T_c$ field penetrates the material. For $T < T_c$ the field is expelled because a supercurrent flows on the surface which creates a field that exactly cancels the applied field.

Using Ampere's law and the London equation the Meissner effect can be derived. Ampere's law is given by

$$\nabla \times \mathbf{B} = \mu_o J \tag{1.6}$$

Taking the curl of Equation (1.6) and using Equation (1.5) a screening equation can be obtained after some vector calculus identities are used. This screening relation is given by

$$\nabla^2 \mathbf{B} = \mathbf{B}/\lambda^2 \tag{1.7}$$

where λ is known as the London penetration depth. Equation (1.7) shows that magnetic field only exists on the surface of a superconductor and decays exponentially with the decay constant λ. Typical values of λ range from about 30 nm to 1μm. A similar expression can be derived for the supercurrent, $\mathbf{J_s}$, showing it also exists only near the surface. The supercurrent flows in such a way as to create a field that opposes and exactly cancels the applied field, making the net field in the interior of a superconductor exactly zero. This process is shown in Figure 1.1. Of course this field screening can only occur up to some threshold value of applied field. If the applied field gets too large, it becomes energetically favorable for the superconducting state to vanish. This field value is known as the critical field, H_c.

If flux is applied to a superconducting ring an interesting result is obtained. Since the resistance of the ring is zero, the electric field, $\mathbf{E}$, deep inside is zero. Faraday's law states

$$\oint \mathbf{E} \cdot d\mathbf{l} = -\frac{d\Phi}{dt} \tag{1.8}$$

where Φ is the magnetic flux. Since $\mathbf{E}$ is zero, $d\Phi/dt$ is also zero. Thus it follows that the flux through a ring of superconducting material remains constant. The surface supercurrent will flow in such as way as to make this possible. Given this result, it is clear that flux can be trapped inside of a superconducting loop.

Not only is the flux in a SC loop constant, it is quantized. If a line integral of $\nabla\phi$, the gradient of the wavefunction's phase, is performed around the loop one gets a quantized condition due to the single valued nature of Ψ.

$$\oint \nabla\phi \cdot d\mathbf{l} = \oint (\mathbf{A} + \Lambda \mathbf{J_s}) \cdot d\mathbf{l} = \frac{2\pi\hbar n}{2e} \tag{1.9}$$

The flux quantum, Φ_o, is defined as $\Phi_o = \hbar/2e$. (Note that actually it is the term $(\mathbf{A} + \Lambda \mathbf{J_s})$, called the fluxoid which is quantized. In most cases this is equivalent to the flux itself being quantized).

Long before the BCS theory was developed, V.L. Ginzburg and L.D. Landau [4]provided a phenomenological model of superconductivity which was an extension of their earlier work on phase transitions. This model, known as the Ginzburg-Landau(GL) theory, is still used today since it is useful for describing how the superconducting wavefunction (order parameter) behaves in different environments (near interfaces, in fields, etc...). Amazingly this model was able to reproduce exactly Equation (1.3). Thus the GL theory was able to predict and calculate the penetration depth. Since the GL theory describes how the order parameter behaves, it has another characteristic length scale, ξ known as the GL coherence length. This characteristic length is the minimum distance over which spatial changes in the order parameter $\Psi(r, \phi)$ can occur. The ratio of the London penetration depth, λ, to the GL coherence length, ξ, turns out to be an important parameter which distinguishes two types of superconductivity.

If λ is smaller than ξ, then the free energy of the surface associated with a superconducting/normal interface is positive. Thus, when a magnetic field of sufficient strength is applied the material tries to minimize the normal/superconductor contact surface area. This usually results in the superconducting state vanishing everywhere in the sample at once. However, depending on the demagnetization factor, large normal/superconducting regions may form. In this case the system is in a phase known as the intermediate state. If $\lambda < \xi$, the material is called a Type I superconductor.

If $\lambda > \xi$, the free energy of the normal/superconducting surface is negative. In this case, the system tries to maximize this surface area. As a result, when a field is applied the superconductivity does not vanish everywhere at once, but instead forms tiny normal channels through which flux can penetrate. These channels have one quantum of flux, Φ_o, and are known as vortices (one is called a vortex). The core size of a vortex is roughly ξ, and supercurrent flows around this core extending out to a radius of roughly λ. If $\lambda > \xi$, the material is called a type II superconductor. For a type II superconductor, two critical fields exists. The field at which a single vortex forms is called the lower critical field, H_{c1}. The field at which the vortex density gets so large that the system prefers to exit the superconducting state is called the upper critical field, H_{c2}. For fields $H_{c1} < H < H_{c2}$, the system is in what is called the mixed state, or Schubnikow phase. An entire subfield of superconductivity is devoted to the study of vortices and vortex dynamics.

1.3 The Josephson Effects

A remarkable phenomenon occurs when two superconductors are coupled together by a thin, non-superconducting barrier. Amazingly a supercurrent (current with no voltage) can flow across the entire structure. Such a structure is known as a Josephson junction [5]. A supercurrent can flow because Cooper pairs are able to coherently tunnel from one superconductor to the other. This process, called the dc Josephson effect is described by the following relation,

$$I_s = I_c sin(\phi_2 - \phi_1) \tag{1.10}$$

where ϕ_i are the phases of the two superconducting order parameters and I_c is critical current, the maximum supercurrent that can flow through the junction. The phase difference across the junction obeys the relation

$$V = \frac{\hbar}{2e}\frac{\partial(\Delta\phi)}{\partial t} \tag{1.11}$$

where $\Delta\phi = \phi_2 - \phi_1$. Integrating Equation (1.11), assuming a constant applied voltage V, and inserting the result into Equation (1.10) produces an oscillating supercurrent given by

$$I_s = I_c sin(\frac{2eV}{\hbar}t + \phi_o) \tag{1.12}$$

The result, Equation (1.12), shows that an ac supercurrent can be obtained by applying a dc voltage. This is called the ac Josephson effect.

In practice there are many types of Josephson junctions. The non-superconducting part of the junction can be an insulator, a normal metal, a superconducting constriction in width of less than coherence length, a grain boundary, or several other possibilities. Fascinating and useful devices known as **S**uperconducting **QU**antum **I**nterference **D**evices, or SQUIDS, can be fabricated by putting one or more Josephson junctions in a superconducting loop. In this situation one can macroscopically observe quantum interference. Such devices are useful for measuring and detecting extremely small magnetic fields.

1.4 High Temperature Superconductivity

In 1986 a new class of superconductors known as the cuprates or high temperature (high-T_c) superconductors was discovered by Bednorz and Muller [6]. The first such material was $La_{1.85}Ca_{0.15}CuO_4$ with a transition temperature (T_c) of 30 K. This T_c was already high enough to suggest the material may not fit the standard BCS model of superconductivity. In just a few years researchers were able to make cuprates with higher and higher T_c's. Today there are many cuprates with $T_c's$ exceeding the boiling temperature of liquid nitrogen

(77 K) and even some exceeding 100 K. The record to date is $HgBa_2Ca_2Cu_3O_{8+\delta}$ with $T_c = 150K$ under high pressure.

The creation of these materials has sparked a revolution in superconductivity research. However, despite fifteen years of intense research many important questions about the cuprates remain unanswered. The most difficult question appears to be the superconducting mechanism. To date, a successful microscopic theory of superconductivity has not been developed for the cuprates. Other unanswered questions involve the non-superconducting phases. In fact one of the major difficulties in understanding superconductivity in the cuprates is that our understanding of the normal state is not on firm ground. Many feel a successful model of the cuprate normal state is needed before the superconducting state can be explained. However, explaining the normal state seems to be nearly as big a challenge as explaining the superconducting state.

Chapter 2

Properties of the Cuprates

2.1 Structural Properties

All of the cuprates have a stacked perovskite-like crystal structure. The term perovskite comes from the Russian mineralogist, Perovski, for whom the mineral $CaTiO_3$ is named. Perovskite is not only a nickname for the mineral $CaTiO_3$, but also for the crystal structure of $CaTiO_3$. Compounds with this crystal structure are loosely categorized as perovskites. Many interesting materials such as ferroelectrics, manganites, and skutterudites also have this structue. Unfortunately materials with this structure tend to be ceramic-like and brittle, posing a challenge to those trying to make high-T_c wires and other flexible structures. An ideal, cubic, perovskite structure ABX_3 is shown in part A of Figure 2.1. The anion, X, and cation A have large atomic radii and determine the size of the structure. The B cation has smaller atomic radius and has six anion neighbors forming an octahedron. The structure has BX_2 planes separated by AX planes. The cuprates are similar with CuO_2 planes corresponding to the BX_2 planes and SrO or BaO corresponding to the AX planes. The cuprates are complex, tetragonal instead of simple cubic and thus are not true pervoskites, but perovskite-like.

There are many features in the cuprate structure which are present in the perovskites. Most importantly, we have CuO_2 planes lying in the a-b plane, with a simple square lattice. Secondly, the CuO_2 planes in the a-b plane are sandwiched between interleaving AX planes such that the oxygens in the AX planes coordinate the Cu atoms of the CuO_2 planes as in the perovskites. Finally, we have a rectangular array of large radius cations and anions in contact with smaller radius cations which occupy the interstices. The crystal structure of the material studied for this thesis, $YBa_2Cu_3O_{7-x}$ (YBCO) is shown in part B of Figure 2.1.

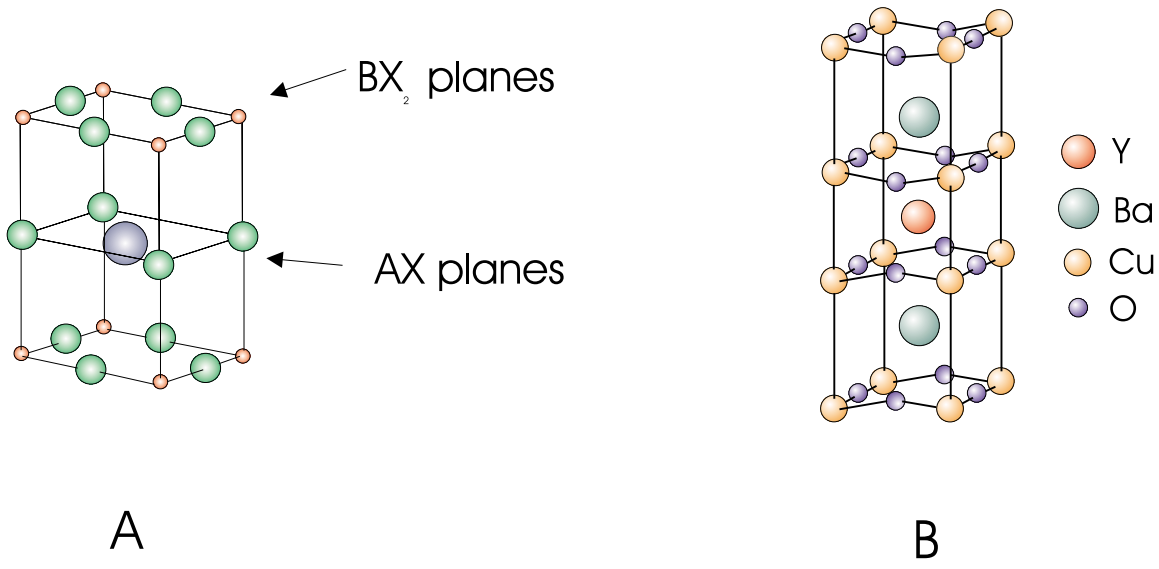

Figure 2.1: (A) The perovskite crystal structure ABX_3. (B) Crystal structure of YBCO. The CuO_2 planes correspond to the BX_2 planes and the BaO planes to the AX planes.

2.2 Superconducting Properties

In addition to having high T_c's the cuprates have other interesting superconducting properties. They are highly type II with extremely large H_{c2}'s ($> 100T$), very small coherence lengths ($\approx 1 - 3nm$) and large penetration depths ($\approx 100 - 500nm$). As mentioned the cuprates are Perovskite-like containing CuO_2 planes. Experiments and theory have shown the superconductivity in the cuprates is 2-dimensional and occurs only in these planes. The superconductivity in the c-direction (plane to plane) is believed to occur via Josephson tunnelling. Thus the superconducting properties are highly anisotropic with the in-plane (a or b direction) properties varying considerably from the inter-plane (c-direction) properties. For instance the coherence lengths, penetration depths, critical current densities, and critical fields, can have substantially different values.

Perhaps the most intriguing property of the cuprates is the nature of its order parameter. It is highly anisotropic within the a-b plane. Within the plane the order parameter has 4 nodes, 4 lobes, and a sign change in the phase when going from lobe to lobe. Since the c-direction superconductivity occurs via Josephson tunnelling, no true c-direction order parameter exists. Such an order parameter was predicted theoretically [7, 8, 9] and the experimental verification [10, 11] of this order parameter narrowed down the possible mechanisms for superconductivity in the cuprates. An order parameter of this form is known as d-wave. The name is an analogy borrowed from the orbitals of the hydrogen atom. Conventional superconductors have an isotropic, constant phase order parameter and are known as s-wave. The d-wave and s-wave order

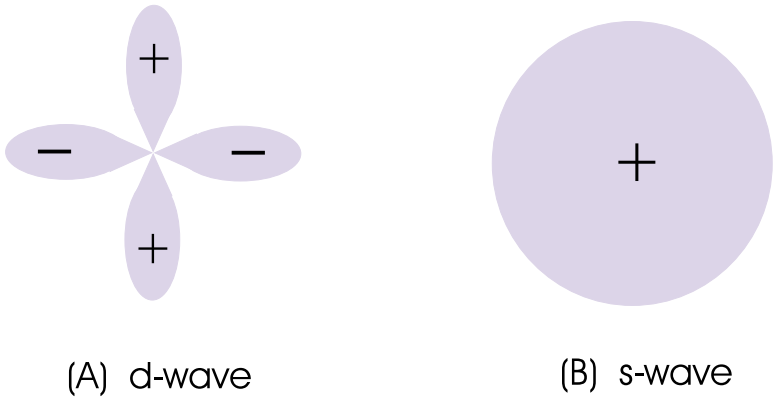

Figure 2.2: (A) K-space diagram of a d-wave order parameter, showing nodes, and a sign change in the phase. (B) K-space diagram of an s-wave order parameter, has constant magnitude and phase.

parameters are shown schematically in Figure 2.2.

2.3 Doping and the Cuprate Phase Diagram

In order for the cuprates to become superconducting they must be doped. The dopant atoms are normally in the interleaved SrO or BaO layers instead of the CuO_2 planes. These dopants are either cations with a different valence, or oxygen vacancies. In most cases the SrO or BaO layers are ionic and have no free carries. Thus the extra charge from the dopants is taken up in the CuO_2 planes as an effective change in the Cu valence. In YBCO, the interleaving layer with the structure $(BaO)(CuO_x)(BaO)$ also contains Cu. In this case the doping is altered by changing the O concentration in the CuO_x layers. This structure also has CuO chains lying along the b direction.

The cuprates have an amazing spectrum of properties as one spans the temperature versus doping phase diagram. This phase diagram is shown in Figure 2.3. In the extremely low doping side of the phase diagram the material is an antiferromagnetic (AF), Hubbard-Mott insulator with a Neel temperature of a few hundred Kelvin. As the doping is increased a superconducting state with very low T_c is seen. The T_c rises with increasing doping, levels off, then begins to decrease with increasing doping, forming a dome in the phase diagram. Above T_c the system can be in a variety of phases, depending on the doping. Above T_c, and for low dopings the system is in what is known as the pseudogap (PG) regime. The PG is an intriguing state whose characteristics will be discussed at length later in this thesis in chapter 3. Some theories and experimental data suggest the existence of a second crossover within the PG into another state, shown by the dashed line in Figure 2.3.

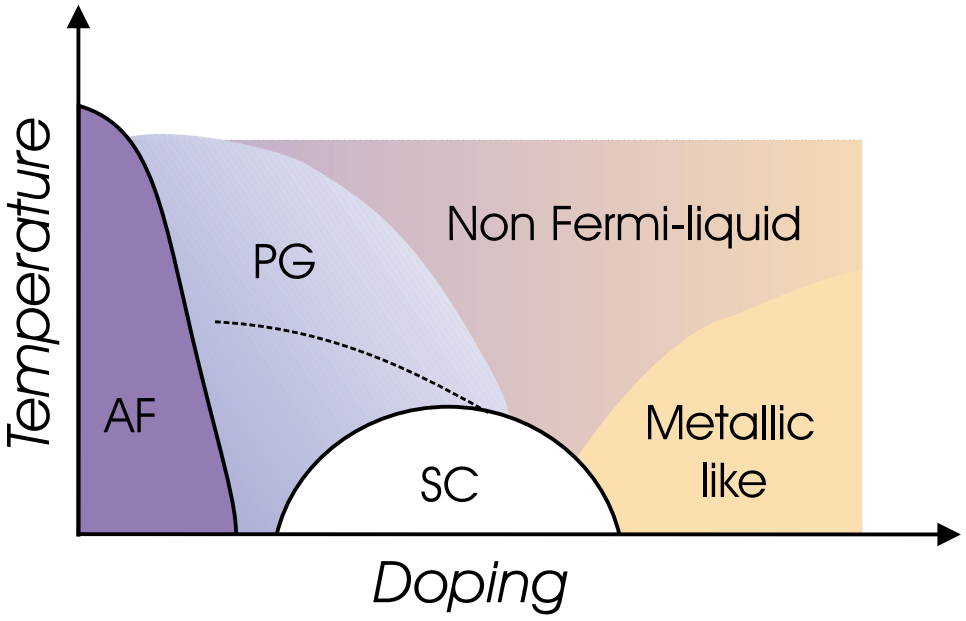

Figure 2.3: Temperature versus doping phase diagram for the cuprates

As the doping increases the material exits the PG state, and enters a non-Fermi-liquid state. This state is not as puzzling as the PG, but still far from ordinary. Finally, for the overdoped regime, the system enters a metallic-like state, which is a little more ordinary but still not perfectly understood. The general consensus is that as the doping increases the system behaves more and more metallic. There are many slight variants of this phase diagram used in the community. Most of these differences are simply disagreements about where in doping the above-T_c phases begin and end. However, it is generally agreed upon that these phases exists.

2.4 Electronic Structure

The carrier density in the cuprates is quite low, similar to semi-metals such as bismuth. This low carrier density leads to an increased importance of the Coulomb interaction between electrons. At high carrier densities as in a metal, the electron states are extended and exist throughout the sample. However, at low densities these states become more and more localized due to Coulomb repulsions from neighboring electrons. For an electron spacing of r the Coulomb interaction energy is given by

$$U = \frac{e^2}{4\pi\epsilon_o r} \tag{2.1}$$

and the kinetic term by

$$K = \frac{\hbar^2 k^2}{2m} \sim \frac{\hbar^2}{2mr^2}. \tag{2.2}$$

At low densities r is larger and since the Coulomb term goes as $1/r$ it dominates. This low carrier density leads to an insulating state because the carriers are trapped in Coulomb barriers. This state is known as a Mott insulator. At high densities r is smaller and the electrons have enough kinetic energy to tunnel through the Coulomb barriers. The competing terms in Equation (2.1) and Equation (2.2) are described in the Hubbard model with the following Hamiltonian.

$$\mathcal{H}_{Hubbard} = -t \sum_{i,j,\sigma} c^{\dagger}_{i\sigma} c_{j\sigma} + U \sum_{i} n_{i\downarrow} n_{i\uparrow}. \tag{2.3}$$

The first term is simply a tight-binding, independent-electron-model term, where t is the overlap integral of states on sites i and j. This term creates an electron at site i with spin σ and removes an electron at site j with spin σ. The second term is simply the Coulomb term. It adds energy U when electrons with opposite spin occupy the same site, i. If $U = 0$ the standard tight-binding approximation applies. In this case a well defined Fermi surface exists and the standard Fermi-liquid picture holds. If $U \gg t$ and there is one carrier per site, an insulating, AF state with localized magnetic moments arises. In intermediate regimes where, $U \approx t$ or where one term is not dominant the solution gets more complicated. At low dopings the system can form what are known as Hubbard bands. In this scenario there is mobility of charges in the form of hopping. Some researchers feel a Hubbard-band-like transport occurs in the cuprates. It is currently under debate whether the cuprates are Hubbard-band-like or whether a modified Fermi liquid picture is correct. The single Hubbard band model is too simple but is useful for demonstrating the electronic structure debate in the cuprates. Most Hubbard models for the cuprates incorporate multiple Hubbard bands.

It is known that the superconducting cuprates lie very close to the AF Mott insulator transition. Unfortunately, it is for this doping level that theories tend to be the least well developed. The true nature of the electronic structure in this regime is not known. Is there a gradual transition from Hubbard-band-like behavior to a Fermi liquid as the doping increases? Or does the system form an inhomogeneous microstructure with some regions Hubbard-band-like and others Fermi-liquid-like? Could the system form domains of coexisting metallic and semi-metallic regions or even conducting and insulating regions? The experiments carried out for this thesis study exactly this issue by probing mescoscopic samples.

2.5 Above-T_c, Electronic Transport Properties

It should come as no surprise that there are many controversies and mysteries associated with the above-T_c transport in the cuprates. The transport is quite unusual and no particular model at this time is accepted as being correct. Unfortunately, experiments seem to be contradictory, leaving theorists with no particular guidelines.

The resistivity, ρ, of the cuprates in the non-superconducting state is strongly dependent on direction, doping, and of course temperature. As mentioned the cuprates are very planar with the charge carriers residing in the CuO_2 planes, the "a-b planes". This 2-D localization of charge carriers leads to a highly anisotropic resistivity. For most cuprates the resistivities in the $\mathbf{a}$ and $\mathbf{b}$ directions are nearly the same (in YBCO $\rho_a \approx 2\rho_b$). However ρ_c is typically higher than ρ_{ab} by an order of magnitude or more. This anisotropy factor between ρ_{ab} and ρ_c can vary enormously. For YBCO it is ≈ 10, while in BSCCO it is $\approx 10^5$. The conduction in the c-direction for intermediate anisotropy factor occurs via tunnelling and is linear with T for many cuprates. However for some cuprates with very large anisotropy ρ_c increases with decreasing temperature suggesting semiconducting or hopping behavior.

The resistivity in the a-b plane for cuprates having optimum or near optimum doping varies linearly with T and at first glance appears similar to that of a typical metal. The well known expression for the conductivity in a metal is given by

$$\sigma = \frac{ne^2\tau}{m^*} \tag{2.4}$$

where n is the carrier density and τ is the scattering relaxation time. For a metal n is independent of T and since $\rho_{metal} \sim T$ this implies that the scattering rate, $1/\tau$ varies linearly with T. In the optimally doped cuprates the linear resistivity is more difficult to explain. The carrier density and sign of the charge carriers can be obtained by measurements of the Hall coefficient, $R_H = 1/ne$. For most cuprates R_H is positive and the carriers are doped holes. Interestingly these measurements show that R_H varies linearly with T implying that the scattering rate is proportional to T^2 rather than T.

The resistivity of the cuprates is a strong function of doping. At optimum and near optimum doping the resistivity is linear. As the doping is decreased an upward curvature appears before T_c. Then for very low doping the material never becomes superconducting but instead becomes insulating at low temperatures. For the over-doped case the resistivity is always linear, and never has an upward curvature or insulating phase. An example of this doping dependent behavior is shown in Figure 2.4 The PG state mentioned earlier can also show up in the transport measurements. This will be discussed in the next chapter.

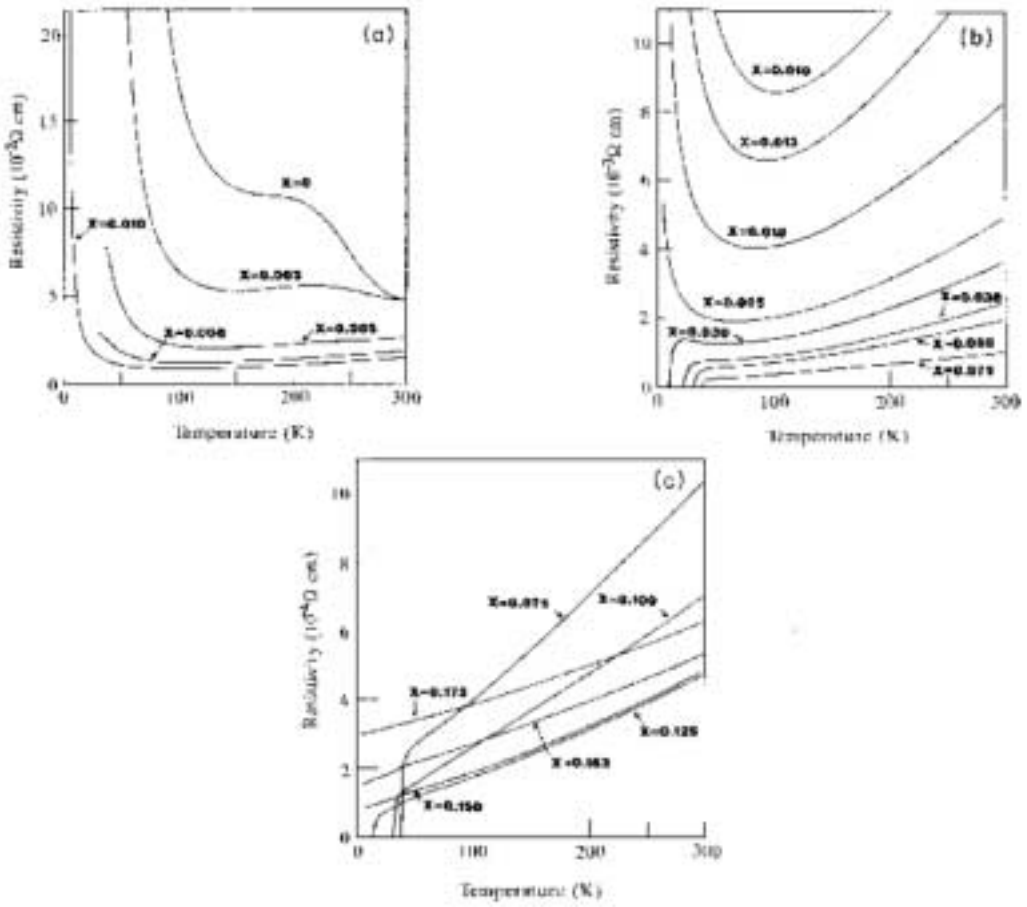

Figure 2.4: Resistivity vs Temperature over a large doping range for the cuprate $(La_{2-x}Sr_x)CuO_4$. (a) extremely underdoped, (b) underdoped to optimally doped, (c) optimally doped to overdoped.[12]

Chapter 3

The Pseudogap

3.1 Introduction and Definition

As mentioned in Chapter 1, the superconducting state is composed of a condensate of Cooper pairs. These pairs are created when normal electrons just above and just below the Fermi level feel a net attractive interaction. This pairing and condensation lower the energy of the system since electrons in states above the Fermi level lower their energy when they pair with the corresponding opposite momentum and opposite spin electron below the Fermi level. Excitations can occur that break pairs and promote the corresponding single particles back to the energies just above or just below the Fermi level. These single particle excitations are known as quasiparticles and are either electron-like or hole-like depending on whether they are just above or just below the Fermi level. There is a certain amount of energy required to break a pair and create these quasiparticle excitations. This energy is known as the superconducting energy gap since for energies less than this value quasiparticles cannot be created. It is analogous to a semiconductor energy gap where energies less than the gap energy will not excite a charge carrier from the valence band to the conduction band. For conventional superconductors this energy gap forms precisely at the superconducting transition temperature. Amazingly in the underdoped to slightly overdoped cuprates this energy gap seemingly begins forming at temperatures as high as $100 - 300$K above T_c, even though the sample is not superconducting! This phenomenon is known as the pseudogap. The microscopic origin of the PG is currently unknown. Although many researchers do feel a real superconducting energy gap begins to form at T^*, others do not think this is correct. Thus it should be stressed here, that a superconducting energy gap **seemingly** begins to form at T^*.

Perhaps the most powerful and easiest to understand technique for probing the energy gap in conventional superconductors is tunneling spectroscopy. This technique will be briefly described and results will

be shown for a conventional superconductor. The results for the cuprates will then be shown for comparison. By seeing these two cases, an understanding of what is meant by ”pseudo”-gap will become clear.

3.2 Tunneling Spectroscopy; an Illustrative Experimental Technique for Explaining the Pseudogap

In tunneling spectroscopy an oxide layer is grown on a superconductor and then coated with a normal metal. This forms what is known as a superconductor/insulator/normal (SIN) junction. In equilibrium the Fermi levels of the superconductor and normal metal will equalize as shown in part A of Figure 3.1. In this case there are no empty states for electrons from the metal or the superconductor to tunnel into. If a bias voltage, V, is applied the Fermi level of the normal metal can be adjusted. For voltages, $-\Delta/e < V < \Delta/e$ there is no conductance, due to the gap. If $V > \Delta/e$ electrons from the normal metal can tunnel into the empty states of the superconductor. Or if $V < -\Delta/e$, electrons (or quasiparticles) can tunnel from the superconductor into the empty states of the normal metal. This process, shown in part B of Figure 3.1, results in large peaks in the conductance, dI/dV vs. V plot. A typical tunneling conductance curve is shown for a conventional superconductor in Figure 3.2.

In the underdoped to slightly overdoped cuprates the depression in the conductance between $\pm\Delta$ begins forming at temperatures very far above T_c. This is in stark contrast to the tunneling conductance for a conventional superconductor, in which the conductance is simply a flat line (Ohmic) above T_c. The temperature at which this depression in the conductance appears, or at which the gap seemingly begins to form, is known as the pseudogap temperature, T^*. It is unknown at present if this is a phase transition or just a crossover. An example of a conductance curve showing the formation of the pseudogap is shown in Figure 3.3.

3.3 Experimental Probes of the Pseudogap

In addition to tunneling spectroscopy many other experimental techniques have been used to probe and observe the pseudogap state. Each of these probes has a specific advantage and adds unique insight. A detailed description of all the techniques would be too lengthy. Thus a discussion of only those which are most important and/or relevant for this thesis will be addressed. These are, nuclear magnetic resonance(NMR), angular resolved photoemission spectroscopy(ARPES) and transport.

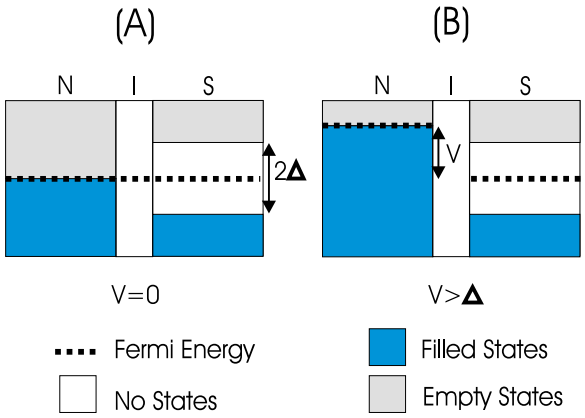

Figure 3.1: (A) For zero voltage, there are no states available for tunneling. (B) For $V > \Delta$ electrons in filled states from the normal metal can tunnel into empty states in the superconductor.

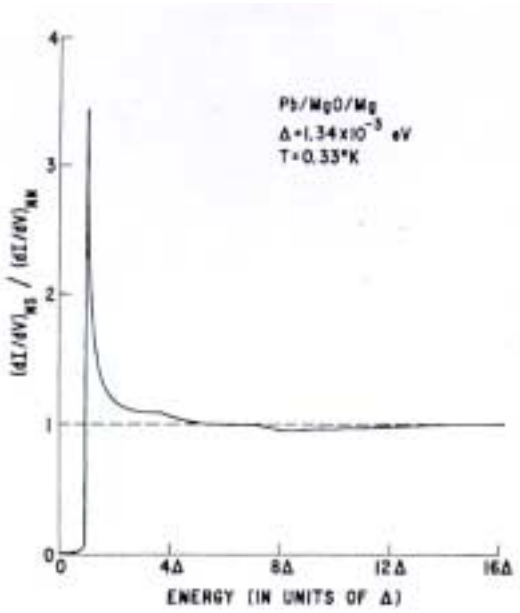

Figure 3.2: The normalized conductance, dI/dV, versus V for a Pb/MgO/Mg SIN junction. [13]

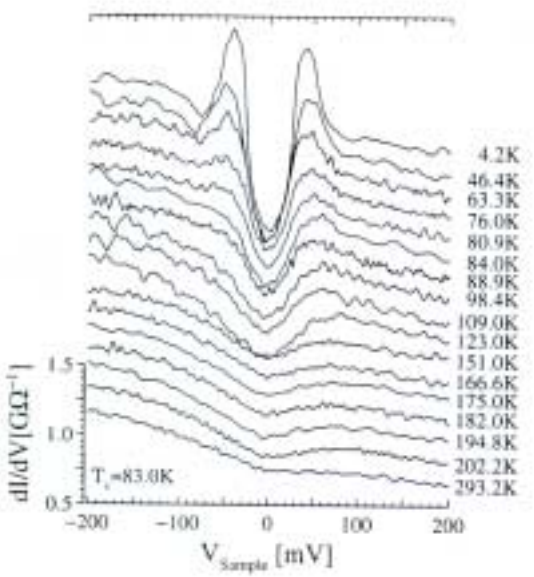

Figure 3.3: The conductance, dI/dV, versus V for underdoped BSCCO with a T_c of $83K$. The pseudogap begins forming well above T_c and even appears to be present at room temperature. [14]

3.3.1 NMR measurements of the Pseudogap

NMR provided one of the first experimental verifications of the BCS theory of conventional superconductors. It has proved to be useful in the study of the cuprates as well. In fact the first observation of the PG came from NMR. The two types of NMR measurements which have mainly been used to study the PG, are the Knight shift, K_s, and the spin-lattice relaxation time, T_1. The Knight shift refers to the change, or "shift" in the resonance frequency due to interaction of the nuclear spin with the spin of conduction electrons. The shift is named for Walter Knight, who first observed a difference in the resonance frequency of ^{63}Cu in metallic copper, and the copper in diamagnetic CuCl. T_1 is a measure of the time for the nuclear magnetic moment to relax back to its equilibrium value after being perturbed, or tipped away from being aligned with the static field. Both K_s and T_1 are quantities sensitive to the density of states. T_1 is also sensitive to AF fluctuations. These measurements are therefore well suited for investigating the PG regime.

NMR is unique and important for 3 major reasons. First, unlike many techniques which are sensitive to the charge channel, it is sensitive to the spin channel. In fact, since the the PG was discovered with NMR, it was originally called the spin gap. Second, NMR is one of the only techniques which shows the PG extending into the overdoped regime and not ending at optimal doping. And finally, NMR shows two clear crossover temperatures instead of one. The upper crossover temperature is called T^0 and the lower one T^*.

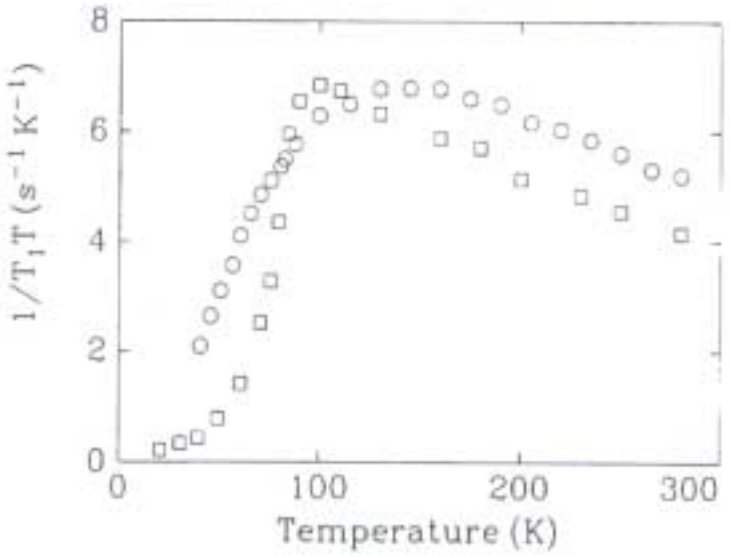

Figure 3.4: In plane ^{63}Cu spin $1/T_1T$ in optimally doped $YBa_2Cu_3O_{6.95}$ (squares) and underdoped $YBa_2Cu_3O_{6.64}$(circles). The PG causes a decrease in the relaxation rate well above T_c.[15]

Figure 3.4 and Figure 3.5 show the behavior of T_1 and the Knight shift for underdoped and optimally doped YBCO. In the optimally doped case, $1/T_1T$ increases as the AF spin coherence increases. Then right at or very near T_c a sudden drop occurs. However, in the underdoped case $1/T_1T$ levels off and begins to decrease about $100K$ above T_c. This decrease is attributed to the PG.

For the Knight shift an even more remarkable difference is seen between the underdoped and optimally doped samples. In Figure 3.5, the Knight shift in the optimally doped sample is temperature independent above T_c and then suddenly drops when $T = T_c$. The Knight shift in the underdoped sample gradually decreases with temperature and little to no change is seen at T_c. Measurements of the Knight shift also show the upper crossover temperature, T^0. This has been seen in the naturally underdoped compound $YBa_2Cu_4O_8$. Above T^0, K_s is temperature independent. At T^0, K_s changes behavior and decreases linearly with T. At the lower crossover temperature T^*, K_s changes behavior once again and decreases faster than linear with T. Many measurements of the PG have been performed with NMR over the last 10 years. If a catalog or summary of all the data is made, then a phase diagram can be produced. This has been done in a review article of the pseudogap [17]. This phase diagram is shown in Figure 3.6. It provides a good summary of the NMR data. The main features are two crossover temperatures and an extension of the PG into the overdoped regime.

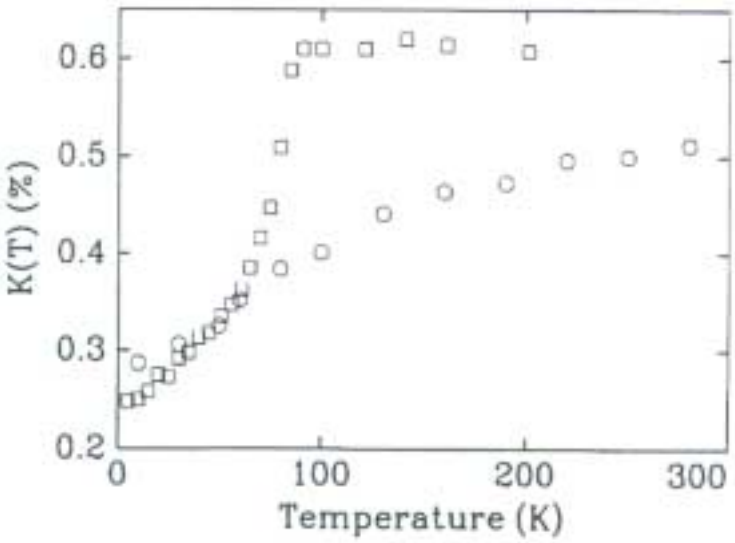

Figure 3.5: In plane ^{63}Cu Knight shift for $YBa_2Cu_3O_{6.95}$(squares) and $YBa_2Cu_3O_{6.64}$(circles). The normal state Knight shift is temperature independent in the optimally doped case but decreases with temperature in the underdoped case.[16]

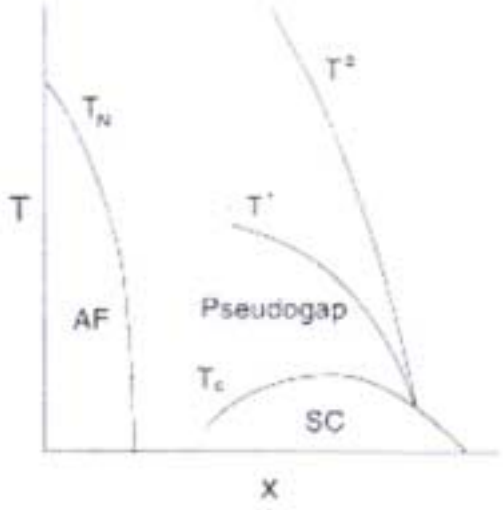

Figure 3.6: A phase diagram of the cuprates suggested from a catalog of NMR data.[17]

3.3.2 Angle Resolved Photoemission Spectroscopy

Angle-resolved photoemission spectroscopy (ARPES) is a refined version of the standard photoelectric effect. A beam of relatively high energy photons ($\approx 20eV$)impinges on the surface of a single crystal in ultra high vacuum. This causes photoelectrons to be ejected from the sample. The energy of these ejected electrons can be measured and used to determine the binding energy of the electrons by simply using the conservation of energy,

$$E_{kin} = \hbar\omega - E_{wf} - E_{bind} \tag{3.1}$$

where $\hbar\omega$ is the energy of the incident photon, E_{wf} is the work function of the material, and E_{bind} is the quantity of interest, the binding energy. The momentum of the electron parallel to the surface is conserved as it is ejected. By measuring this momentum, the momentum of the electron in the initial state can be deduced. This makes ARPES a perfect tool for mapping out the k-dependence of the electronic structure of materials.

ARPES has been used to map out the k-dependence of the SC gap in the cuprates. The result shows very clearly and convincingly that the gap magnitude follows that of a d-wave gap [18, 19, 20]. Amazingly, for the underdoped cuprates, a gap feature appears above T_c, and even more amazing is that this above-T_c gap has the same d-wave angular dependence as the SC gap [21, 22].

3.3.3 Resistivity

As discussed earlier, the resistivity, ρ, in the cuprates is a strong function of doping. For very low dopings the material does not become superconducting, but instead becomes an AF insulator at low temperatures. As the doping is increased the ρ vs. T curve has a large upward curvature, but eventually goes superconducting at low temperatures. When the doping reaches optimal this upward curvature disappears and the ρ vs. T curve is linear. For the overdoped case the curve remains linear. These features and doping dependence were shown back in Figure 2.4. Interestingly if the ρ vs. T curves are carried out to higher temperatures, as shown in Figure 3.7, the underdoped samples show a very clear change in slope. These slope changes are thought by many to be attributable to the PG. The same behavior is seen in $YBa_2Cu_3O_{6+x}$ but with a much lower PG crossover temperature. This is shown very nicely in the data from Ito et al. [24] in Figure 3.8. In both the $YBa_2Cu_3O_{6+x}$ and $La_{2-x}Sr_xCuO_4$ data the crossover temperature decreases with increasing doping consistent with PG behavior seen in other experimental probes.

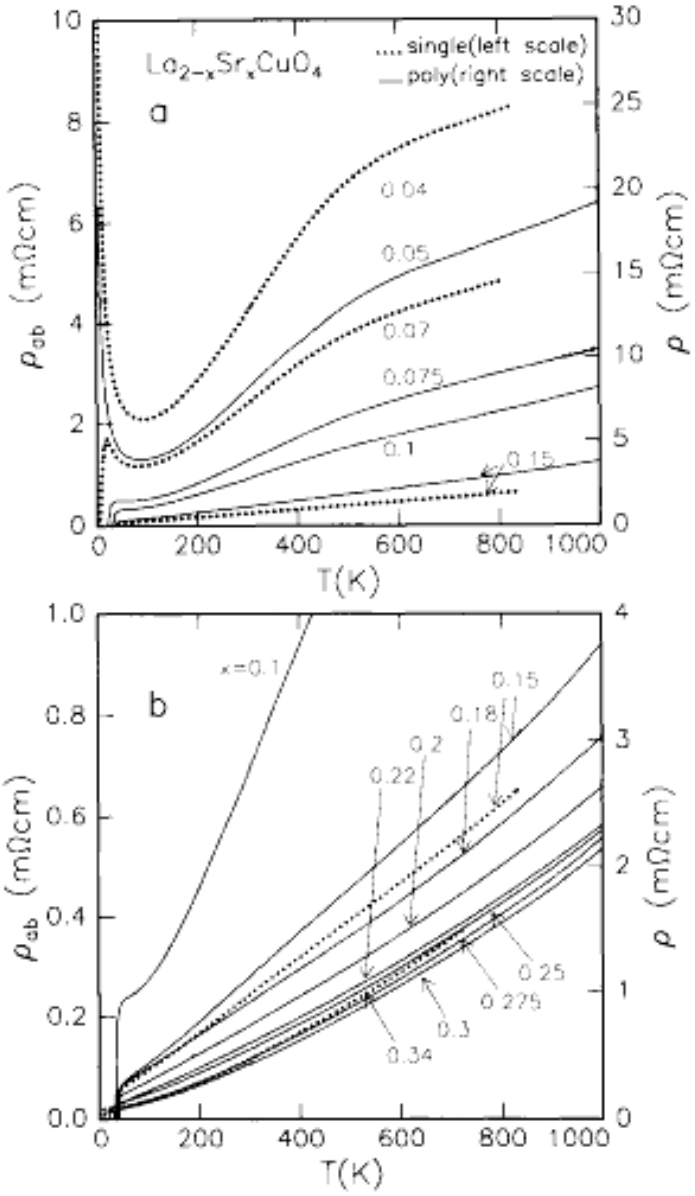

Figure 3.7: Temperature dependence of the resistivity of $La_{2-x}Sr_xCuO_4$ at various doping levels. Underdoped is shown in the top panel. Optimal and overdoped are shown in the bottom panel. In the underdoped samples a drop in the resistivity at high temperatures between 300-600 K is seen. This drop is thought by many to be from the formation of a pseudogap.[23]

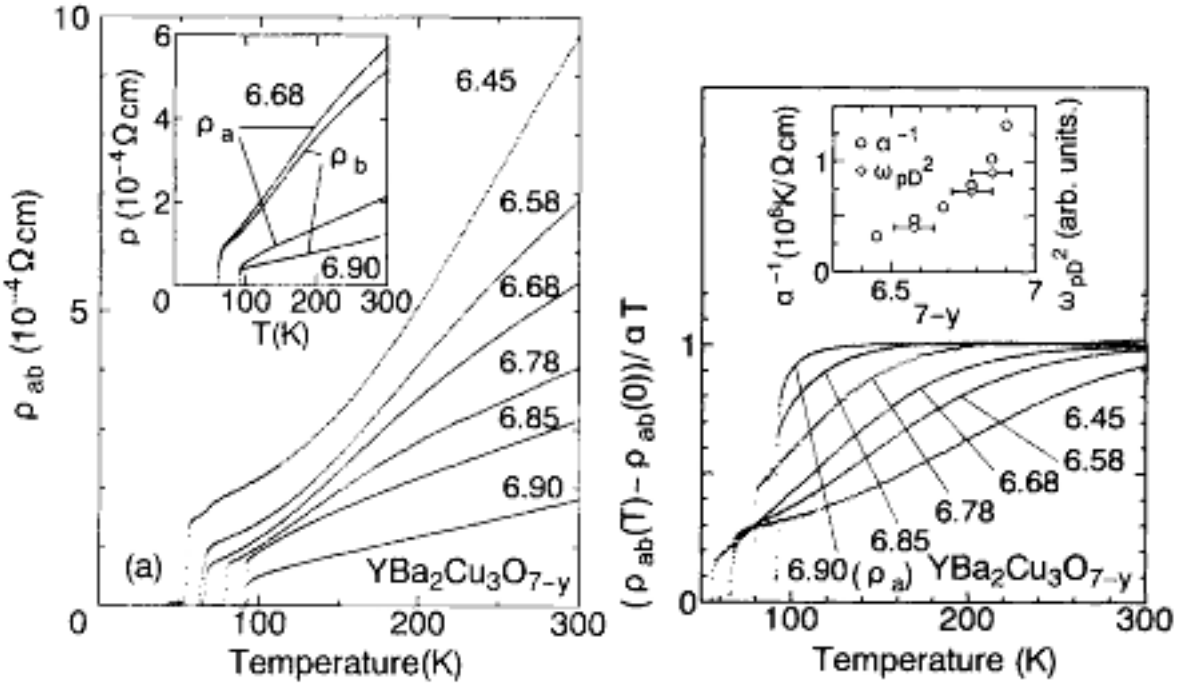

Figure 3.8: DC ρ_{ab} of $YBa_2Cu_3O_{6+x}$ at various doping levels. (A) shows the raw data (B) shows the normalized data which clearly displays a change at a crossover temperature between 100-300 K. [24]

3.4 Models of the Pseudogap

The PG exhibits features that are strikingly similar to a SC gap. It creates a depression in the conductance and density states, it shows up in NMR, transport, it has the same magnitude as the SC gap, and ARPES has even shown it has the same k-space angular dependence as the d-wave SC order parameter (OP). Thus, it is very tempting to say the PG is the above T_c formation of a real SC gap. This is exactly what many PG models propose. For superconductivity to occur over macroscopic lengths, the OP's magnitude must be non-zero everywhere, and equally important, the phase of the OP must be constant or smoothly varying. Many theorists [25, 26] asked, what would happen if the magnitude of the OP were non-zero everywhere, but the phase was fluctuating on short length scales such that phase coherence could not be established across the entire sample. The quantity, $\psi^*\psi$, where ψ is the OP magnitude gives the Cooper pair density. Therefore, models predicting a non-zero OP magnitude above T_c are referred to as pre-formed pairs, or pre-cursor SC models. The PG data presented thus far is consistent with the ideas of pre-cursor SC. However, other models have been developed that also explain the data. In addition there are some recent tunneling spectroscopy results that demonstrate the features from the PG and SC gap are distinct [27, 28]. These other models make more specific predictions such as, competing states, AF spin fluctuations, and types of nanoscale charge ordering, such as narrow conducting channels called stripes.

Most researchers feel an understanding of the PG is needed before a microscopic model of high-T_c superconductivity can be developed. As mentioned many other regimes in the cuprate phase diagram are also not well understood, making nearly the entire phase diagram a mystery. Thus, each model of the PG is a component or aspect of a larger model attempting to describe the entire phase diagram. These models are described in chapter 4.

Chapter 4

High-T_C Theories

4.1 Introduction

Explaining high-T_c superconductivity is one of the most, if not the most, difficult problem in condensed matter physics. It is perhaps also the most contentious. When a discovery with extreme fundamental and technological importance is made by complete surprise, researchers are more eager and more enthusiastic than normal to develop a theory. This high level of enthusiasm, combined with the emotions of those involved has created an intense competition between researchers.

The number of theories and models which have been created is far too large for even a cursory description of each. Fortunately a considerable number have been ruled out in recent years by several key experiments. These all involved measurements sensitive to the magnitude and/or phase of the order parameter (OP) and were able to demonstrate the OP is d-wave as shown in Figure 2.2. Theories that make predictions contradictory or inconsistent with a d-wave order parameter are thus effectively ruled out. There are a handful of researchers who still feel an s-wave approach is correct, in light of these measurements. Indeed, there are a few puzzling experiments which seem to contradict d-wave [29], but the number supporting and/or showing d-wave is far greater (too many to reference). Thus it seems highly unlikely the d-wave result will be overturned. For this reason, only those theories consistent with or predicting a d-wave OP will be discussed. High-T_c theory is a quickly evolving area of research. Therefore the models presented here are simply those that at present seem to have the most promise.

As mentioned in chapter 2 the electronic structure of the cuprates in the non-superconducting state is not well understood, or agreed upon. What is agreed upon is that as the doping increases the system becomes more and more Fermi-liquid-like. The undoped parent compound is an AF Mott insulator while for extreme overdoping, past the doping which can support SC, the system behaves like a Fermi-liquid. These opposite

ends of the phase diagram provide two starting points for theories. One can take the view that proximity to the AF Mott state is vital for SC. Or one can assume a type of modified Fermi-liquid state can produce SC, and that viewing the system as a doped AF, Mott insulator is not necessary.

Very generally this choice of Fermi-liquid-like, or doped Mott AF, defines two categories for theories. Both categories have models which are consistent with experiments probing the superconducting and pseudogap states. The validity and accuracy of models from each category is likely dependent on the doping, with the Fermi-liquid approach favoring overdoping, and the doped Mott AF approach favoring underdoping. Finally, nearly all the models contain an explanation of the anomalous above-T_c behavior and the pseudogap.

4.2 Doped Antiferromagnetic Mott Insulator Models

These models all start from the simple question: What happens when a Mott AF insulator is doped with holes? Are the holes distributed uniformly, or do they arrange and order themselves in a type of microstructure? Another key question is how the spins behave. One advantage the doped AF theories have is a natural explanation of why SC goes away as the doping increases. The modified FL models have a difficult time explaining the existence of SC at low doping.

4.2.1 RVB and Associated Models

An early, incorrect theory proposed by P.W. Anderson [30] in the late 1980's, called the resonating valence bond (RVB) model, has recently attracted much attention. Anderson received much criticism for the original model and he himself later thought it was incorrect. However, within the last few years (as of 2002) researchers have proposed modified versions of the original RVB idea, or models which incorporate some aspect of the basic premise behind the RVB idea [31, 32]. The undoped, parent compound for the high-T_C cuprates exhibits long range AF order. Anderson's proposal is that quantum fluctuations in a 2D system (the planes) might be strong enough to destroy the long range antiferromagnetism. However short-range AF would remain because the spins pair together in an antiparallel configuration. The state of each pair is then a superposition of two possible configurations, $|pair\rangle = \frac{|\uparrow\downarrow\rangle - |\downarrow\uparrow\rangle}{\sqrt{2}}$. In addition to each pair having two configurations, an ensemble of spins has many configurations depending on which spins pair. The system exists as a superposition of all these possibilities, and is known as a spin liquid. This is analogous to benzene, a molecule that exists in a superposition of two configurations for its double bonds. It is for this reason, Anderson's idea is called the resonating valence bond model. An artistic conception of the RVB model and

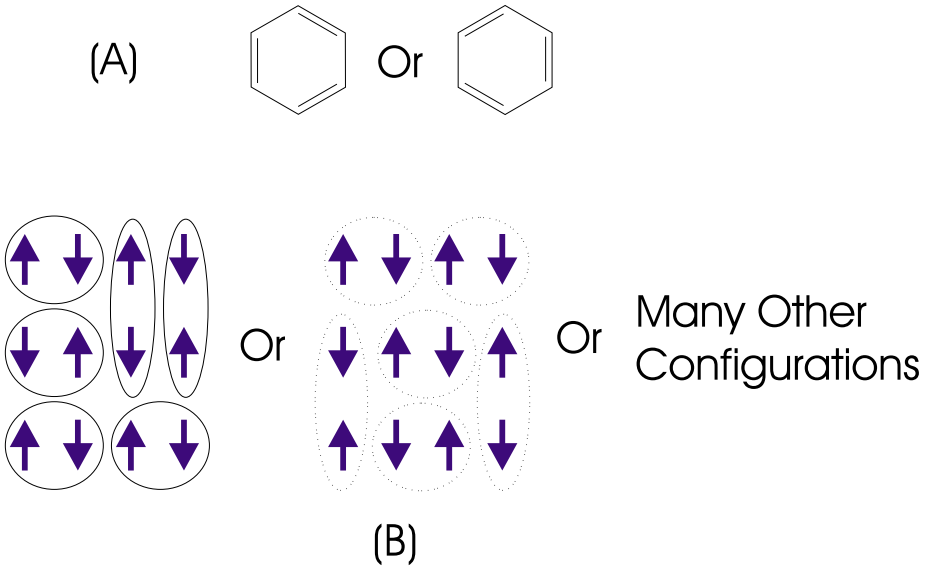

Figure 4.1: (A) The two states of the benzene molecule (B) The many configurations of spin pairs in the RVB model

the benzene analogy is shown in Figure 4.1. For the undoped material these spin pairs are trapped because no site can have two charges (no double occupancy). In others words the system is still a Mott insulator, but not one with long range AF order (Mott insulators need not be AF). When the material becomes doped with holes, motion of these spin pairs becomes possible. Interestingly the excitations in this doped spin liquid exhibit spin charge separation. There are excitons, called spinons which carry spin and have no charge, and others known as holons having charge and no spin. The holons are bosons and SC occurs via a Bose-Einstein condensation of the holons. Holons are not pairs but experiments in cuprates show flux quanta of $h/2e$ as opposed to h/e, suggesting pairs are still present. However this is not a problem for the RVB models since the motion of a holon corresponds to the motion of a bonded pair. The major problem with the RVB idea is that experiments were able to demonstrate clearly that the undoped parent compound did not behave as a spin liquid, but instead as an antiferromagnet with long range order. Recent models by Randeria et al. [31], Laughlin [32], and others incorporate the basic notion of the RVB spin liquid, while remaining consistent with experimental observations.

Laughlin's model, known as "Gossamer" superconductivity recognizes that the undoped parent compound is an antiferromagnet with long range order. But he proposes a weak, secondary type of antiferromagnetism distinguishable from the the first by a tiny background superfluid density. This superfluid density he proposes comes from regions that are RVB-like. The Gossamer model thus proposes that SC exists well

into the AF insulating phase, but cannot conduct because there is no long-range, SC order.

The model proposed by Randeria et al. is one which assumes d-wave BCS pairs. In the RVB model which had no reason to assume or propose a d-wave OP, an s-wave order parameter was chosen. The Randeria model combines d-wave pairing with RVB ideas and is able to naturally explain the pseudogap, and the superconducting dome in the phase diagram. In this model the pseudogap is simply the region or temperature at which spin pairing occurs. The destruction of SC as doping is decreased is explained as the trapping of pairs due to becoming more and more Mott like. A Mott insulator simply means that the Coulomb repulsion between carriers becomes extraordinarily high and no site can ever contain two charges. Mott insulators are a result of low carrier density and was explained in chapter 2. A Mott insulator does not require or imply long range AF. Long range AF occurs for other reaons. The Randeria model set out as its goal, understanding the cuprates at zero temperature for doping levels which create superconductivity. In the process it naturally explains the PG. The model does not ask what happens at doping levels small enough to create long range AF. This is not problem for the model since the phase diagram likely contains a region between the SC doping level and long range AF doping level. Thus there's no requirement for the low doping side of this model to produce long range AF. The long range AF can be explained for reasons unrelated to d-wave SC.

4.2.2 Stripe Models

These models, largely the work of Emery, Kivelson, Zaanen and Frakdin [33, 34, 35, 36] propose that when holes are doped into an AF lattice they line up in one dimensional entities known as charge stripes. The regions between the charge stripes remain AF. In such models all of the charge carriers reside in the stripes, and conduction occurs along the stripes. The existence of stripes sounds rather exotic. However, very simple arguments can be made demonstrating why they should form.

The motion of one hole in an AF cannot easily occur. It's motion leaves in its wake, an array of frustrated bonds that ruins the AF pattern. Thus one hole moving through the lattice is a highly frustrated, energetically unfavorable process. This can be seen in part A of Figure 4.2. In the early days of high-T_c it was thought that pairs of holes could easily travel through an AF lattice. However, this was disproved by Truggman [37]. Therefore the motion of holes through an AF lattice is also a frustrated, unfavorable process. Figure 4.1.

The AF lattice does not like the presence of holes and tries to eject them. If holes were neutral this would lead to a complete phase separation and the sample would have all the holes in one section, while the rest of the sample remained an AF Mott insulator. However, the holes carry electrical charge and the Coulomb energy inhibits a complete phase separation. The final result is a compromise between two competing

processes, hole ejection and Coulomb repulsion. This competition leads to the formation of stripes as shown in part C of Figure 4.2. Similar competing processes occur elsewhere in nature and do indeed produce stripes. Stripes are seen in Rayleigh-Benard convection, the mammalian visual cortex, and very recently and surprisingly in 2D electron gases at high Landau levels [38].

Many researchers now think that stripes do form in the cuprates. However, there are many questions and debates concerning their properties. In some materials, namely the Nd doped $La_{1.6-x}Nd_{0.4}Sr_xCuO_4$ compound, compelling evidence exists for static stripes [39]. In other cuprates the stripes are believed to fluctuate making their detection more difficult. However in the fluctuating case evidence exists from neutron scattering [40]. Another key question is the role stripes play in producing superconductivity. Some think that stripes are crucial, some think they are beneficial, and others feel they are detrimental. The answer to this question may depend on whether they are static of fluctuating. Even though many questions concerning stripes remain open at present, one group of researchers has developed a model of high-T_c superconductivity in which stripes are the key ingredient. This model was proposed by Emery and Kivelson [33] in 1997. In their model the upper pseudogap (PG) crossover occurs when the stripes form, the second PG crossover occurs when spin pairing occurs in the AF regions near the charge stripes. This pairing is manifested in the charge stripe via pair hopping between the AF regions and the charge stripes themselves. Emery and Kivelson refer to this as a magnetic proximity effect. Finally as the temperature is lowered even further the stripes become Josephson coupled and long range phase coherence (superconductivity) is established.

4.2.3 Other doped AF models

There are many models which have not been mentioned which fall under the banner of doped AF, or doped Mott insulators. Many of these other models are simply variants of the ideas described above or combinations. For example a model by Sachdev combines the ideas of RVB spin-liquids and stripes. Other models contain an electronic phase separation but predict clusters or bubbles of charge instead of stripes. Interestingly some recent STM data [41] suggests an electronic phase separation into bubbles or clusters of holes.

4.3 Modified Fermi-Liquid Models

Modified FL models assume that SC can be obtained without the need for the strong interactions associated with a low carrier density and proximity to the Mott insulating phase. As with the doped Mott insulator models there are too many FL models to discuss. Thus, the only one which will be described is the model

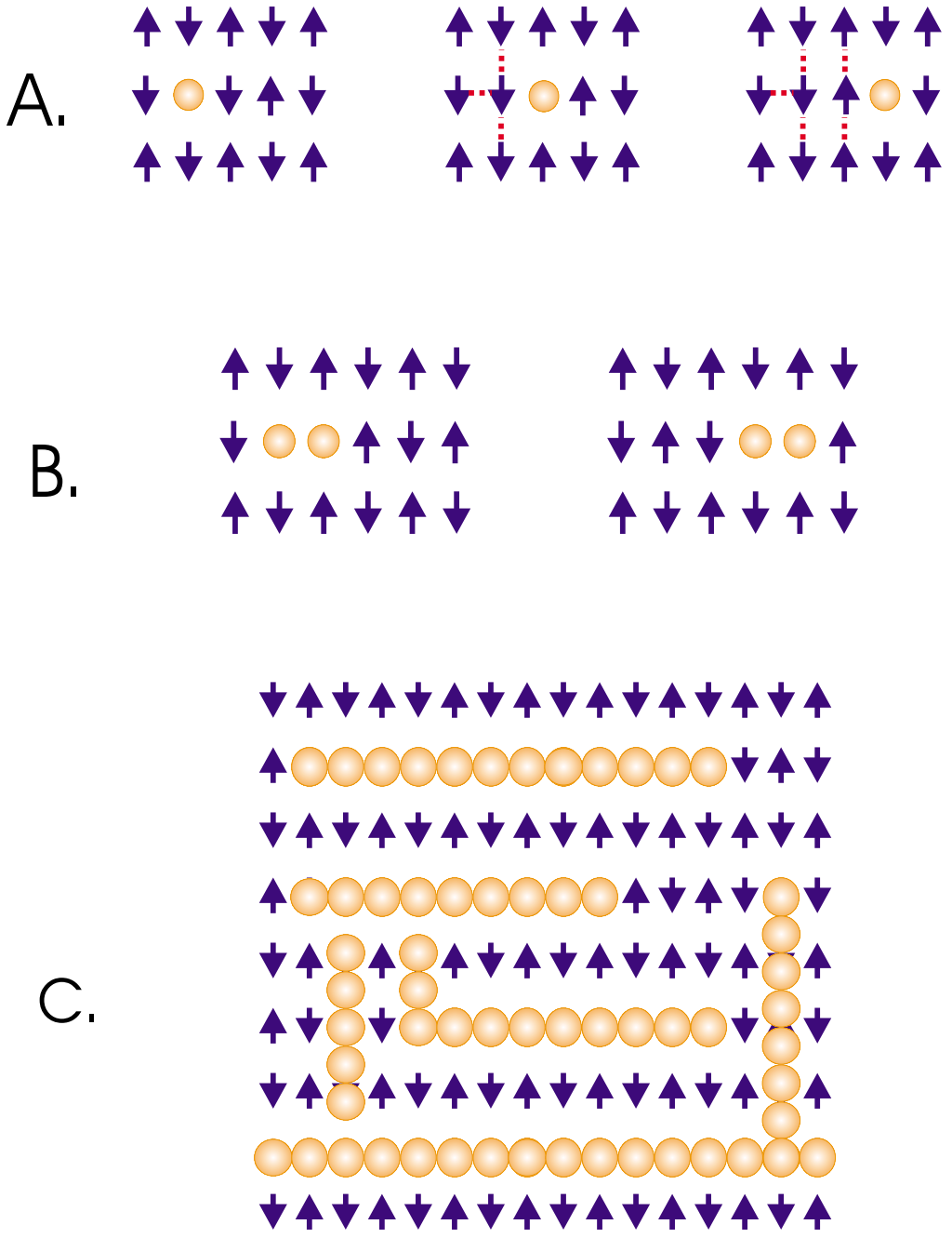

Figure 4.2: (A) The motion of one hole creates frustrated bonds and destroys the AF lattice. The motion of one hole is an energetically favorable process. (B) A pair of holes can seemingly propagate without frustration, but this is not the case. (C) The competition between hole expulsion and Coulomb repulsion results in stripes.

by Pines and co-workers [42] This model is known as the nearly anti-ferromagnetic Fermi-liquid (NAFL).

Even though it is unclear that a Fermi surface can be defined for some levels of doping, early ARPES experiments suggested that one exists. Thus the NAFL model assumes a well-defined Fermi surface. The model is a bottom-up approach and is based directly on early experimental observations from ARPES and NMR. In order to fit NMR data which showed AF correlations, the model assumes two types of quasiparticles (qp's) which are wavevector dependent. The "hot" qp's couple directly to AF spin fluctuations while "cold" qp's do not. The model predicted the hot qp's were located on the Fermi surface at $Q = (\pi, 0)$ and $Q = (0, \pi)$. The experimental data on which the model is based obviously must agree with d-wave, but only a few people were thinking of OP symmetries at the time. Pines and co-workers could only get their model to fit the data by assuming a d-wave OP. This gave them a very specific prediction; a d-wave OP. Although they were not the first to suggest a d-wave OP their prediction received a great deal of attention. The developers of this model believed so deeply in the theory they literally challenged the experimental community to prove them right or wrong. They even promised to withdraw the theory if experiments showed anything other than d-wave. Fortunately for them, experiments did indeed show their OP symmetry prediction is correct.

In this model the PG is explained as follows. At high temperatures, the AF correlations are absent. At the upper PG crossover temperature, T^o, AF correlations set in and the hot qp's interact with the AF correlations. At the lower crossover temperature, T^*, the hot qp's become gapped. Superconductivity occurs when all the qp's become gapped. Since the hot ones are already gapped at T^*, the gapping of the cold qp's determines T_c.

4.4 Competing Order to explain the Pseudogap

Many researchers have developed models based on types of competing order to explain the PG. These models do not attempt to explain SC. It is clear from looking at the phase diagram in Figure 2.3, that something is killing the superconductivity as the doping is decreased. Randeria et al. explain this simply as the system becoming more and more Mott like as the doping is decreased. Others feel a type of competing order parameter (not a SC order parameter) is turning on at certain doping and temperature levels and killing SC [43, 44, 45]. Most of these competing orders involve exotic forms of AF with examples being the proposed staggered flux phase, d-density waves, and a figure eight like orbital current pattern. All of these are examples of a type of orbital, as opposed to spin, AF. These competing orders may in some cases to have long range order, making their detection feasible, especially in a mesoscopic samples.

Chapter 5

Properties of Superconducting Nanowires and Mesoscopic Structures

5.1 Non-superconducting Mesoscopic Structures

The characteristics of all solids depend on many important characteristic length and energy scales. An incomplete list of these is: the atomic spacing, typically a few angstroms, the electron mean free path, which ranges from a few angstroms for alloys and up to 50 microns for ultra-clean, 2D semiconductors at low temperatures, the phase coherence length, the length over which electrons lose their phase memory, the Fermi energy, the energy of the highest occupied electron state, $k_B T$, the thermal energy, and many others.

In large, macroscopic structures, the sample dimensions are much greater than any of the characteristic lengths. However, modern lithography techniques allow for the fabrication of structures whose dimensions are smaller or comparable to one or more characteristic length scales. Such structures are referred to as mesoscopic. Many of these length scales are highly temperature dependent, making cryogenic cooling necessary for observing sample size effects. An example is the transport in an ultra-cold, normal metal nano-ring, whose circumference is on the order of the electron phase coherence length. In this and other examples, the size, and temperature of the sample allows for quantum effects to be observed.

5.2 Superconducting Mesoscopic Structures

In superconducting, mesoscopic samples the characteristic length scales that are most important are different than in the non-superconducting case. For instance the single electron phase-coherence length and mean free path are not relevant when a sample is in the superconducting state. The length scales most important in SC

samples are the Ginzburg-Landau coherence length ξ, the London penetration depth, λ, the vortex-vortex spacing, and vortex mean free path. For the high-T_c superconductors other theory dependent length scales emerge. These will be discussed later.

Superconducting mesoscopic samples can be in a variety of different regimes depending on the sample width, and whether the material is a type I or type II superconductor. The sample's width, w, can be roughly the same as ξ and smaller than λ, or vice versa. Or instead of the sample's width being smaller than any of the characteristic lengths, it may simply be the same order of magnitude in size (a few to 100 characteristic lengths).

5.2.1 Critical Current Density in Mesoscopic Superconducting Structures

The current density, J, in a wire or slab of material is defined as the current, I, divided by the cross sectional area, A. As discussed in chapter 1, a supercurrent, I_s, flows only near the surface within a thin shell of thickness λ. This is a possible source of confusion when defining the current density in a superconducting sample. Should one divide by the cross-sectional area of just the surface portion carrying the current, or the entire cross-sectional area? The answer is simply convention and one divides only by the area which actually carries current. However for nanowire samples in which the width is less than or comparable to λ, the current distribution over the cross-section of the wire is nearly uniform. In this case one simply divides by the entire wire cross-section.

The maximum current density a wire can sustain before a voltage appears is called the critical current density, J_c. The mechanism for the wire going normal depends on whether it is a type I or type II superconductor.

In a type I superconductor the critical current is reached when the self-field at the surface of the sample exceeds the critical field, H_c. For a cylindrical type I wire of radius R, the cross-sectional area in which current flows is given by, $\pi R^2 - \pi(R-\lambda)^2 = \pi(2R\lambda - \lambda^2)$. Using Ampere's law, $H = \frac{\mu_o I}{2\pi R}$, to calculate the self field at the surface this gives the result

$$I_c = 2\pi R H_c/\mu_o \tag{5.1}$$

Dividing by the current carrying area gives the critical current density

$$J_c = \frac{2RH_c}{\mu_o(2R\lambda - \lambda^2)} \tag{5.2}$$

For large wires in which $\lambda \ll R$, Equation (5.2) reduces to

$$J_c = \frac{H_c}{\mu_o \lambda} \tag{5.3}$$

For mesoscopic superconductors where $R \approx \lambda$ the quantity $2R\lambda - \lambda^2$ is nearly equal to λ^2 and the same result is obtained except for a factor of 2. For samples where $R < \lambda$ the actual cross-sectional area of the wire should be used in the calculation.

For a type II superconductor the situation is more complicated. A transport current generates a Lorentz force on the vortices. When the vortices flow an effective E-field is created, and thus a voltage. However, defects in the crystal create pinning sites for vortices and thus the current value which nucleates vortices at the edge of the sample is lower than the value which causes them to flow. So for a type II superconductor the current at which vortices begin to flow defines the critical current. The degree to which vortices are pinned is largely a function of the material itself and sample quality. For a superconductor with zero or extremely weak pinning of vortices the critical current is very close to the value in Equation (5.3), but with H_c replaced with H_{c1}. In most cases however, the value of the critical current will be determined by the pinning forces.

5.2.2 Vortices and Phase-Slip Centers

The core of a vortex is roughly 2 coherence lengths wide. Thus vortices can only nucleate in samples whose widths are greater than this. The supercurrent flowing around a vortex extends out to a radius of roughly a London penetration depth. In samples with widths smaller than a penetration depth a vortex can still exist, but the supercurrent around the vortex is highly distorted.

In long filamentary superconducting samples in which the width is roughly one to a few coherence lengths, vortices become ill-defined since their cores would not fit into the sample. For samples in this size regime entities known as phase slip centers (PSC's) may nucleate. The exact nature and explanation of these is not perfectly understood, but a model created by Skocpol, Beasley, and Tinkham [46], the SBT model, is in good agreement with experiment. PSC's are localized sections along the wire where the order parameter magnitude fluctuates to zero. Since the sample is only few coherence lengths wide, the order parameter magnitude can go to zero across the entire width of the wire. This creates a normal section in the wire which creates a situations very analogous to a Josephson junction. The phases of the order parameters on each side of the normal region evolve at different rates. Thus the entities are called PSC's. Each time a PSC is nucleated a the voltage abruptly changes creating a step in the current voltage characteristics.

5.3 High-T_c Mesoscopic Structures

The high-T_c superconductors are highly type II with $\lambda \approx 100\xi$. The values for ξ are roughly $1 - 4$nm, making penetration depths $100 - 400$nm. The fabrication of high-T_c samples with widths on the order of ξ

would be exceedingly difficult and to date no one has done this. Fabricating structures with widths less than λ is difficult but certainly possible. The samples studied for this thesis are in this regime. In addition there are other theory dependent length scales important for the cuprates. Two of these are lengths associated with the stripes discussed in chapter 4. The stripes are one dimensional charge carrying channels. Thus their widths are extremely small and are presumably a lattice constant (a fewÅ). The only measure of their lengths comes from two independent sets of neutron scattering data. Mook et. al [47] were able to deduce a charge ordering or stripe correlation length of no less than 35nm for YBCO. And Lake et al. [40] deduced a correlation length of 40 nm for LSCO. Also mentioned in chapter 4 were various types of competing order parameters. If present, these will have characteristic length scales and domain sizes. There is little to no experimental data from which to guess these lengths.

Existing work on high-T_c nanostructures is rare and not many have attempted making the samples. This was one of the main reasons the experiments described in this thesis were carried out. Some very early work on fabricating and measuring high-T_c nanowires ($50 - 200$ nm in width) done [48, 49] suggested ultra-high critical current densities. This work showed J_c's as high as $10^9 A/cm^2$ at 77 K, which is $2 - 3$ orders of magnitude higher than normal. Only a few other groups have ever studied high-T_c nanostructures [50, 51], and there are no other reports of ultra-high critical current densities. The data presented in this work shows some signs of an enhanced critical current density but not as large. This will be discussed in a later chapter along with a general comparison of the experiments performed for this work to the other work on high-T_c nanostructures.

Chapter 6

Fabrication of High-T_C Nanowires

6.1 Overview of Fabrication Process

Fabricating nanoscale samples made from any material can be a challenging endeavor. The same is true with the growth and fabrication of any size high-T_c sample. The combination of these two, the fabrication of high-T_c, nanoscale samples, is therefore an extremely challenging process. A considerable amount of trial and error, time, and effort went into creating and perfecting the fabrication technique. The procedure for making one sample involves many steps and approximately 50 hours of actual work time, or about 5 days.

The patterning of cuprate thin films is difficult for several reasons. One is sensitivity to heat. The oxygen content of the material determines its T_c and other superconducting properties. Many processing steps such as ion etching, and resist baking, create excess heating of the sample. Heating can result in oxygen loss thereby killing the superconducting properties. If the heating occurs in vacuum, as is the case for many processing steps, then this loss can be even worse. Next is sensitivity to many processing chemicals such as deionized water, and lithography resists. This requires a process in which the films and structures are never exposed to water, and the use of select lithography resists.

The conditions during deposition of the cuprate material restrict the type of lithogrpahy that can be performed. Broadly speaking, there are two types of lithography. One is called ”lift off” and the other is simply etching. In a lift off process, the substrate material is coated with resist first. A lithography step leaves holes in the resist, into which the desired material is deposited. The material that is not deposited into a hole gets washed away with the resist when exposed to the proper solvent. The deposition of cuprate material requires substrate temperatures of several hundred degrees Celsius. At this temperature the resist would burn off or become damaged. This means the cuprate material must be deposited first, followed by the

lithography steps. In this case the resist is put on top of the cuprate and serves as a mask during etching. This process works just fine for micron scale patterning which can be performed with photolithography. However, nanoscale lithography requires the use of electron beam resist, which is much thinner than photoresist. The thickness of the electron beam resist is not great enough to serve as a etching mask. The reason is that the etch rates of cuprates are very slow and the resist would etch away before the cuprate was fully removed in the desired areas. This leaves a few possibilities. One is a lift off procedure on top of the cuprate of a material that can be used as an ethcing mask. This process was tried with a silicon monoxide etching mask. This worked in terms of forming the desired structure, but it seriously degraded the cuprate. It was thought that the cause of the degradation was the silicon monoxide However, the process was also tried with carbon as the etching mask and this did not work either. Carbon is known to not harm cuprate materials, thus it is unclear why this process does not work. It is believed to be due to charging damage during electron beam(e-beam) writing. The possibility of charging damage, means that e-beam techniques can only be used if a protective layer, or buffer layer is put down on top of the cuprate. All of the e-beam writing is then performed in this layer. The final process which was discovered to be successful involves a carbon/gold bilayer. This bilayer first serves as protective layer, then later in the process as an etching mask. The process is outlined below and steps $6-12$ are shown schematically in Figure 6.1. From this side view shown in Figure 6.1 it may be a little difficult to see how the process results in a nanowire. A top view of processing steps 11 and 12 provides a clearer picture of how a nanowire is formed. This is shown in Figure 6.2.

The steps in processing order are: (1) Pulsed laser deposition of YBCO thin film. (2) Deposition of carbon onto YBCO by sputtering. (3) Deposition of gold onto carbon by sputtering. (4) Inductive T_c testing of film. (5) Spinning and baking of electron beam resist. (6) Electron-beam lithography. (7) Nitrogen cooled ion milling of gold layer. (8) Reactive ion etching of carbon. (9) Nitrogen cooled ion milling of cuprate. (10) Creation of cuprate leads and contact pads by photolithography. (11) Removal of carbon from nanowire by reactive ion etching. (12) Deposition of gold leads and contact pads by photolithography.

6.2 Pulsed Laser Deposition of YBCO Thin Films

The first step of the fabrication process is the deposition of a high quality YBCO thin film. To achieve this a process known as pulsed laser deposition or laser ablation is used. This is a physical vapor deposition technique in which a pellet(or target) of material is hit with an intense UV laser pulse creating a stoichiometrically correct plume in which a substrate sits. Typically the substrates are heated to about $800^{\circ}C$ so that surface diffusion is enhanced making epitaxial growth possible. Pulsed laser deposition can be done in

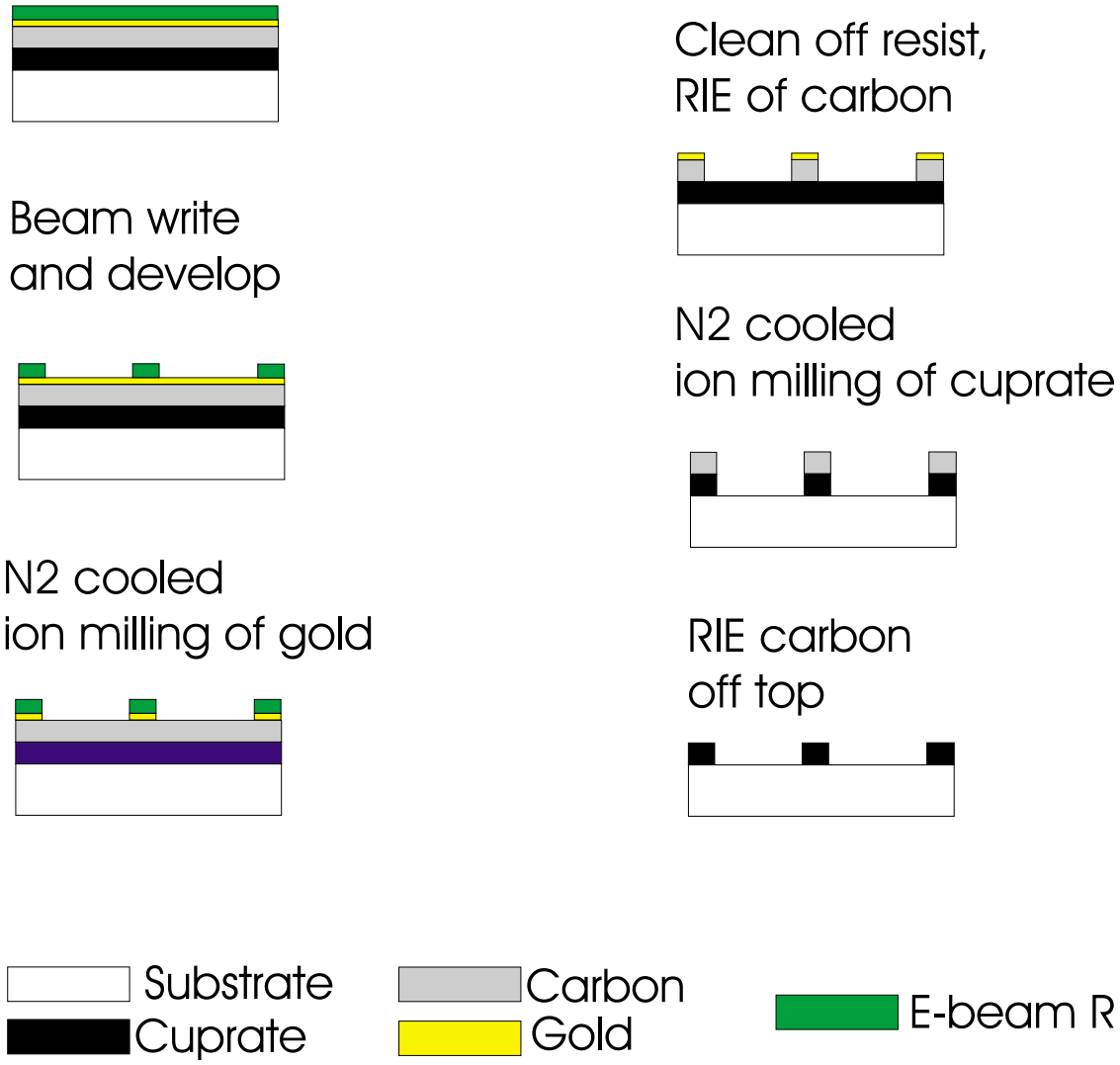

Figure 6.1: A side view of the nanowire fabrication process.

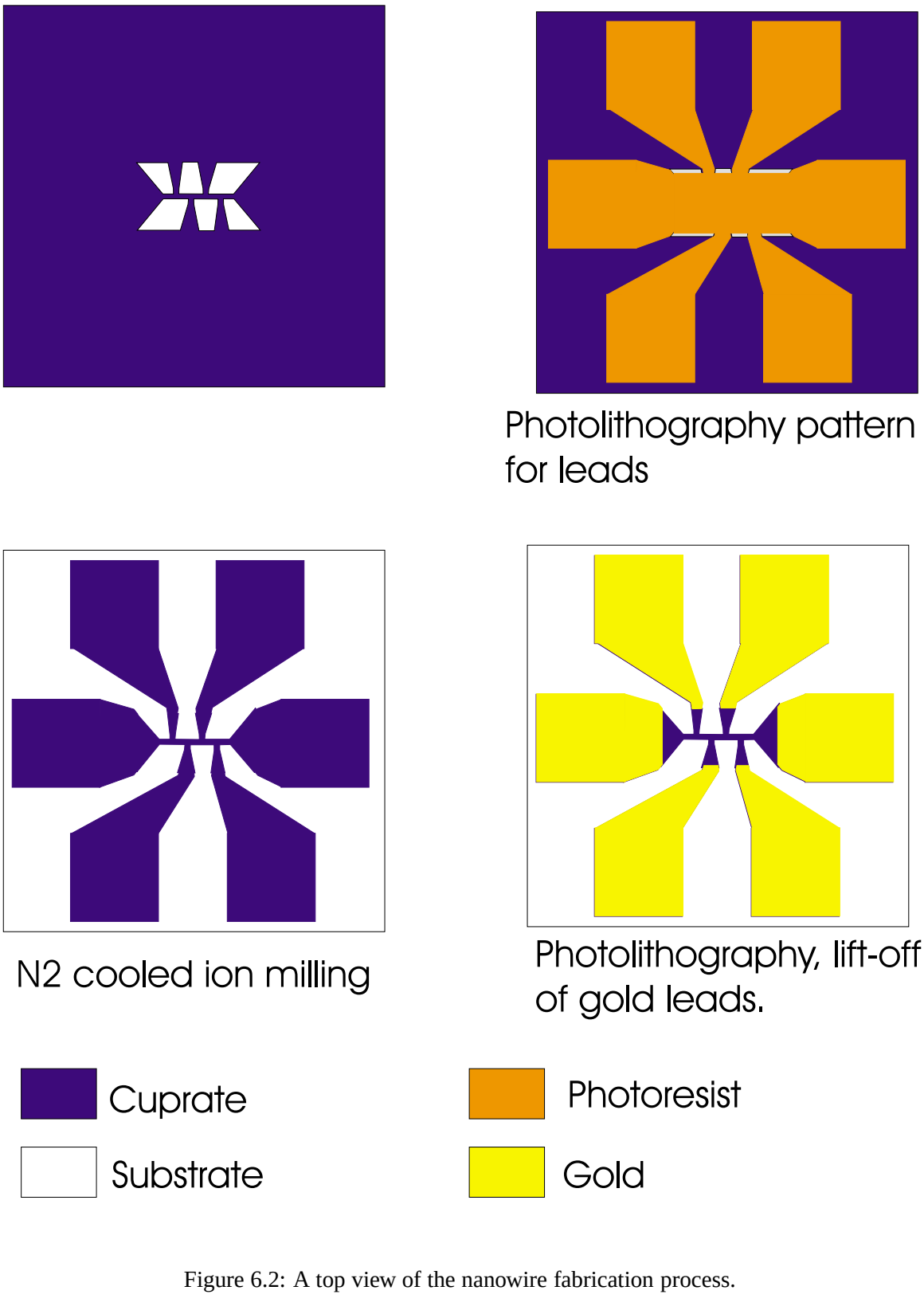

Figure 6.2: A top view of the nanowire fabrication process.

vacuum, but typically most compounds, including the high-T_c cuprates, require the presence of oxygen or other gases. We typically perform ablations at O_2 pressures between $20 - 500$ mTorr depending on what doping level we desire.

6.2.1 The Pulsed Laser Deposition System

The pulsed laser deposition consists of 4 main parts, the laser, the optics, the vacuum system, and the substrate heater. A great deal of the system was designed and built by myself and former members of Dale Van Harlingen's research group.

The laser is made by the company Lambda Physik and is of the UV pulsed excimer type. This is a gas laser which uses an excited dimers (hence the name excimer) molecules as the lasing medium. The excited dimer used by the systerm is the metastable compound ArF. It produces UV radiation at $193nm$ with energies of about 100-600 mJ per pulse. The laser can produces pulses with a rate of $1 - 10Hz$.

The vacuum system was designed by Ralph Schweinfurth, a former University of Illinois student and former member of the Dale Van Harlingen research group (Ph.D. 1994). The vacuum chamber includes a high quality UV-transparent, vacuum-compatible window, a rotating carousel type pellet holder capable of housing 4 pellets, and all of the plumbling, gas handling, and flow control in order to regulate the pressure during deposition.

The substrate heater was designed by myself and William Neils, another former Dale Van Harlingen group member (Ph.D. 2001). The heater incorporates a quartz-halogen bulb which radiates onto an inconel (an exotic stainless steel-like alloy) plate, on which the substrates are attached. This heater was designed and built in the Spring of 2002 after the failure and melting of a commercially made heater. The quartz-halogen bulb design requires that every part of the heater, except the inconel substrate holder remain cool. This is accomplished by a water-cooled reflector and base. Also the edges of the inconel plate are machined such that the contact area to the rest of heater is minimized. This results in a large thermal gradient. The center of the inconel plate can reach temperatures as high as $1000^{\circ}C$ while the rest of the heater and the base of the bulb are much cooler at temperatures $< 100^{\circ}C$. The entire heater except for the inconel plate are made entirely of stainless steel.

To keep the laser beam from digging a hole into the pellet, one of two things must be done. The laser beam must be scanned, or the pellet must be scanned. It is also a nice feature, especially for large substrates to have the plume scan relative to the substrate. This ensures a uniform film thickness. There are two ways to accomplish these criteria. One is having a scanning target holder, and scanning substrate heater. This approach was used on our original laser ablation system made in the late 1980's. This scanning technique

was successful for many years but normal wear and tear took their toll and the system became unreliable. To fix this problem, I decided to use another approach which is to scan the laser beam. This meets both criteria by scanning one thing. In this case the beam moves relative to the target, and since the beam is also moving relative the heater, the plume moves relative to the substrate. This technique has two major advantages. One is there are no scanning parts inside the vacuum chamber, and two is that it is an order of magnitude cheaper. This scanning system operates by sending the beam into a scanning UV mirror. The mirror is held in what is known as a gimbal mount. This mount can rotate about the x and y axes independently. Motorized micrometers control the angle of the mirror and the motors are controlled by a home-written computer program. By placing the pellet several feet away from the mirror, minuscule changes in the angle results in large lateral motion of the beam. The mount and motorized controllers are commercially available from Oriel. The UV mirror is commercially available from Acton Research.

6.2.2 Step by step description of YBCO deposition

The first step is to attach a $LaAlO_3$ subsrate to the substrate holder. $LaAlO_3$ is used because it has a very close lattice match to YBCO and because edge-oriented substrates made from $LaAlO_3$ are readily available. The substrates are attached by silver paint. The paint used is "Leitsilber" silver paint available from Ted Pella Incorporated. Other brands of paint do not work as well or at all. The paint is coated onto the back of the substrate with a paintbrush. Then the substrate is gently pressed onto the substrate holder. Finally the holder is baked on a hot plate at roughly $300^{\circ}C$ for about 20 minutes. Silver paint is used because it provides great thermal contact between the substrate and holder while simultaneously allowing for easy removal of the subsrate after deposition. Silver paste has also been used, but the substrates frequently crack when trying to pry them off.

Next, the substrate holder is slid into the heater and the vacuum system is pumped down to a base pressure of $3\text{x}10^{-8}$ Torr. With the pellets shielded, the substrates are then brought up to the growth temperature of $820^{\circ}C$. With the substrate shielded from the plume, a pre-ablation is performed to clean off any possible contaminates from the pellet. When the heater is turned on the pressure rises due to outgassing and usually takes $15-20$ minutes to get back into the 10^{-8} Torr range. Once the pressure is low enough, and the pre-ablation is complete, ultra-high-purity (99.999 % pure) oxygen is allowed to flow into the chamber until the flow controlling system stabilizes the pressure to the desired value. 500 mTorr gives optimal doping with a T_c of 93K while 20 mTorr gives medium underdoping and a T_c of about $70-80$ K. Once the conditions are set the ablation process begins. An ablation time of 3 minutes at 2 Hz, and 300 mJ per pulse gives a film thickness of about 500 Å.

Another very important step is the annealing of the films after the deposition is complete. The annealing parameters also affect the doping. The parameters adjusted are; the oxygen pressure, the temperature at which oxygen is flooded into the system, the temperature at which the annealing occurs, and finally the annealing time. For underdoped, the system is flooded with oxygen when the substrate temperature is about $600^{\circ}C$, and the annealing takes place for 15-20 minutes at 200 Torr. For optimal doping, the system is flooded with oxygen at the growth temperature ($820^{\circ}C$) and annealed in 1 atm of oxygen for a few hours.

By adjusting the annealing and growth parameters good films with T_c's ranging from $40 - 93K$ can be grown. The film quality is usually excellent with large single crystal regions ranging from 300nm up to a couple of microns. The films are usually smooth, shiny, have good room temperature resistivities and are pin-hole free. The widths of the transitions are narrow and range between $2 - 7$ K. If a film is found to not meet the highest standard of quality as judged by transition width, smoothness, resistivity, and absence of pinholes, then the film is not used.

6.3 Deposition of the Carbon/Gold Bilayer

The carbon and gold layers are deposited directly on top of the YBCO film by a process known as DC magnetron sputtering. This is performed with commerically made sputtering guns and targets. The sputtering guns are located in the same vacuum system in which the pulsed laser deposition occurs. A sample transfer arm allows for the in-situ deposition of these layers after pulsed laser deposition. However, it is felt that inspection of the YBCO film is more important, so usually vacuum is broken between the steps. A sputtering gun is a simple device in which argon ions are created by large bias voltage. These ions are then confined by a magnetic field to stay near the target. By clever arrangement of the electric and magnetic fields around the target, the argon ions continually bombard the target ejecting atoms of target material. This process make a plume or plasma cloud of ions and target atoms. The substrate simply sits in the cloud and the target atoms stick the substrate. A carbon layer of about 1000 Åis deposited, followed by a very thin, 20 Å, layer of gold. The purpose of these layers will become clear when the other processing steps are described.

6.4 Inductive T_c Testing of film

The T_c's of the films are tested inductively instead of resistively. This is simply because a resistive T_c test requires the use of contact pads which would mar the surface of the film causing potential problems later.

The inductive test incorporates two coils, a drive coil, and a receive coil. The drive coil is excited with

a current with the same frequency as that from reference signal which comes from a lock-in amplifier. The signal from the receive coil is fed into the the lock-in amplifier. When the superconducting transition occurs the Meissner effect screens the field blocking the path to the receive coil.

6.5 Electron Beam Lithography

Electron beam(e-beam) lithography is a nanoscale patterning technique in which fine control of the electron beam in a scanning electron micrscope (SEM)is used to trace or draw a pattern. The typical beam diameter for a modern SEM is a few nanometers and the lateral control of the beam can also be as fine as a few nanometers. With fine tuning, e-beam lithography can produce features sizes down to 25 nm. The minimum feature size is governed by what is called the proximity effect. This effect is a broadening of line-widths due to exposure from backscattered secondary electrons.

The electron beam traces out a pattern in a resist material thereby exposing the desired areas and leaving other areas unchanged. After rinsing in a chemical called a developer this process results in a mask of resist. By etching the material underneath the resist, or depositing material into the holes in the resist, nanoscale structures are created.

6.5.1 Spinning and Baking of the Electron Beam Resist

Resists, whether for e-beam lithography or photolithography, are polymers whose characteristics and structure change when exposed to charge or UV light. The most commonly used e-beam resist is polymethymethacrylate (PMMA). PMMA comes in many different molecular weights and solvents. The PMMA used in this work has a molecular weigth of 950K amu, and is dissolved in anisole. The PMMA is premixed and commercially available from Microchem Inc. When PMMA is exposed to the correct dosage of charge, it breaks down into lower molecular weight monomers which dissovle in a chemical(developer)known as methylisobutylketone (MIBK). Before e-beam lithography can be peformed the sample must be coated with PMMA. This is done by spinning the sample and dropping on the PMMA. A spinning speed of 4000 RPM, and time of 20 seconds gives a PMMA thickness of about 200 nm. Before processing the PMMA film must be baked in order to drive out the solvent. For most applications PMMA is baked at a temperature of $> 170^{\circ}C$. Just above this temperature a glass transition temperature is reached causing the resist to flow and become more uniform. Resist uniformity over large samples is needed for many applications. So the standard, well known ”recipe” for baking PMMA is $180^{\circ}C$ for about 1 hour on a hot plate. This baking temperature and baking time was discovered by me to seriously degrade the T_c and transition width of

YBCO films, in some cases even completely killing the superconductivity. Because of this, a lower baking temperature of $90^{\circ}C$ and baking time of 10 minutes are used. This time and temperature result in little to no degradation. This discovery was an important one since many unsuccessful nanowire fabrication attempts were made assuming the films were still good after resist baking.

6.5.2 Controlling the Electron Beam

The SEM used for this work is a JEOL 6400 equipped with a lanthanum hexaboride (LaB6) filament. The filament ejects electrons which are then accelerated through a series of apertures and coils (lenses). Hardware and software made by JC Nabity Lithography Systems, allow for the computer control of a set of coils known as the scanning coils. Control of these is what makes the beam trace out the desired pattern.

There are many parameters associated with the SEM and beam which must be taken into consideration during e-beam lithography. The beam current, alignment, focus, stigmatism, filament current, magnification, and other values must all be set perfectly. All of these values are important. However the two most vital are the beam current and focus.

Setting the focus is the most important parameter. However, since imaging the area in which you desire to beam-write would expose the resist, obtaining the focus value directly is not possible. Therefore the focus value must be gotten from interpolation. This interpolation process works as follows: (1) scratch marks are made on each corner of the sample far away from where the writing will take place. (2) The focus values and positions of each mark are then entered into a computer program written by myself and Trevis Crane(a current student in Dale Van Harlingen's research group). (3) This program calculates the focus values at the desired positions by assuming a flat sample and simply fitting to a plane. To ensure the sample lies flat on the SEM's sample stage a couple steps must be taken. One is cleaning the stage to ensure no dust or dirt are present. Two, after pulsed laser deposition silver paint is still stuck to the back side of the samples. The surface of this paint is far from flat. Thus with great care, the paint is scraped off with a razor blade. If the sample does not lie flat, the focus gradient across the sample will be too large, making the calculated focus values inaccurate.

The beam current ranging from a few to several hundred picoamps must be accurately measured since it governs the charge dosage. Once the beam current is measured this value is entered into the Nabity software. The software then calculates how long the exposure will last. If the beam current is measured incorrectly, the writing will be either under or overexposed.

After beam writing, the sample is rinsed with developer. The developer is a mixture of 3 parts isopropanol to 1 part MIBK. Typical development times are 60-70 seconds for a charge dosage of $350\mu C/cm^2$.

6.6 Ion Milling of the Gold layer

After YBCO, carbon and gold are deposited and after the electron beam lithography is performed, the first milling (or etching) step is performed. As shown in Figure 6.1, the PMMA mask is on top of the gold. In order to remove the gold from those areas not covered by PMMA a process called ion milling is performed. This is a standard dry etching technique in which accelerated argon ions bombard the sample. The process is like sandblasting, but with ions. Ion milling can be a very damaging process if care is not taken. Most of the possible damage comes from heating. As mentioned heating of cuprate materials in vacuum deoxygenates the samples, thereby ruining them. The sample stage provided with the ion milling system uses water cooling. This was found to not be adequate. So a homebuilt liquid nitrogen cooling stage was incorporated into the system. Even with nitrogen cooling, the milling had to be done, in 30 seconds on/off cycles. In addition it was found that low beam currents and voltages significantly improve sample quality. Many users of the ion milling system use the max values of 500 V and 100 mA. Much lower values of 250 V and 50 mA were used for the nanowire samples.

By ion milling the gold away in regions not covered by PMMA, the desired pattern can be transferred into the gold. This gold pattern then serves as a mask in the following step known as reactive ion etching.

6.7 Reactive Ion Etching of the Carbon Layer

Reactive Ion Etching (RIE) is another dry etching in which very specific ions preferentially etch one material over another. In RIE a gas is introduced into the system which is excited into a plasma by an intense radio-frequency voltage. This plasma does the etching.

Below the gold mask is a carbon layer. Carbon can be readily etched with an oxygen plasma while the gold is not affected at all. The carbon is etched away in regions not protected by the gold mask. The oxygen plasma does not degrade or etch the YBCO so over etching is not a worry. This RIE process transfers the pattern from the gold layer into the carbon layer. Now the carbon layer, which originally was used as buffer layer, can now be used as a milling mask when the YBCO is ion milled. Carbon was chosen as a buffer layer and etching mask because it does not degrade YBCO and because it has a very slow ion milling rate, about 3-5 times lower then YBCO. This makes carbon ideal for this dual role.

6.8 Ion Milling of YBCO to Define the Nanowires

The same concerns arise here as when ion milling the gold layer. The ion milling of the YBCO is performed under same conditions as the gold milling. The only difference is that milling times are much longer for YBCO since the etch rates are much slower. Typical exposure times were 20-24 minutes depending on the YBCO thickness. It should be stressed again, that milling without liquid nitrogen cooling and without using low voltages and low currents was found to degrade the samples. This was one of the key discoveries which made the fabrication process successful.

6.9 Photolithography to Define the YBCO Leads and Contact Pads

In principle, this step could be eliminated by simply e-beam writing the entire pattern; nanowire, leads, and pads, all at once. However, this would require long e-beam writing times, and a stage controller option which is not available on the SEM used for this work. Using photolithography for this step is just as good and is much quicker.

Photolithography is very similar to e-beam writing, except a UV-sensitive polymer, known as photoresist is used. Standard photolithography can be used to make features as small as $1-2$ microns. In photolithography, photoresist is spun onto the sample and baked at $90^{\circ}C$ for 45 seconds. Then a mask is set on top of the sample and a UV bulb exposes the resist. The resist is then rinsed with developer, thereby transferring the mask pattern into the resist.

The photolithography mask used in this step overlays and meets with the e-beam written pattern. The e-beam pattern contains the nanowire and some small leads which branch out to a width of 10 microns. These 10 micron wide, e-beam written leads, then mate to the leads made by photolithography. This mating of the e-beam written pattern and photolithography pattern appear one as one of the steps in Figure 6.2 but is shown more clearly in Figure 6.3.

6.10 Removal of Carbon from the Nanowire Surface

Since the experiments performed for this work are carried out below and above T_c the presence of carbon on the surface of the cuprate nanowires would make the above-T_c transport measurements difficult if not impossible to interpret. The carbon, which served as an etching mask, is removed by RIE with an oxygen plasma as described earlier.

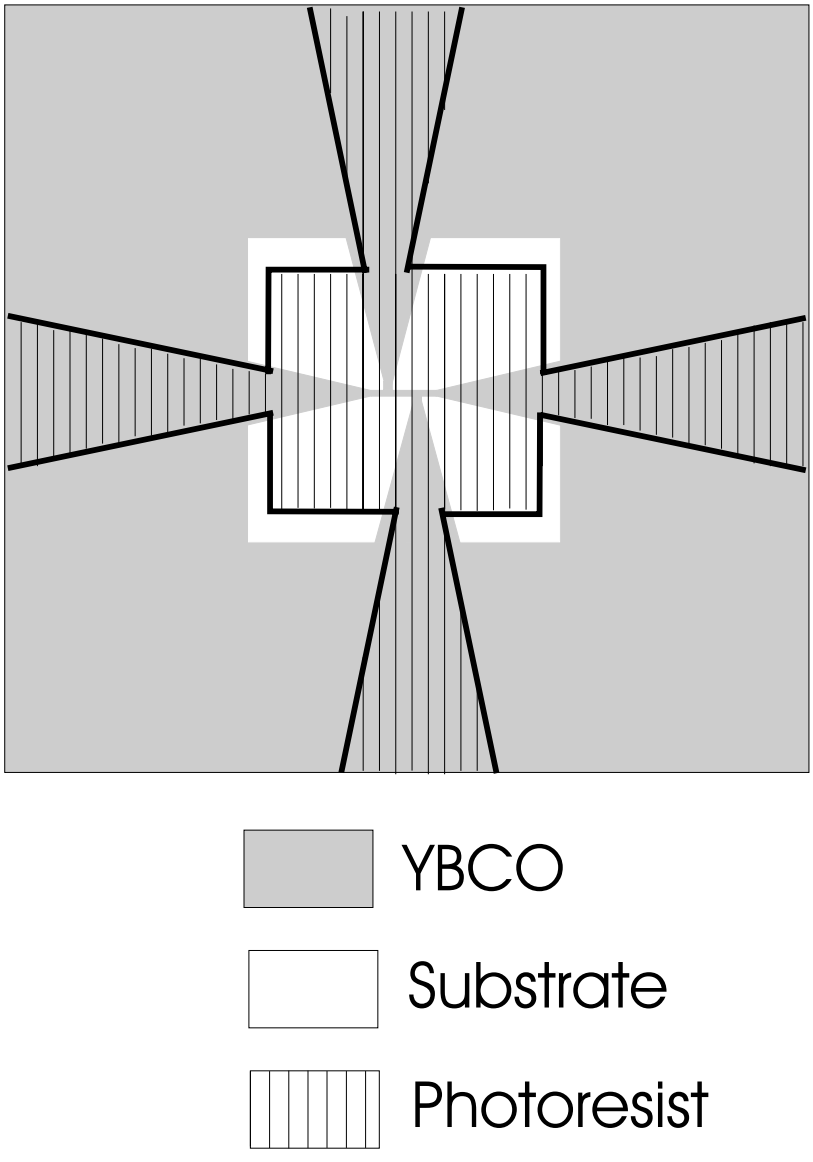

Figure 6.3: Zoom view for mating of photoresist pattern and e-beam written pattern.

6.11 Creation of Gold leads and Pads

This is a lift-off photolithography process which results in gold being deposited on top of the YBCO leads and pads. Photoresist is spun onto the sample and baked as previously described. Next, the photoresist mask is exposed and developed. Before the gold is deposited the sample is ion milled for $15 - 20$ seconds with a smaller ion milling system located in the same vacuum chamber which houses the gold sputtering tareget. The nanowire is not harmed by the ions since it is covered with photoresist and since the short exposure times do not allow for heating . This ion milling is done to clean off any oxidation layer which may have formed on the surface of the YBCO leads. Without breaking vacuum, gold is then deposited over the sample by DC magnetron sputtering. The gold that gets deposited into the holes in the resist sticks to the sample and the gold which is on top of the resist gets washed away with acetone. This is the last step of fabrication.

6.12 The Final Product

The multi-step process described in this chapter results in high-T_c nanowires with very little degradation. The T_c's, transition widths, and critical current densities, J_c's, are all nearly the same as for bulk film. A way to clearly demonstrate the sample quality of the nanowire is displaying the T_c tests from the starting bulk film and the nanowire on the same graph. This is shown in Figure 6.4. An SEM image of a nanowire is shown in Figure 6.5.

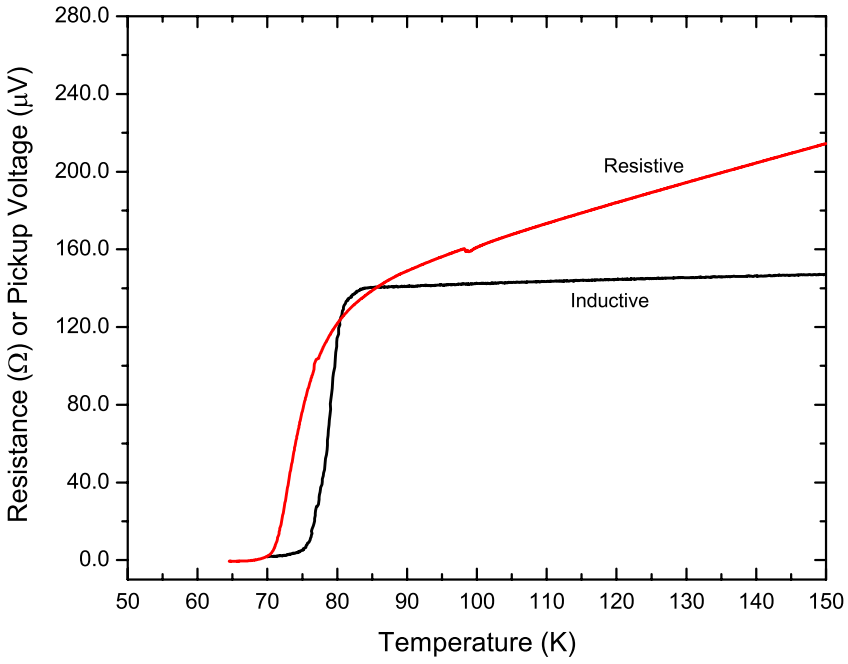

Figure 6.4: T_c's of the starting bulk YBCO film and the nanowire made from the film.

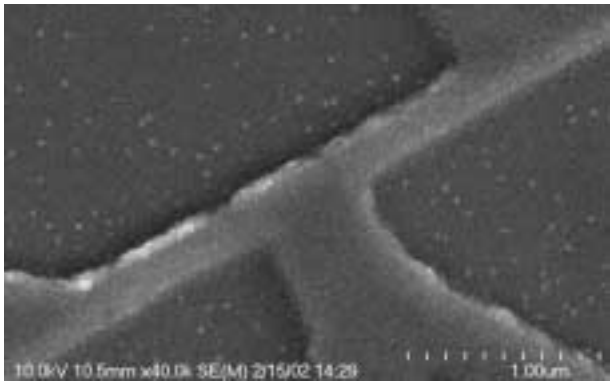

Figure 6.5: An SEM image of a 200 nm wide, YBCO nanowire.

Chapter 7

Experimental Techniques

Since fabricating the samples played a major role in this work, the lithography and deposition techniques were discussed in detail. Measuring the samples also required a great deal of care, work, and technique thus aspects concerning, the wiring of the sample, electronics, data acquisition, and cryogenics will be discussed.

7.1 Cryogenic Techniques

The measurements performed for this work were done over a broad range of temperatures ranging from 1.4K to 300 K. This requires a technique and apparatus capable of providing such a range. Three crysostats (cooling apparatus) were used to make measurements. All of the cryostats use liquid helium and are of the ”flow through” type. The simplest type of cryostats are simply well insulated reservoirs containing liquid helium. These are known as dewars. In these systems a long stick, known as an insert, holding the sample is simply inserted into the liquid. These systems are simple and easy to operate but only provide a temperature range near liquid helium temperatures. Flow through type cryostats are much more complex but provide a temperature span from 1.4 K up to several hundred Kelvin.

In these systems the sample is attached to an insert which sits in a vacuum space which is connected to a liquid helium reservoir through a needle valve. The needle valve is exactly what the name implies. It is a valve whose opening and closing are controlled by the motion of a tiny needle. An Ohmic heater is wrapped around the needle valve and can be used to heat the helium as it flows through the valve. When helium enters the sample space it boils and enters as a gas. In this case, the sample is cooled by the helium vapor. The temperature is governed by the position of the needle valve and the needle valve heater. In another mode of operation, the needle valve is opened fully, the sample space is isolated from the vacuum pumps, and the heater is turned off. These conditions allow liquid helium to flow through the needle valve and fill up the

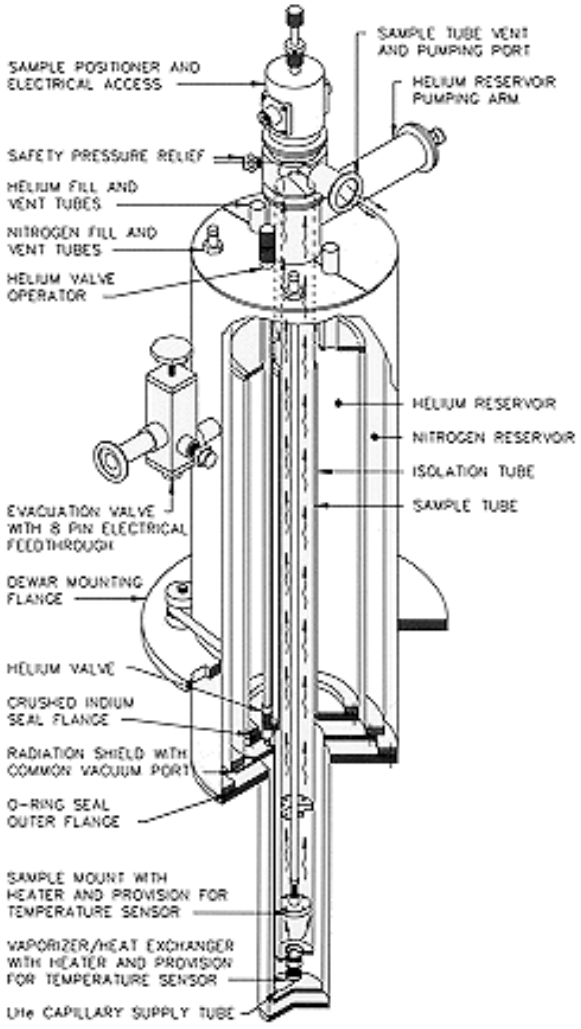

Figure 7.1: Schematic diagram of helium flow through cryostat

sample space. This provides temperatures down to 4 K. Once the sample space fills with helium, it can be pumped on with a vacuum pump to lower the temperature to 1.4 K. Two different flow-through cryostats were used for this work. The reason for using three, was to verify that the data and effects seen in the measurements were not an artifact associated with one particular system. Flow through crysostats contain several sections or spaces. There are vacuum spaces known as jackets which provide insulation. There is a space for liquid nitrogen which is used to minimize helium boil off. Then there is the liquid helium space and sample space. A schematic diagram of a typical flow through cryostat is shown in Figure 7.1.

7.2 Making Electrical Contact to the Samples

The lithography steps described in chapter 6 result in millimeter sized squares known as pads. Sixteen of these pads are arranged around the edge of the chip and make contact to the nanowires. These pads must be connected to wires which ultimately connect to the electronic instruments used to make the measurements. To connect wires to the pads, small pieces of indium were used. Indium is a soft, malleable metal, which is also extremely sticky. With a steady hand, these small indium pieces were pressed onto the electrical contact pads. While pressing on the the indium it was important to keep myself electrically grounded. Static electricity may build up and discharge through the sample thereby destroying it. For this reason, an anti-static mat and grounding strap were always used while pressing on the indium pads. It is tradition in many research groups to use small wooden sticks to press on the indium. However, a wooden stick is insulating and does not provide a path to ground. Thus a metal stick was always used. After the indium pieces are pressed onto the pads the wires must be attached. The wire used is coated with an insulating material called formvar. The formvar was removed on the tips of the wires with a dissolving agent and the wires were pressed into the indium. These wires are typically about 2 inches in length and are soldered to electrical pins which lead to to the electronics. The soldering iron tip is also ungrounded, so usually the wires were soldered to the electrical pins first, then pressed into the indium. Finally, once the wires were pressed into the indium, another piece of indium was pressed on top of each wire, making and indium/wire/indium sandwich. This method of contacting the sample provides stable electrical connection over a broad range of temperatures. The level of detail above may seem too involved, but in the initial stages of this project many samples were ruined before realizing how sensitive the nanowires were to static electricity.

7.3 Electronics and Measuring

Two basic types of measurements were made for this work. Those are resistance vs temperature, R(T) and current vs voltage, IV. The R(T) measurements were performed using the standard four-terminal technique. The current was supplied by a home-built, battery powered, voltage controlled, current supply. A current far below I_c was used ranging between 10 and 100μA. The voltage was fed into an Ithaco brand, model 1201 preamplifier. The preamplifier's main purpose was not amplification but rather for isolation and buffering of the sample from the digital electronics. The output from the preamplifier was fed into a Keithley brand, model 199, voltmeter. The voltage was read from the voltmeter using GPIB (IEEE 488) communication with a personal computer(PC). The temperature was read using a standard diode sensor, a Lakeshore brand model 330 temperature controller, and GPIB communciation with a PC.

The IV measurements were also carried out using a four terminal technique. However, some data was taken with 3 or 2 terminals when leads unfortunately became broken. For the IV's the same type of current supplies were used, but in this case a control voltage was supplied from a digital to anaolog (DA) board. The control voltage from the DA board was ramped by computer control causing the current value to also ramp. The IV's were performed in what is known as a bipolar retrace mode in which the current is ramped up to a positive value, then ramped back down through zero, then to a negative value, and finally back to zero. The voltage from the sample was fed into the same type of preamplifier as was used for the RT measurements. The output voltage was fed into an analog to digital(AD) board in the PC allowing for the voltage values to be read and recorded. The voltage monitoring the current was fed into another preamplifier and into another channel on the same AD board. Using this set up it was possible to ramp and measure the current, while simultaneously measuring the voltage. Schematic diagrams for the RT and IV measurements are shown in Figure 7.2.

The data acquisition and control programs used for both the IV and RT measurements were created by myself and a former graduate student Brian Yanoff. The programs were all written with software made by National Instruments known as Labview.

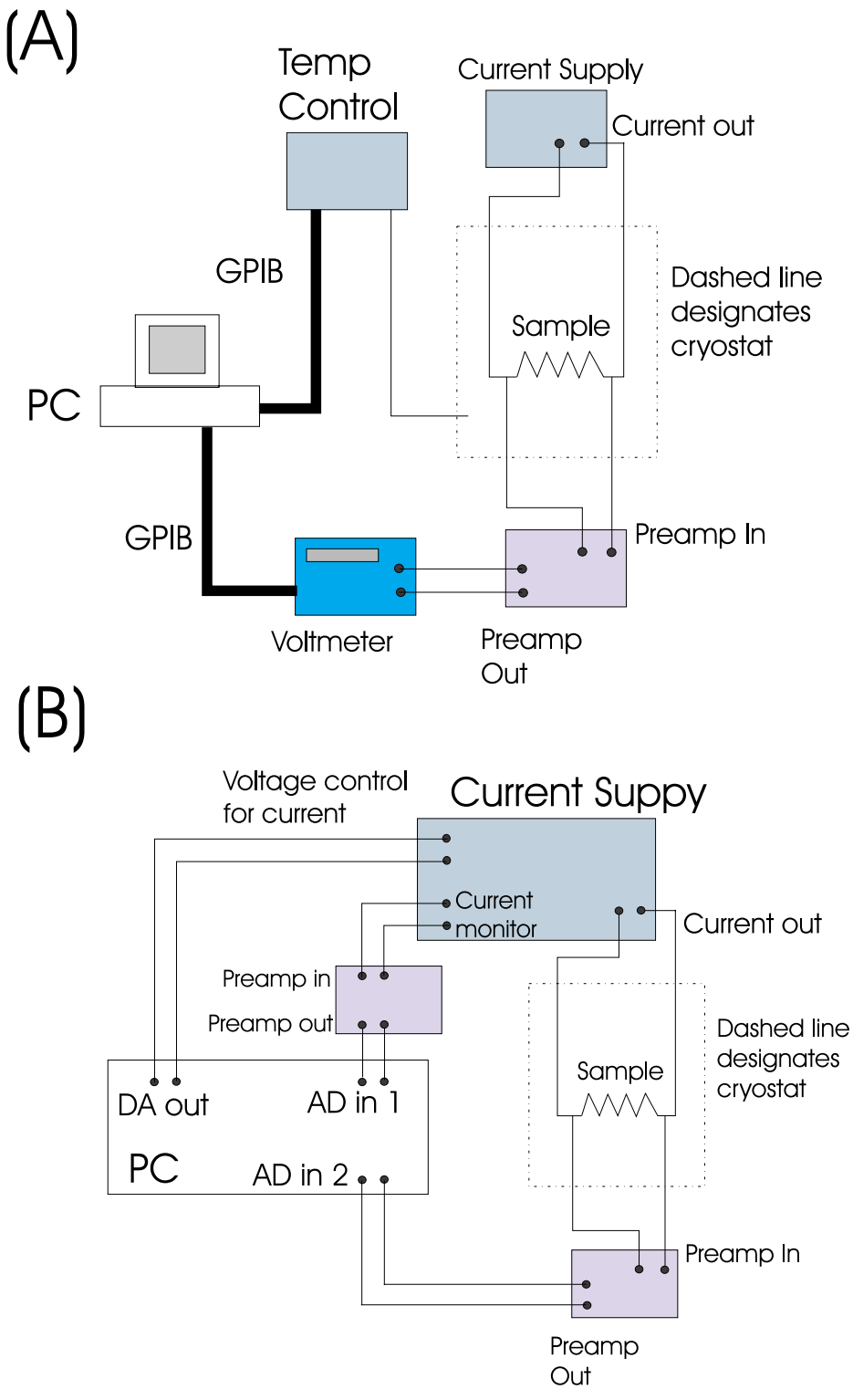

Figure 7.2: (A) Schematic for Resistance vs Temperature Measurements. (B) Schematic for Current vs Voltage Measurements.

Chapter 8

Critical Current Density Data

The mechanism by which superconductivity vanishes in the presence of a current for single grains or strongly coupled grains of cuprate material is somewhat of an unsettled issue. In the late 1980's Tahara et al.[52] suggested that if the width of a cuprate strip was on the order of a penetration depth or smaller, then a barrier-to-flux entry would exist and depairing, instead of flux flow, would be the mechanism for destroying superconductivity. Interestingly, a few years later there were two reports of ultra-high critical current densities in high-T_c nanowires. The ultra high critical current densities (J_c's) measured by Jiang et al. [48] and Zaquine et al. [49] were higher than expected by 2 orders of magnitude. They measured J_c's of 1.3 x $10^9 A/cm^2$ and 6 x $10^8 A/cm^2$ which is very nearly the de-pairing current, the current at which Cooper pairs unbind. If the data from Jiang et al. and Zaquine et al. are correct it is not flux flow, but depairing that governs the critical current density in the cuprates. Only a few other researchers have created high-T_c nanowires and the others have measured critical current densities which are not higher than expected or enhanced. The work by Larsson et al. [50] and Assink et al [51] did not exhibit such an enhancement and their values were in the high 10^6 to low $10^7 A/cm^2$ range. These values of J_c are consistent with a flux flow mechanism. At the time of the reports of ultra high J_c's, the idea of stripes playing a role in the cuprates had not been developed. I proposed the following hypothesis; Perhaps the enhancement in J_c seen by two groups is angle dependent due to the fact that charge stripes (if they are present) are believed to exist only along the a and b crystal axis directions. The substrates used for my samples were edge oriented, which means the edges of the substrates are parallel to the a and b directions. This allowed the nanowires to be fabricated along well defined directions. If the enhancement could be shown to be a function of angle this would be an explanation for the inconsistencies between results. It is also possible for an angle dependence to exist because of the d-wave nature of the order parameter in the cuprates, however this would not produce

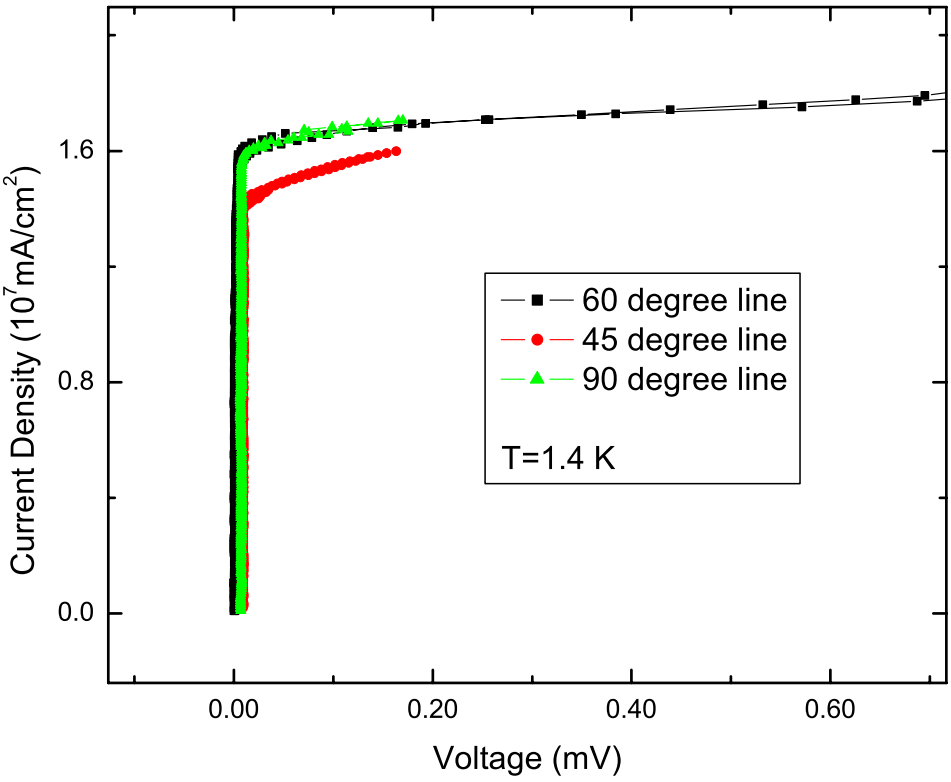

Figure 8.1: Current density vs. voltage at 1.4K of 3 nanowires ranging in width from 150-250 nm. The wire with the lowest J_c was 150 nm, while the other two were 250 nm wide. The thickness of all were 50 nm.

---

an enhancement.

The nanowires used for testing the angular dependence of J_c were lightly underdoped, and 150-250 nm wide. Each set of wires was fabricated from the same starting film and, in addition the sections of each film used were about 20 x 20 microns insuring there was no appreciable change in quality from wire to wire. The data from the 3 nanowires fabricated from film 080701 is shown in Figure 8.1. The 30 and 60 degree nanowires were 250 nm wide, while the 45 degree nanowire was 150 nm wide. The 45 degree line has a slightly lower J_c but the data shows no strong angular dependence. The J_c values for all 3 wires were in the low $10^7 A/cm^2$ range at 1.4K. Thus no enhancement was observed.

The critical current density as a function of angle was performed for another set of nanowires fabricated from a different starting film and similar results were obtained. The nanowires for this data run were all 200 nm wide and 50 nm thick. They were lightly underdoped with T_c's of 84 K. The J_c's were all in the low

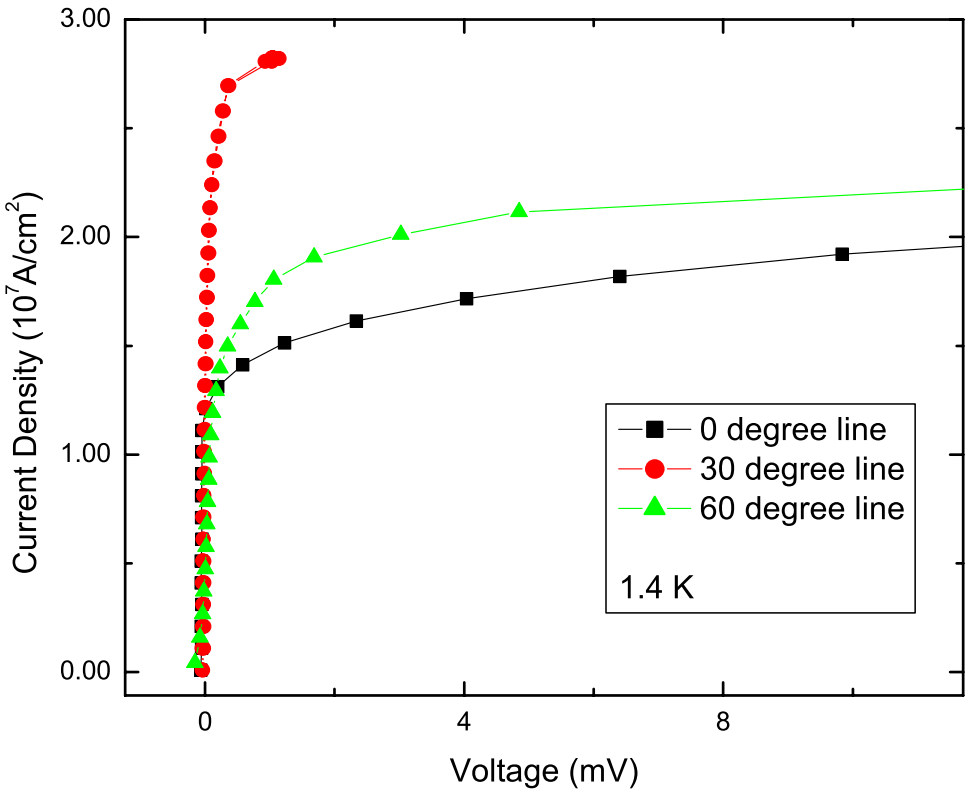

Figure 8.2: Current density vs. voltage for 3, 200 nm wide, 50 nm thick nanowires, performed at 1.4 K.

$10^7 A/cm^2$ range at 1.4K. As with the other set of nanowires, no enhancement or strong angle dependence was observed. These results are shown in Figure 8.2.

Other experiments and results concerning nanowires will be discussed later in this thesis. These other experiments required performing IV's. Thus a large number of J_c's were obtained in the process. A plot of all the J_c's as a function of width is shown in Figure 8.3. Of all the measurements only 1 showed a hint of enhancement. The J_c for this slightly enhanced sample was roughly a factor of 5 higher than normal. This one case of an enhancement is nowhere near the factor of 100 reported by Jiang et al. and was probably just a simple case of laboratory error. The rest of the data are consistent with the values observed by Larsson et al. and Assink et al.

The critical current density values of the nanowires studied for this work are in good agreement with a

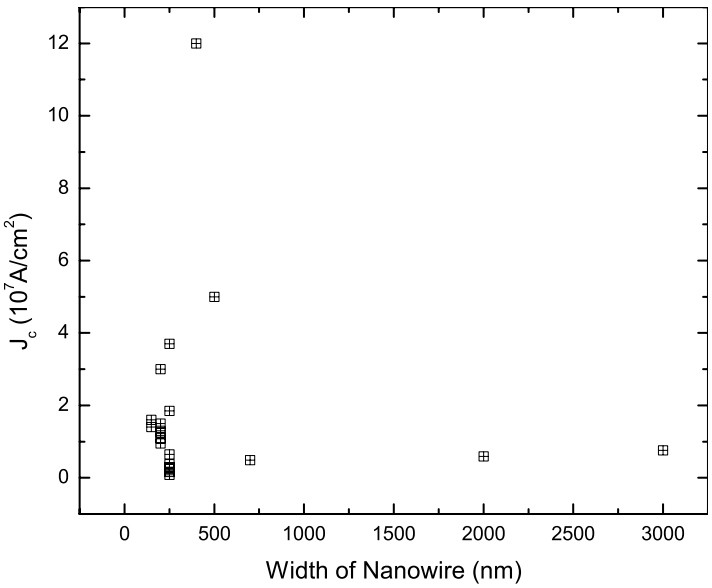

Figure 8.3: J_c vs width for all the nanowires measured for this work. All values for T= 1.4K.

---

flux flow resistivity mechansim. The flux flow J_c is [53],

$$J_c = \frac{\Phi_o}{32\pi\mu_o\lambda^2\xi} \tag{8.1}$$

Plugging in the known values for λ and ξ results J_c's in the low to mid $10^7 A/cm^2$ range depending on which quoted values are used. Note that it is unclear whether one should use λ_c and ξ_c or λ_{ab} and ξ_{ab}. However in either case one gets values that are nearly the same.

The IV's performed for the J_c vs angle experiments were only done out to very small currents. As soon as a voltage appeared the currents were ramped back down. However, it was later discovered that intriguing features appears in the IV's of nanowires at larger currents. These IV's will be discussed in detail later.

Chapter 9

Resistance Data

9.1 The Data

The resistance vs temperature, R(T), data for the nanowires exhibited rather intriguing results which are not completely understood. In a large percentage of the high quality samples, large fluctuations ranging from 0.1 to 5% were seen below a certain characteristic temperature. This temperature was different for each sample, but always in the temperature span $T_c < T < 220K$. Within this span fluctuations were seen in one or more temperature regions typically about $5 - 30$K wide. Outside of these fluctuating temperature regions, the resistance fluctuations were of normal size and the data were quite clean. The observed fluctuations in the R(T) and R(time) exhibit slow dynamics with changes occurring over times on the order of seconds.

The measurements were performed using a standard 4 point method. An excitation current ranging from 10 to 100 μA was used and the current was supplied by one of several home-built, battery powered current sources. Three different current sources were used to rule out fluctuations in the current. In addition, the measurements were performed in two different cryostats, using different inserts. This was done to insure that bad wiring or some other spurious effect associated with a particular insert or system was not to blame. In total 16 nanowires were tested. Of these some were only used for measuring current-voltage characteristics (discussed in chapter 10). Of the nine nanowires on which R(T) measurements were made, six of the nanowires showed the large fluctuation behavior while three did not. However, of the three not exhibiting this behavior, two were seriously degraded with very broad transitions. All of the nanowires were similar in geometry with widths ranging from 150-250nm, and thicknesses from 50-80nm. A figure with all R(T) plots is shown in Figure 9.1 and a zoom view demonstrating the fluctuations in all is displayed in Figure 9.2. The data are scaled so an easy visual comparison can be made.

Data from the sample demonstrating these fluctuations most effectively, sample 102501-45, are shown

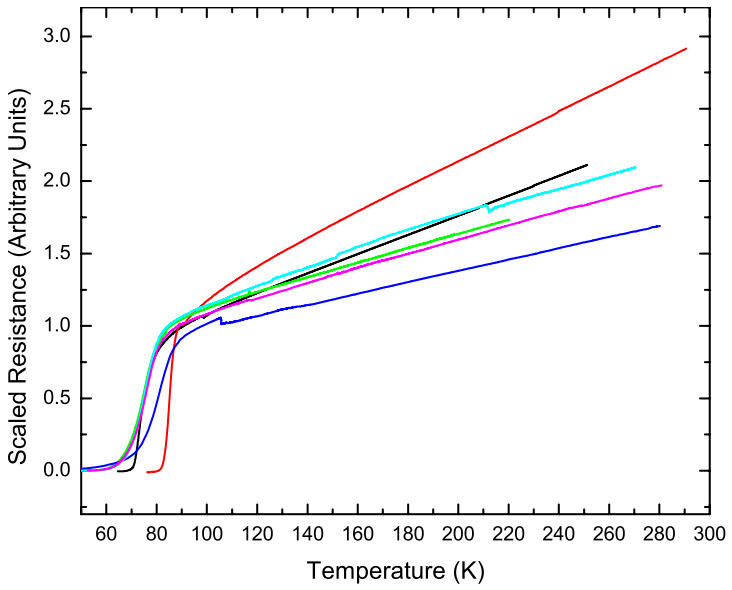

Figure 9.1: Scaled resistance vs. temperature for a series of nanowires ranging in width from 150-250nm in width.

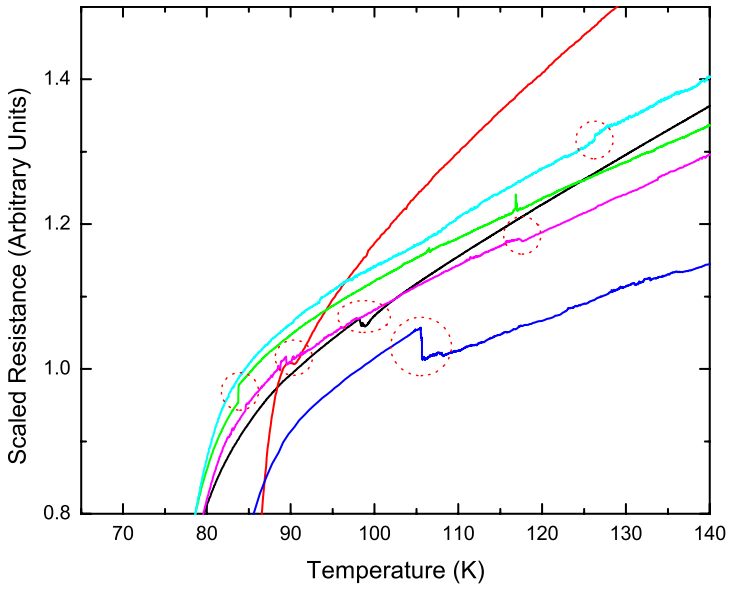

Figure 9.2: Scaled resistance vs. temperature for a series of nanowires ranging in width from 150-250nm in width.

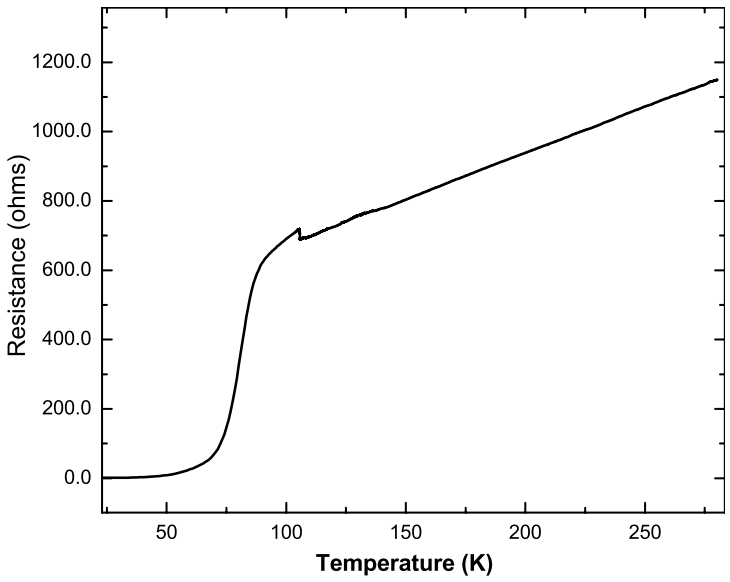

Figure 9.3: Resistance vs. Temperature for Nanowire 102501-45. Wire is 250 nm wide, 50 nm thick. Voltage lead spacing 750nm.

---

in Figure 9.3. Two different zoom views of the fluctuation region are shown in figures 9.4 and 9.5. Several key features are seen in the results in figures 9.3, 9.4 and 9.5. The resistance fluctuations are relatively small above a temperature of about 140 K. Below this temperature and down to about 100 K, the fluctuations become substantial and there is a large, 4% increase in resistance at 105 K. After this large increase there is a clear change in slope in R(T) and the signal becomes rather quiet. During the superconducting transition and below the superconducting transition the sample is very quiet. Fluctuations below T_c would be an indication that an extraneous source of fluctuations was present.

Similar features were seen in sample 022302. These results are shown in Figure 9.6. In this data run, the sample started cold and was warmed. At roughly 100 K there is a large downward jump in resistance which is just over a 1% drop. This is followed by smaller upward and downward fluctuations. Then the sample settles into a quiet state. There is a clear change in slope in R(T) before and after the large jump and fluctuation region. A zoom view of the jump, the fluctuations and the slope change is shown in Figure 9.7.

One obvious question is what happens in successive warming and cooling runs. Successive, cooling and warming runs performed on sample 102501-30. In the temperature span $T_c < T < 150K$, the warming and cooling curves are quite a bit different, and there are again large upward and downward fluctuations in the resistance. The warming run exhibited a large and sudden, $\approx 5\%$ increase in resistance at 83.5 K. A similar change was seen in the cooling run at nearly an identical temperature. The change in the cooling run isn't as

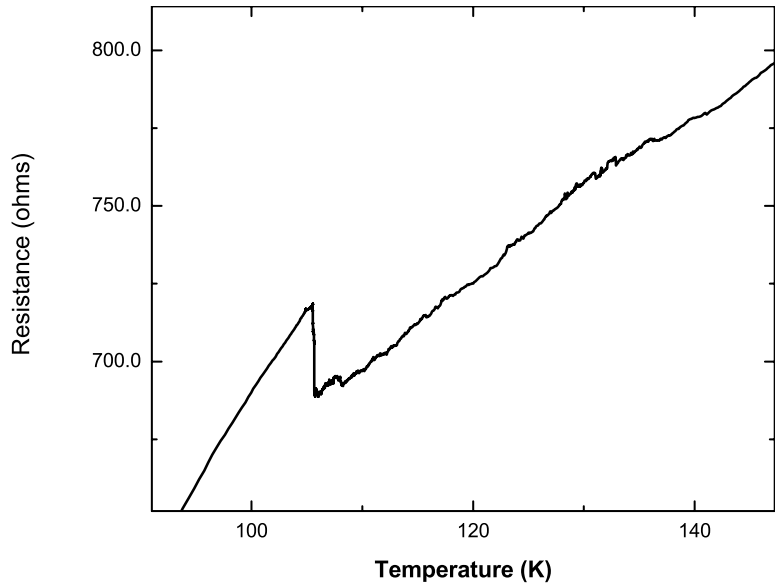

Figure 9.4: Zoom view of fluctuation region of nanowire 102501-45. Largest fluctuation is about 4%.

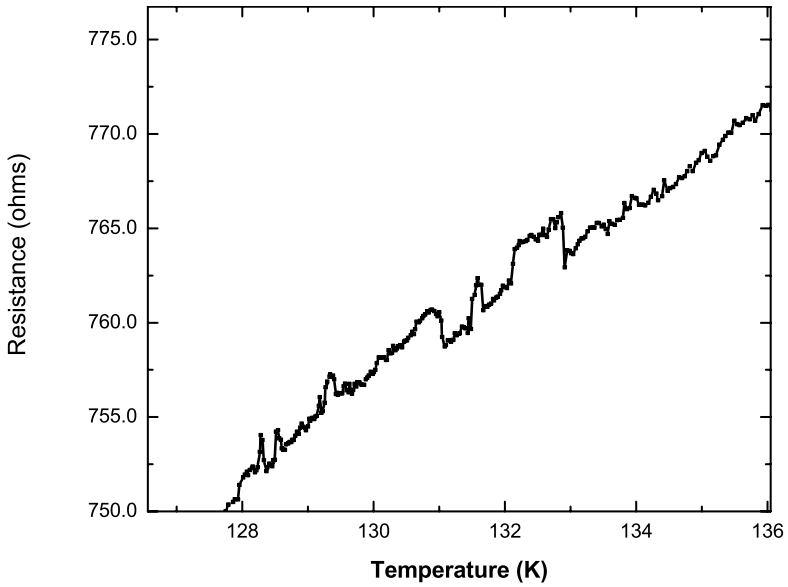

Figure 9.5: Zoom view of fluctuation region from sample 102501-45 showing the up and down switching behavior of the smaller fluctuations which are just less than 1%.

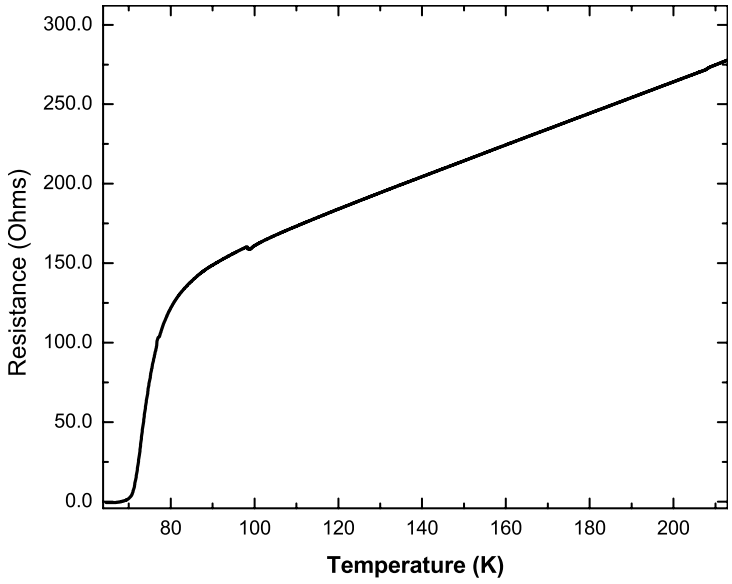

Figure 9.6: R(T) data for sample 022302 Nanowire is 200nm wide, 50nm thick. Voltage lead spacing 750nm.

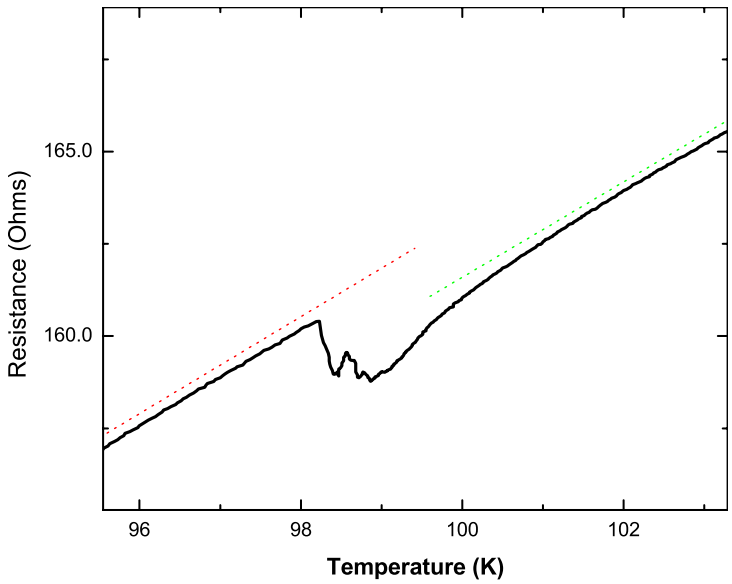

Figure 9.7: Zoom view of the large downward drop in R(T) for sample 022302. Dashed lines have been added so the slope change can be seen more easily.

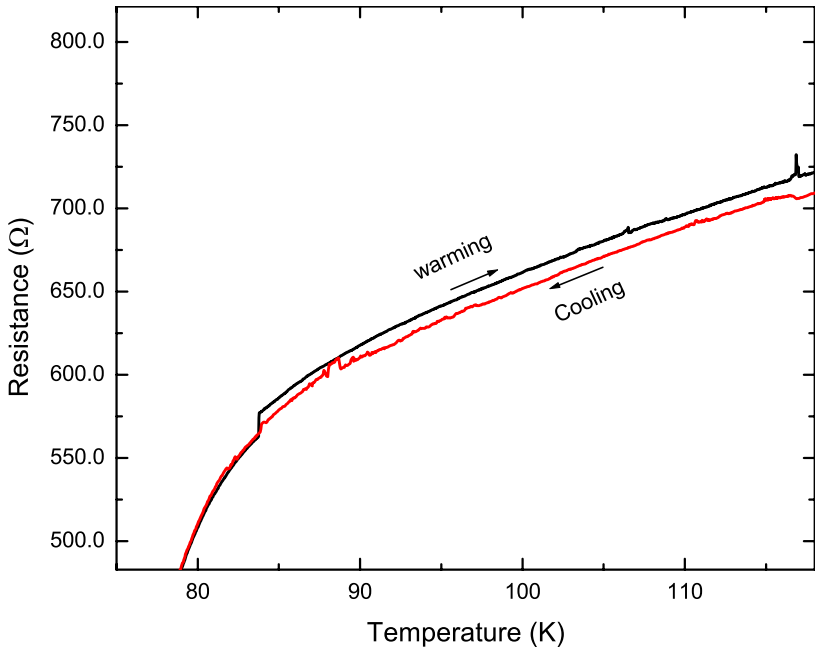

Figure 9.8: Cooling and warming R(T) data from sample 102501-30. Sample is 250nm wide, 50nm thick, with voltage lead spacing of 750nm.

large, but is definitely correlated with the feature in the warming run. The cooling run also exhibited large switches at 89 K which appear to be a competition between jumping up to the resistance state equal to that in the warming run and wanting to stay in a lower state. There is another feature at 117 K which appears in both warming and cooling runs. Finally at higher temperatures, the curves become quiet and behave normally. The R(T) curves for the warming and cooling runs are displayed on the same graph in different zoom views in figures 9.9 and 9.8.

One common question is if these fluctuations can be seen by sitting at a fixed temperature and monitoring the resistance as a function of time. For sample 022302 this was done. The temperature was held at 100 K and the resistance was monitored using a Labview program which acts like a chart recorder. Surprisingly, the resistance appears to prefer two states and is telegraph-like. However, the fluctuations are not truly telegraph noise since they have meta-stable intermediate values between the two preferred states. The two preferred states are separated by approximately 0.25%, corresponding to the switches from one of the smaller fluctuating features, not the largest jump. The dynamics is quite slow with the time spent in the meta-stable regions on the order of a second. The time trace is shown in Figure 9.10 and a histogram of the data demonstrating a bimodal (two-state) Gaussian distribution is shown in Figure 9.11.

The resolution of the voltmeter used is 1μV, amplifier noise was roughly $7nV/\sqrt{Hz}$, the Johnson noise

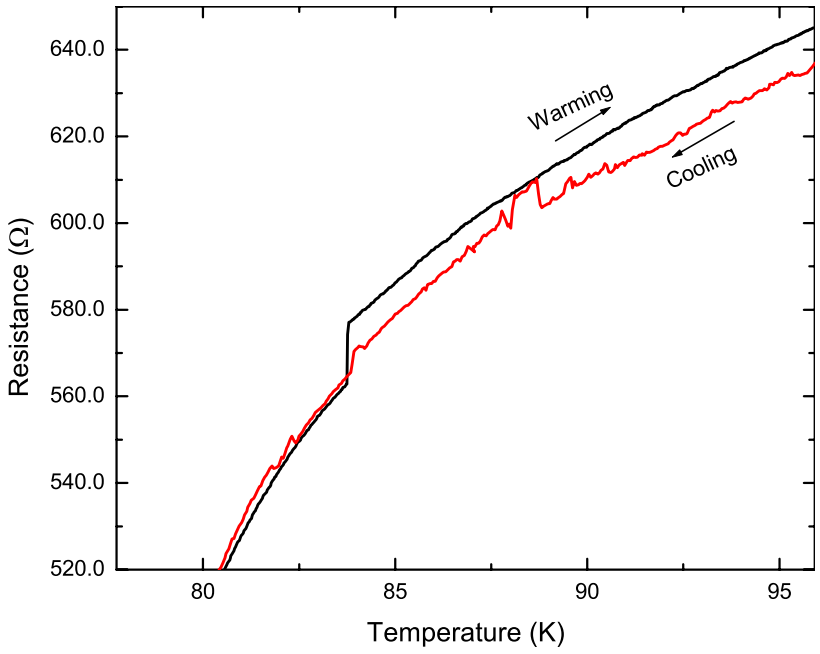

Figure 9.9: Zoom view of features in successive cooling and warming R(T) data from sample 102501-30.

for a bandwidth of 1 MHz, a resistance of 800Ω (sample + contact + lead) and temperature of 100K, is about 2μV. Finally the current noise from the current source is about $\pm 0.01\mu$A, corresponding to 1.5μV of noise. Adding these noise sources in quadrature gives a total spread of roughly 7μV, which corresponds to a spread in the resistance of about 0.07Ω. The noise within the stable regions agrees well with this value. The large fluctuations corresponding to switching between the two stable regimes are roughly an order of magnitude larger than the noise inside of the stable regimes. At higher temperatures the resistance versus time does not appear to be bimodal and exhibits fluctuations which are of normal size and in good agreement with noise estimates. The resistance versus time at 198K is shown in Figure 9.12 and the histogram demonstrating a single Gaussian distribution is shown in Figure 9.13.

It is unclear if these features have a connection with the pseudogap (PG) state. In many reports for larger samples the R(T) plots for underdoped materials show a clear change in slope at a certain temperature. As discussed in chapter 3 many researchers attribute this feature to the PG. However, there are no firm values for the PG cross-over temperature. In general we do not see a drastic change in slope in our samples except for the cases when one is seen before and after one of the large fluctuation regions. Sometimes the eye can be fooled, thus by subtracting a straight line from the data one can easily see if a change in slope or change from linearity is present. We have done this and the results are shown in Figure 9.14. These plots of R(T) in which a straight line has been subtracted indeed demonstrate a behavior which in the raw data would

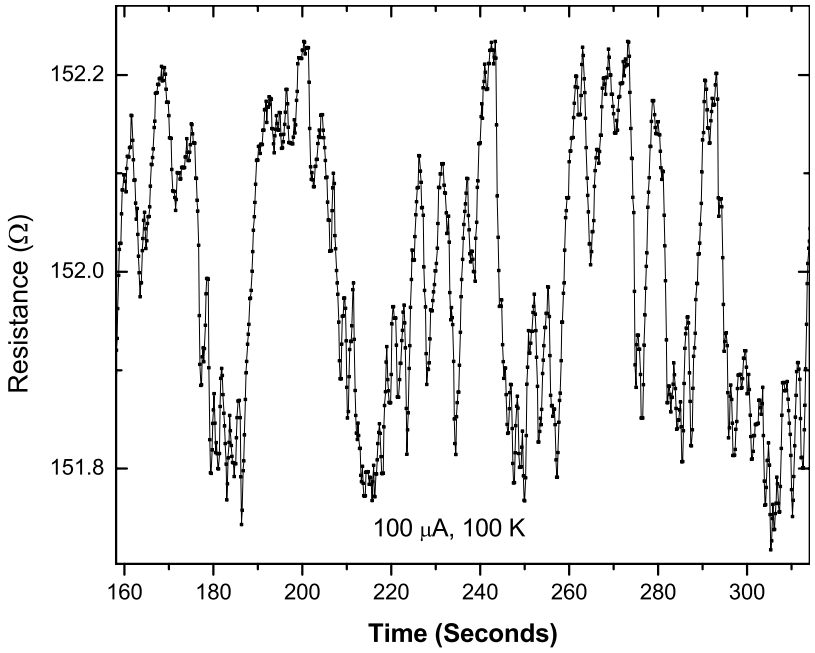

Figure 9.10: Resistance vs time of sample 022302 at 100K

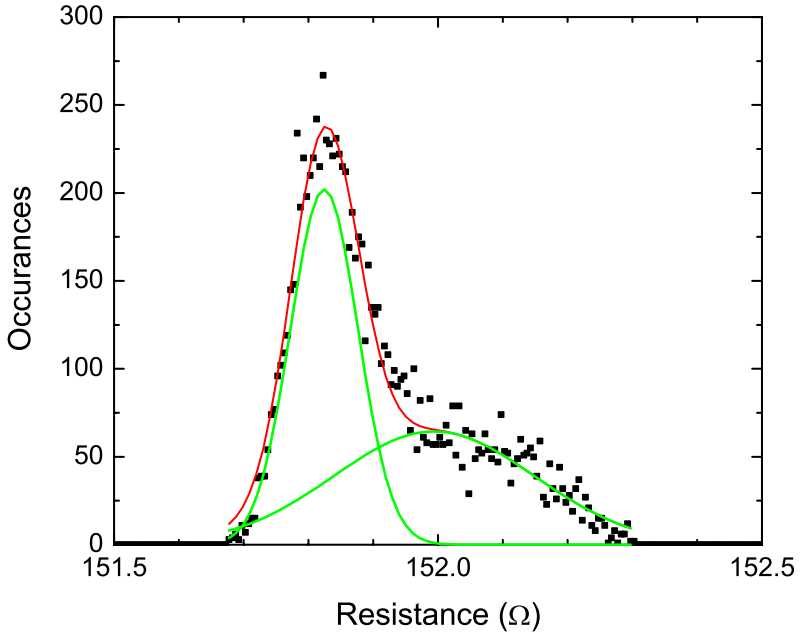

Figure 9.11: Histogram of R(time) data from sample 022302 at 100K demonstrating a bimodal Gaussian distribution.

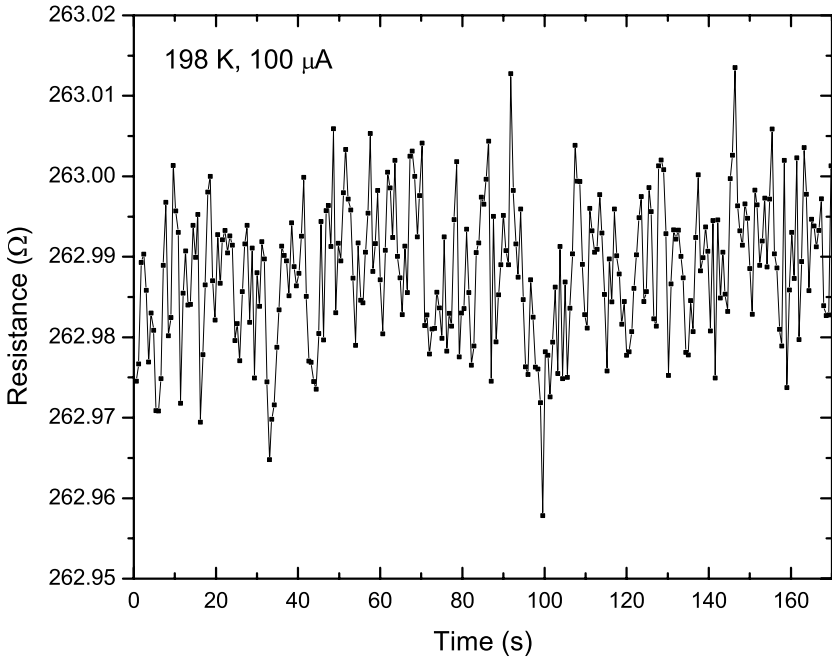

Figure 9.12: Resistance vs time of sample 022302 at 198K.

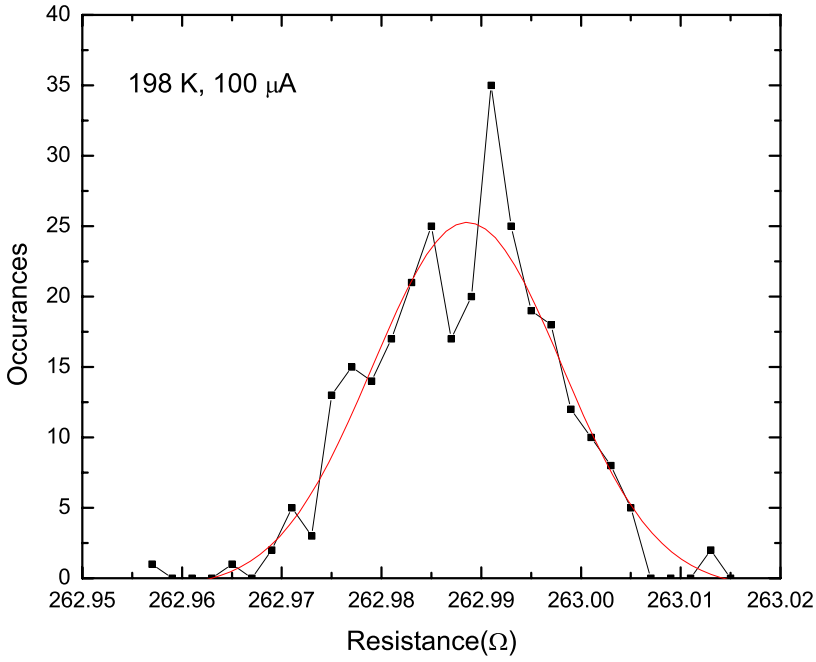

Figure 9.13: Histogram of R(time) data from sample 022302 at 198K demonstrating a single Gaussian distribution.

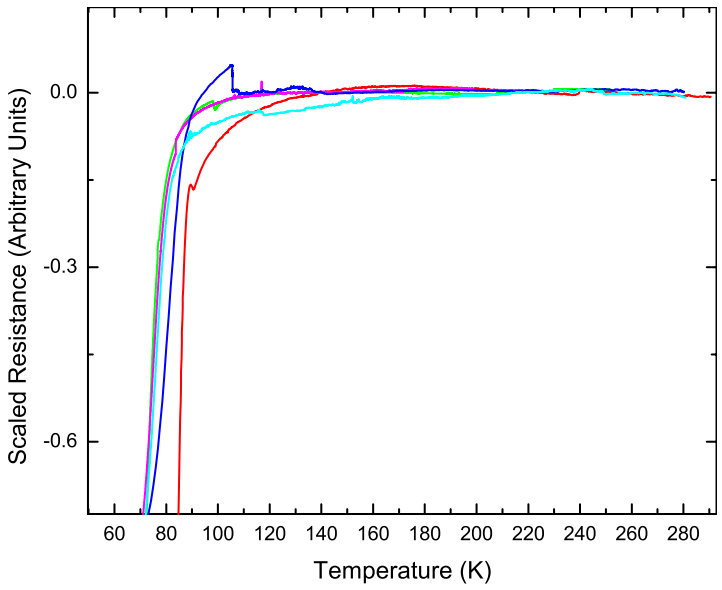

Figure 9.14: Scaled R(T) curves from several samples demonstrating a crossover behavior.

correspond to a small change in slope or change from linearity. The temperature at which this change is observed varies from 115-175K. However, we find no evidence that this crossover temperature is related to T_c. If this crossover behavior were associated with the PG one would expect higher crossover temperatures for the lowest T_c and vice versa. Since our samples are only lightly underdoped, one would expect low PG crossover temperatures compared to those seen in extremely underdoped samples. Thus the temperatures at which we observe a crossover behavior are in the correct range to be related to the PG. It is possible that the small scale nature of samples could change the R(T) behavior. It is also possible that the fluctuation features themselves and the slope changes before and after the fluctuations could be the way in which the PG manifests itself in nanoscale samples. The fluctuation features always appear in the temperature regime between the crossover and T_c. This suggests the fluctuations may have a connection with the PG.

An interesting question is whether the R(T) features seen in the nanowires are localized or whether they extend over larger distances. With sample 102501-90 two simultaneous R(T) measurements on different segments were performed. The two segments are overlapping with sizes 750nm and 8000nm. The smaller segment was measured using a 4-point measurement, while we had to settle for a 3-point measurement for the larger one. The results, shown in Figure 9.15 and in two zoom views in Figures 9.16 and 9.17 are rather amazing. The changes in R(T) have nearly perfect correlation! One thing to note about the R(T) features seen in this sample is that the first interesting feature occurs at 220K, which is roughly 100K higher than the temperatures at which features occurred in all other samples. These results, if not experimental artifact,

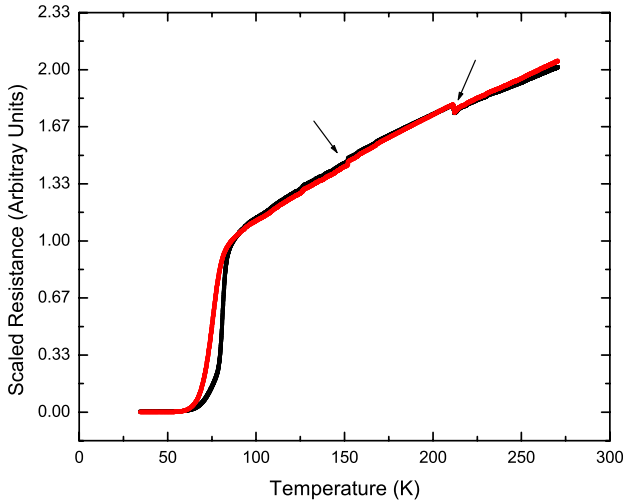

Figure 9.15: R(T) for two overlapping segments of same nanowire, sample 101501-90, showing nearly perfect correlation. Long segment is 8000nm long and varies in width from 250nm up to 3000nm. The short segment is 750nm long and 250nm wide. The data are scaled for easy comparison.

---

imply the resistance changes are correlated over distances of order 10μm. Unfortunately, due to bad luck with broken leads and equipment failure, this was the only correlated two segment R(T) data run we were able to perform except for a degraded sample showing no fluctuations.

The R(T) for wider cuprate lines has been measured by countless numbers of researchers, and to our knowledge no one has ever reported such features. As a control we've measured R(T) in some wider lines made by the same fabrication technique as that for the nanowires and we see no evidence of switching or larger than normal fluctuations. The R(T) data from a 3μm wide line is shown in Figure 9.18, and a zoom view from 90-200K is displayed in Figure 9.19.

Finally, above-T_c IVs were performed on one occasion. The IVs displayed linear, Ohmic behavior out to a current of 200μA. Fear of damaging the sample kept us from ramping further in current. Below T_c IVs were measured for numerous samples out to currents far above I_c. These results will be described in chapter 10.

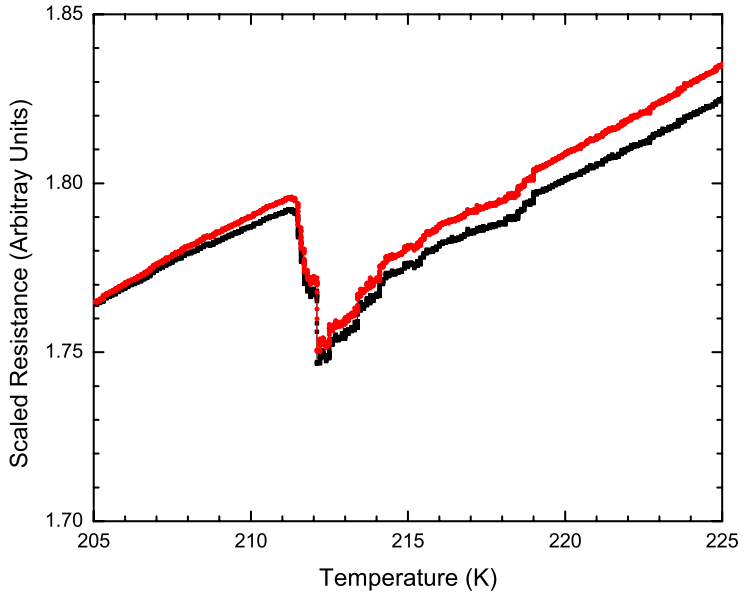

Figure 9.16: Zoom view of fluctuation feature at 220K observed in sample 101501-90. Largest change is roughly 2%.

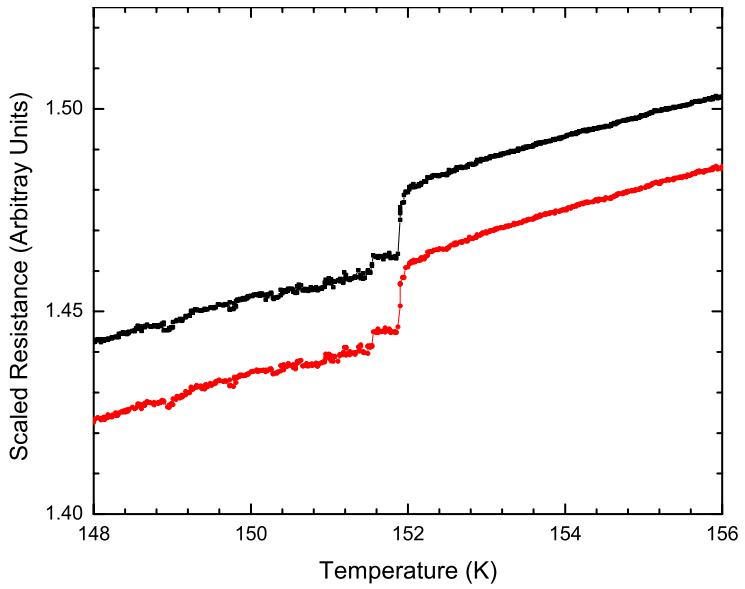

Figure 9.17: Zoom view of fluctuation feature at 150K observed in sample 101501-90. Largest change is roughly 1%.

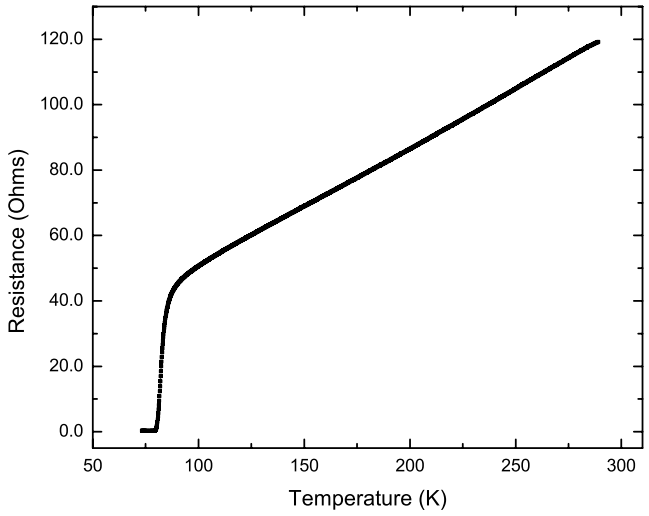

Figure 9.18: R(T) for a 3μm wide line demonstrating the absence of large resistance changes.

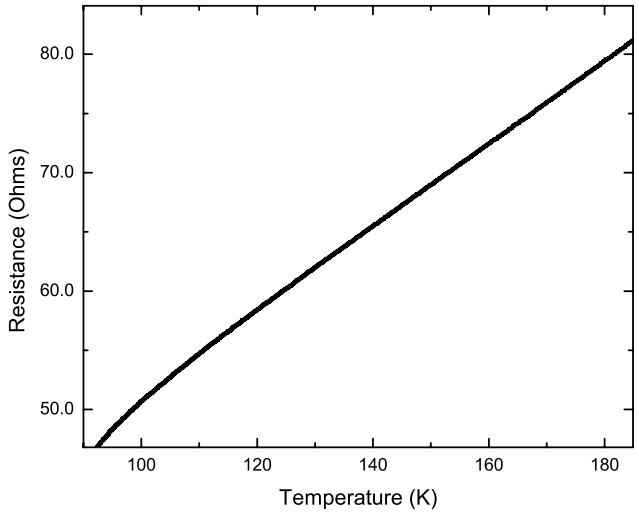

Figure 9.19: Zoom view of the temperature span in which large resistance changes would occur for a 3μm wide line

9.2 Interpretation of Data

The R(T) and R(time) results are quite difficult to explain and are not completely understood. Several possibilities will be considered. Some of these are models which are unique to cuprates while others are not.

9.2.1 Models Not Unique to Cuprates

Larger than expected resistance fluctuations have been reported in other small scale, and/or low dimensional systems. In general fluctuations become easier to observe as a sample becomes smaller, so this is no surprise. The real question becomes, are such fluctuations present in larger samples and not observable due to measurement resolution? Or does the reduced sample size change the system in such a way that such the fluctuations only exist due to the size? One such case of large resistance fluctuations is that in thin wires of Pb-In [54]. An example of the fluctuations from this work is shown in Figure 9.20.

The time dependence of the large resistance fluctuations shown in Figure 9.20 is consistent with the ideas of universal conductance fluctuations (UCF's). UCF's arise from a situation in which electron interference effects cause changes in the resistivity when electron waves scatter from local defects. However, the amplitude of the fluctuations shown in Figure 9.20 are too large to be accounted for by UCF's. The researchers who performed the measurements in Figure 9.20 are not exactly sure what is causing the fluctuations but suggest their results can be explained in terms motion of large defects such as dislocations [55].

Given such results for small Pb-In wires it is certainly conceivable that our results could also be explained by motion of dislocations or other large defects in the crystal structure. However, this is not consistent with the temperature dependence. The mobility of defects would be more likely to occur at higher temperatures. This discrepancy could possibly be explained by thermal contraction. The idea is that at some temperature the thermal contraction reaches a value allowing the dislocation or other defect to move. An important difference between the data shown in Figure 9.20 and our results is the time scale. Our fluctuations have extremely slow dynamics. The data in Figure 9.20 exhibits much faster dynamics and much shorter switching times between states. In spite of the time scale difference and different temperature behavior, the possibility of our cuprate nanowire results being explained by a type of defect motion cannot be ruled out.

9.2.2 Cuprate Specific Models

Several types of competing and/or co-existing orders have been proposed to exist in the high-T_c cuprates [43, 44, 45]. Thus it is possible our cuprate nanowire results could be explained by such ideas. One type of order that has received a great deal of attention is that of charge stripes. As described in chapter 4, the stripe

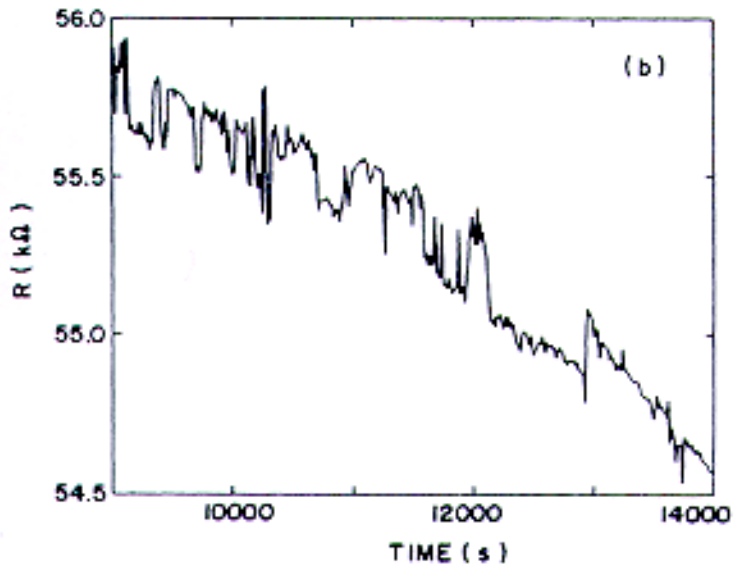

Figure 9.20: Resistance vs time for Pb-In nanowires demonstrating large resistance fluctuations, from reference [54].

---

model proposes that an electronic phase separation occurs in which the charge carriers arrange themselves into 1-dimensional channels. This model is attractive because stripes are believed to have a large resistance anisotropy. This anisotropy combined with a proposal that stripes form a micro-domain structure [56] could account for our results. In this interpretation the stripe domains may experience changes in orientation and/or size. Since they have a large anisotropy any change in the net number stripes oriented along the current flow direction would be expected to create a large resistance change. In the stripe model of high-T_c, the stripes are believed to form at the pseudogap crossover temperature, T^*. This fact would explain the observed temperature dependence of our features. Since our nanowires are only slightly underdoped, T^* is expected to be fairly close to T_c, which would be somewhere in the range 90-150K depending exactly where in the phase diagram the PG phase begins.

Recent neutron scattering data on YBCO and LSCO from two groups [47, 40] demonstrated a charge ordering or stripe correlation length. Both groups of researchers arrived at similar values which are $\approx$ 35-40nm. If these numbers and ideas are correct and they set the size scale of the domains, then our samples would be composed of a grid that is roughly 5x20 domains. The exact anisotropy value is not known, but assuming it is very large, the reorientation of one such domain would result in a resistance change of about 1%, consistent with the size of the resistance changes we observe. Explaining the correlated R(T) data on

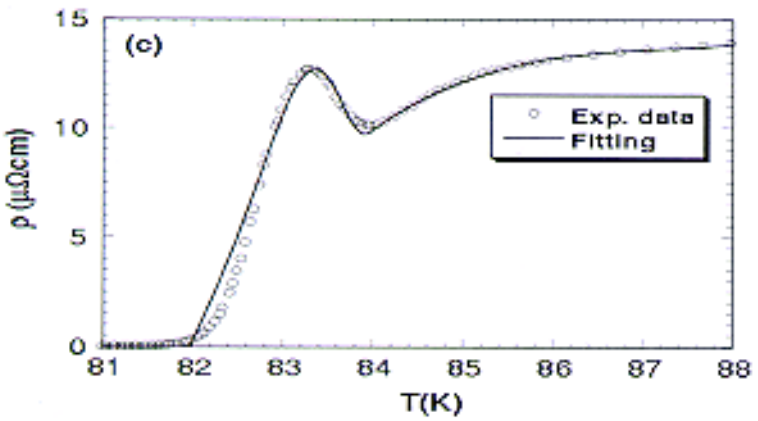

Figure 9.21: R(T) demonstrating an unexplained peak observed in the cuprates by some researchers. [57].

overlapping segments is difficult with this model. If the correlated data is not artifact, then the results imply either long domains on the edges or the possibility of very large domains in one plane being weakly coupled to those in adjacent planes.

Finally, the features we observed are somewhat similar to those from a peak producing effect observed by some in the cuprates. An example of this for YBCO is shown in Figure 9.21 from [57]. The origin of this peak is not known and is still a debatable issue. However the one important difference is that the changes in Figure 9.21 are much larger than what we observe. For instance the example shown Figure 9.21 has a 25% change whereas our changes are on the order of 1%.

Chapter 10

Current-Voltage Characteristics

10.1 The Data

The current-voltage characteristics (IVs) of the nanowires exhibit rather peculiar behavior. As the current is ramped, a voltage gradually and smoothly develops above I_c leading to a rounded, phase-diffusion-like region in the IVs. As the current is ramped further, 2 or more voltage steps are seen separated by linear regions. These steps occur when the voltage suddenly increases, at the switching current I_{sw}. When the current is ramped back down, the linear regions between the steps, and the phase-diffusion region retrace perfectly. However, the steps do not occur at the same current values and thus the step features display a strong hysteresis. The slopes of the linear regions correspond to high dynamic resistances of roughly 500Ω. However, these linear portions do not extrapolate to zero current and are thus not Ohmic. Such a non-zero extrapolation is often referred to as excess current. Excess current is often seen in Josephson junctions, but the origin of this effect is not completely understood. Examples of the step features and linear regions are shown in figures 10.1 and 10.2. A zoom view of a phase-diffusion-like region is shown in Figure 10.3. Interestingly a few of the samples measured exhibited oscillatory behavior at low voltages inside of the phase-diffusion-like region. These oscillatory features also exhibit hysteresis. An example of this is shown in Figure 10.4.

All of the IVs demonstrate that the hysteresis of the step features is highly temperature dependent with the largest hysteresis occurring at the lowest temperatures. At higher temperatures the hysteresis disappears. The switching current has the same temperature dependence as the critical current. In other words, low temperatures means a higher switching current. A plot of the critical current, I_c and first switching current, I_{sw} both versus temperature is shown in Figure 10.5. Also as shown in Figure 10.6 the IVs are symmetric with the respect to current direction, with only some slight variation in the IVs with negative current.

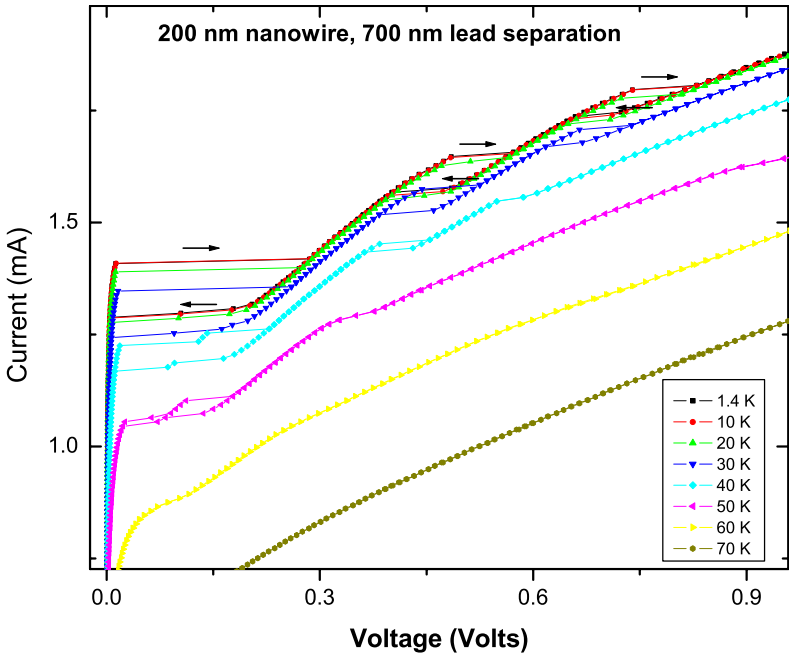

Figure 10.1: IVs at several different temperatures for a 200 nm wide, 50 nm thick YBCO nanowire. Sample 032502-30

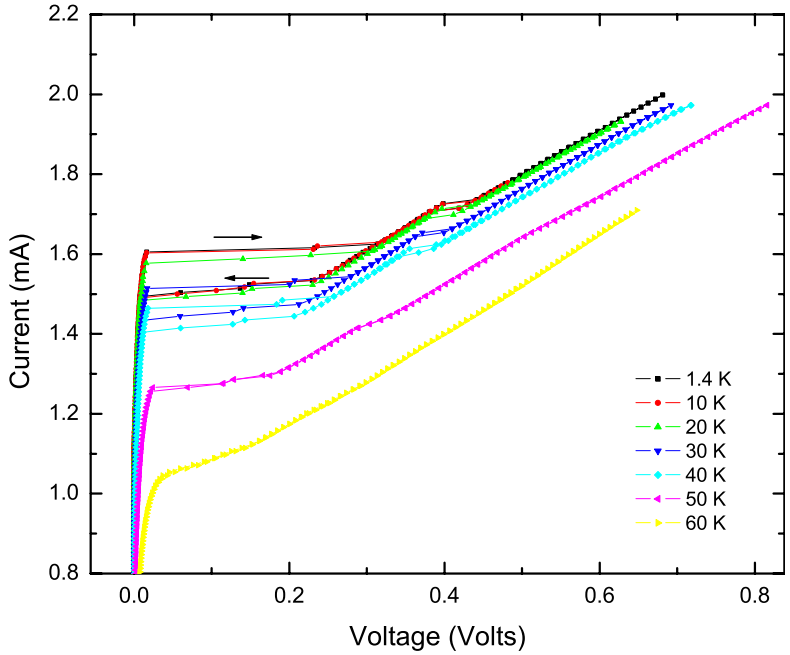

Figure 10.2: IVs at several different temperatures for a 200 nm wide, 50 nm thick YBCO nanowire. Sample 032502-0

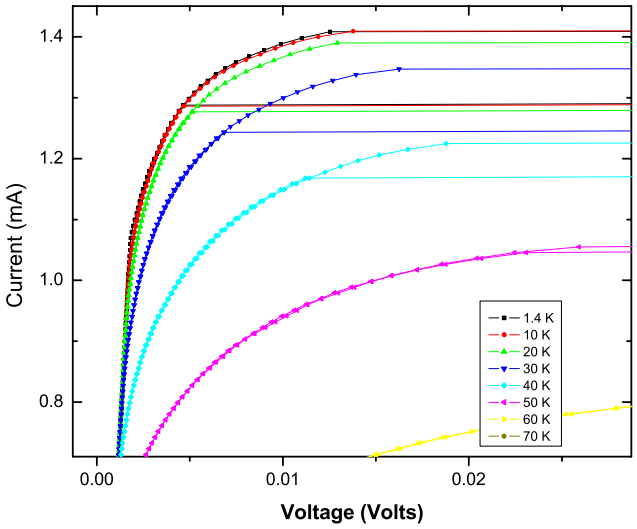

Figure 10.3: Zoom view of the low voltage portion of sample 032502-30 showing a phase-diffusion-like region.

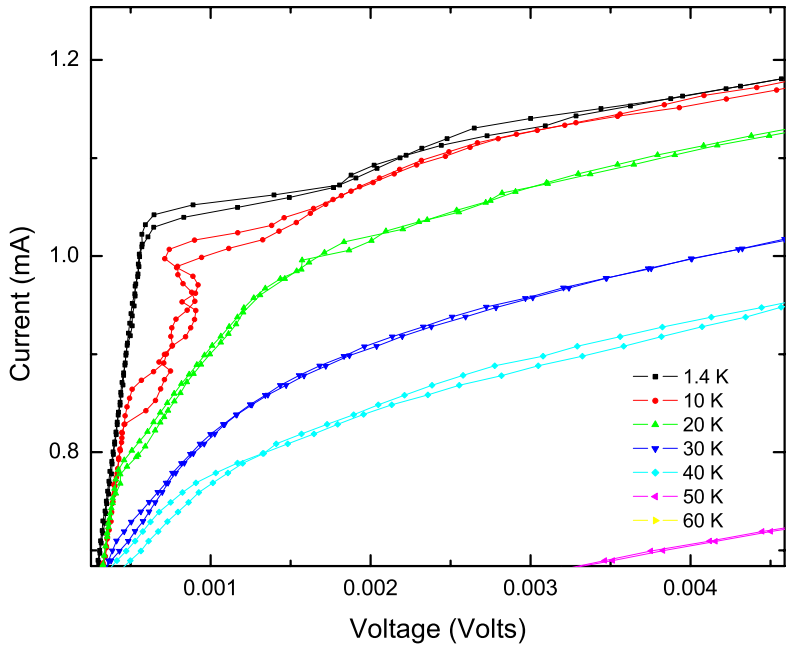

Figure 10.4: Zoom view of the low voltage portion of sample 032502-0 showing an oscillatory behavior.

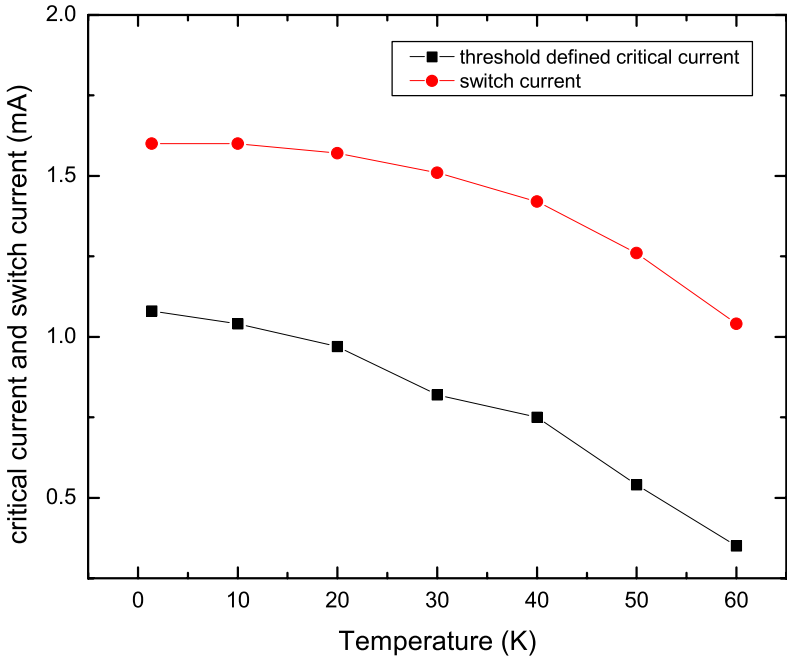

Figure 10.5: Critical current and first switching current versus temperature.

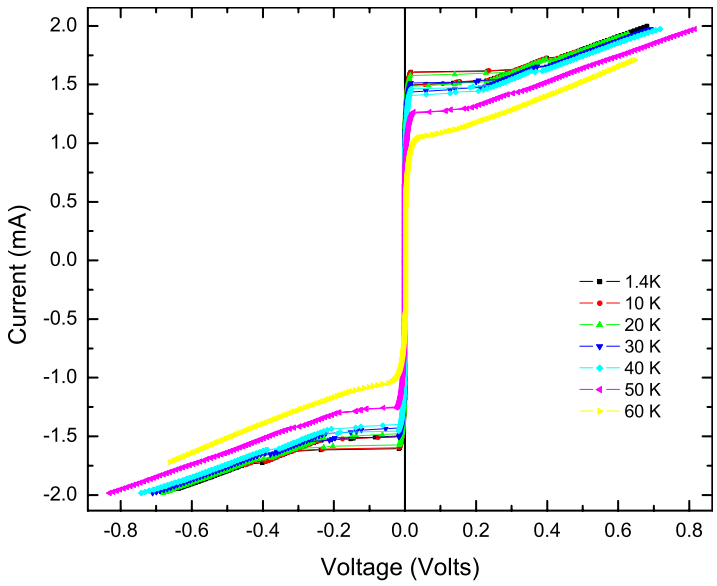

Figure 10.6: A bipolar IV showing symmetry between positive and negative current bias.

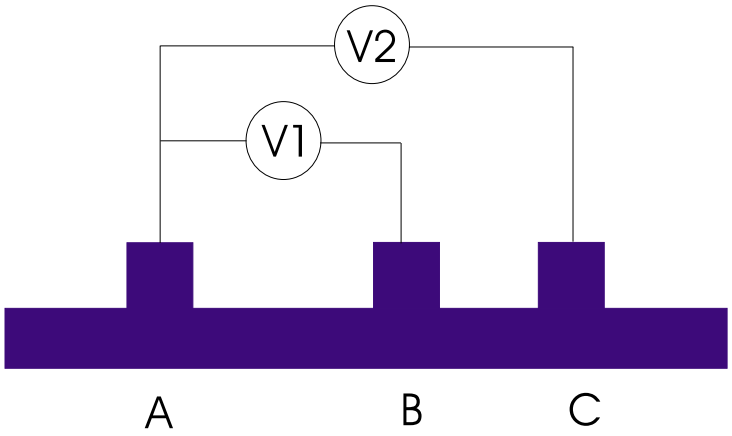

Figure 10.7: Circuit diagram for simultaneous IVs performed on overlapping segments

One question often asked is if the steps are quantized. The answer to this is no. We find no evidence of quantization of the step size. Another common question is whether dynamic resistance values between the steps increases by the same amount after each step. The answer to this is also no. The resistance values between the steps increases after each step, but not by the same amount. In a few cases, the slope after a step changed only by a very small amount.

A key issue is whether the step features are localized in just one section, or whether they extend across a sizable fraction of the nanowire. In order to answer this question simultaneous IVs of different, overlapping segments were performed. The schematic of the circuit used for this measurement is shown if Figure 10.7. The outcome of this type of measurement has 3 possibilities: (1) The step features could be from localized events occurring inside of segment AB. In this case the steps would show up in both voltage channel 1 and 2, and the size of the steps would be the same. (2) The steps features can arise from events occurring in segment BC. In this case, the step will absent in the measurement from voltage channel 1, but will show up in the measurement from channel 2. (3) The step features can be from events that extend across the sample all the way from lead A, to lead C. In this case, the steps would appear in both voltage channels, but the size of the steps would scale with length. In other words the size of the step from voltage channel 2 would be larger than that from channel 1 by the same fraction as that of the ratios of the lengths of the segments. The results from such a measurement are shown in Figure 10.8. This data shows that the steps can be from any of the 3 possibilities. The first and largest pair of steps in Figure 10.8 scale with segment length and was thus from an event that extended from lead A to C. The second pair of steps does not scale with length and was from an event localized in segment AB. Finally when the current was ramped back down a third step appeared only in voltage channel 2, which means this step was from an event localized in

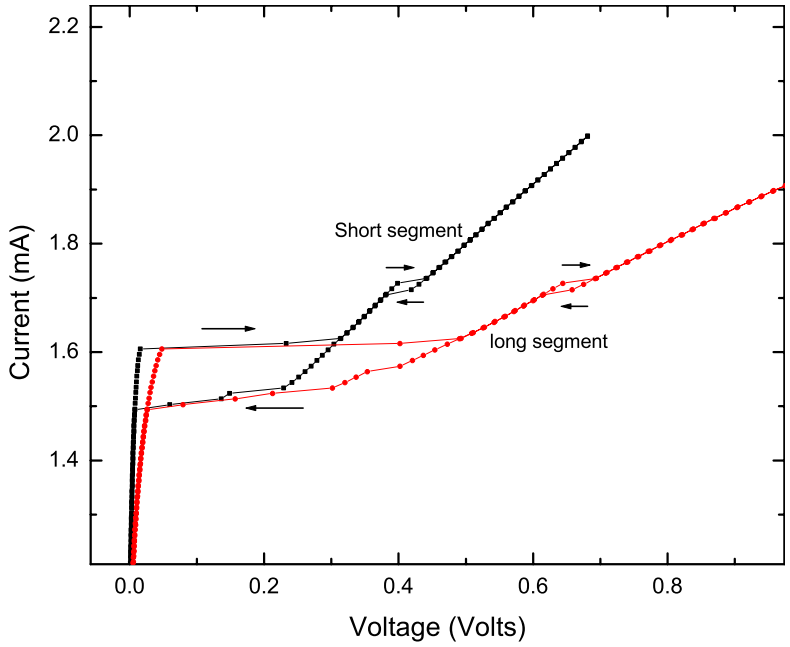

Figure 10.8: IVs of two overlapping segments of a 200 nm wide nanowire performed at 1.4 K.

segment BC. These results demonstrate that the step features occur over a length scale which ranges from less than the length of segment BC and up to the length of segment AC, corresponding to a range of lengths from $0.5 - 2.0\mu$m. Also present in these results is a case in which the step structure not only shows a hysteresis in step position, but in also structure. This can be seen by looking at Figure 10.8 and noticing that when the current is ramping down the sample re-enters the SC state by going though 2 steps, whereas the corresponding section when ramping up in current only displays one step. In addition, the extra step when ramping down is localized. Thus a localized step occurred somewhere within a region which produced a non-localized step when ramping up in current.

Some of the samples measured were of low quality as judged from the resistive transition width, and the critical current density. The low quality samples did not exhibit steps but instead had smoothly varying IVs. An example of an IV from a low quality sample is shown in Figure 10.9. This data suggests that high sample quality is a necessary ingredient for observing the steps.

Another obvious question is one of sample size dependence. Do the steps appear in wider, high quality samples, or are nanoscale samples necessary? In order to test this, samples with widths 700 and 3000 nm were made on the same chip. The 700 nm wide sample displayed steps at 1.7 K, while at the same temperature the 3000 nm wide sample made one jump to a high voltage state. Unfortunately, since the critical currents were so large, when the sample made this sudden jump in voltage, the current source could

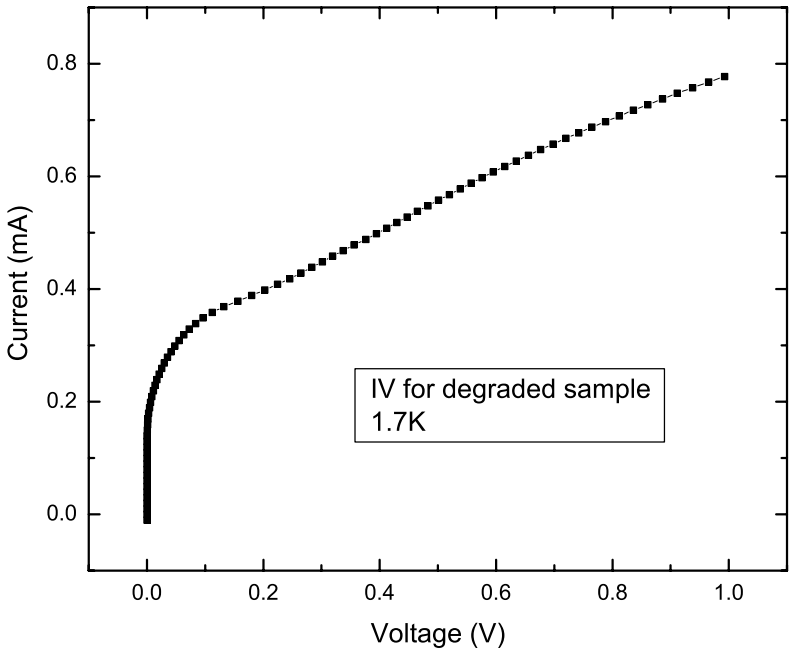

Figure 10.9: IV of a nanowire with low sample quality performed at 1.7 K. Sample does not exhibit step features.

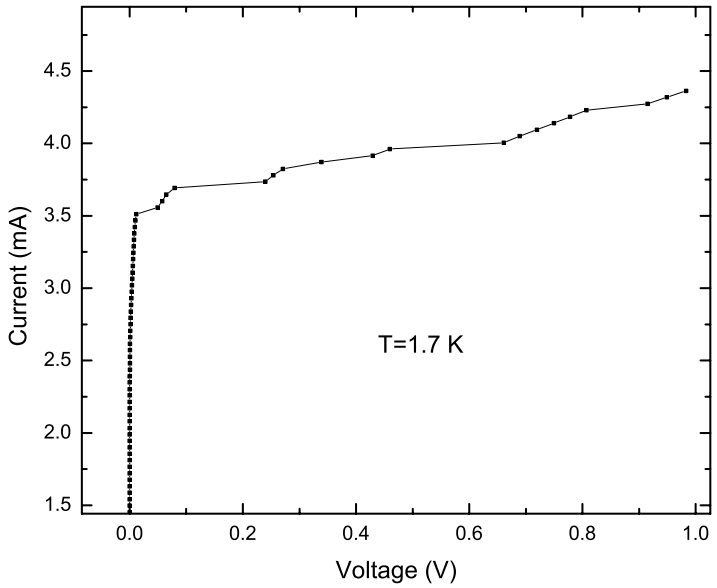

Figure 10.10: IV of 700 nm wide wire at 1.7 K exhibits steps

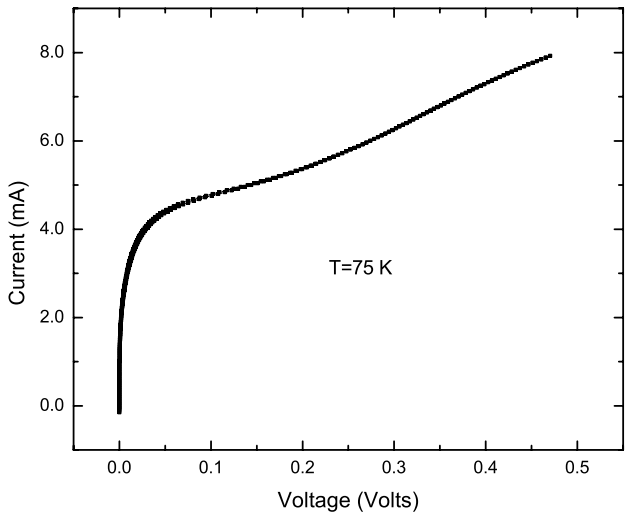

Figure 10.11: IV of 3000 nm (3μm) wide sample at 75 K does not have steps.

no longer supply enough current. However, by raising the temperature of the 3000 nm wide sample closer to T_c the critical current became low enough for the current source. In this case, at $T = 75$ K no steps were seen in the 3000nm wide sample. This result however is inconclusive since the nanoscale samples also do not have steps at temperatures close to T_c. The data from the 700nm wide sample is shown in Figure 10.10 and that from the 3000 nm wide sample in Figure 10.11.

10.2 Discussion and Interpretation of the Current-Voltage Characteristics

The nature of the IVs is rather intriguing. The presence of hysteretic steps and excess current is surprising and difficult to explain. One obvious question is why didn't the other groups who have studied narrow cuprate samples observe similar IVs. The answer is very simple. Studies by other researchers [48, 50, 52, 58] were primarily interested in the values of J_c and not the general character of the IVs. For this reason, these other researchers did not perform full IVs and thus did not ramp far enough in current to observe the hysteretic steps and the excess current. However, the regions just above I_c of my IVs are consistent with the IVs from these other groups. And except for reports of an ultra-high J_c [48], the values of my J_c's are in good agreement with those from others.

Interestingly, the IVs of Josephson junctions in series, and of nanowires made from conventional superconductors such as indium, and tin, have steps and features similar to those observed in the cuprate nanowires studied for this thesis. Therefore a good starting point for explaining the cuprate nanowire IVs is to discuss Josephson junctions and conventional superconducting nanowires. Some of the ideas used in these two contexts may be relevant. However, the cuprates are significantly different and the results cannot be fully understood using such ideas.

10.2.1 Grain Boundary Junction Models

In the resistively and capacitively shunted junction (RCSJ), tilted washboard model the above I_c behavior of a Josephson junction (JJ) is determined by whether it is overdamped or underdamped. In this model, current bias respresents the tilt of the washboard, resistance represents friction from sliding down the washboard, and capacitance represents inertia. When the tilt of the washboard (current) becomes large enough, the phase particle, is no longer trapped in one of the wells and can freely slide down the board. When the washboard is tipped back and if there were no inertia (capacitance), the particle would become trapped (zero voltage state) again once the angle was small enough. However, if there were significant inertia (capacitance) the particle would continue along the washboard even when the tilt angle becomes small (low current), and it would stop at a lower current. This effect creates hysteretic IVs. In the case of underdamped JJ's in series, one would expect multiple steps. This begs the question, can the cuprate nanowire IVs be modelled as JJ's in series?

It is not unreasonable to think JJ's could be present in the nanowires. The only common type of JJ which could be present in the nanowires are grain boundary junctions. The typical grain size for pulsed laser deposited films is roughly 500x500 nm. Since the samples studied are smaller or roughly this size, only one

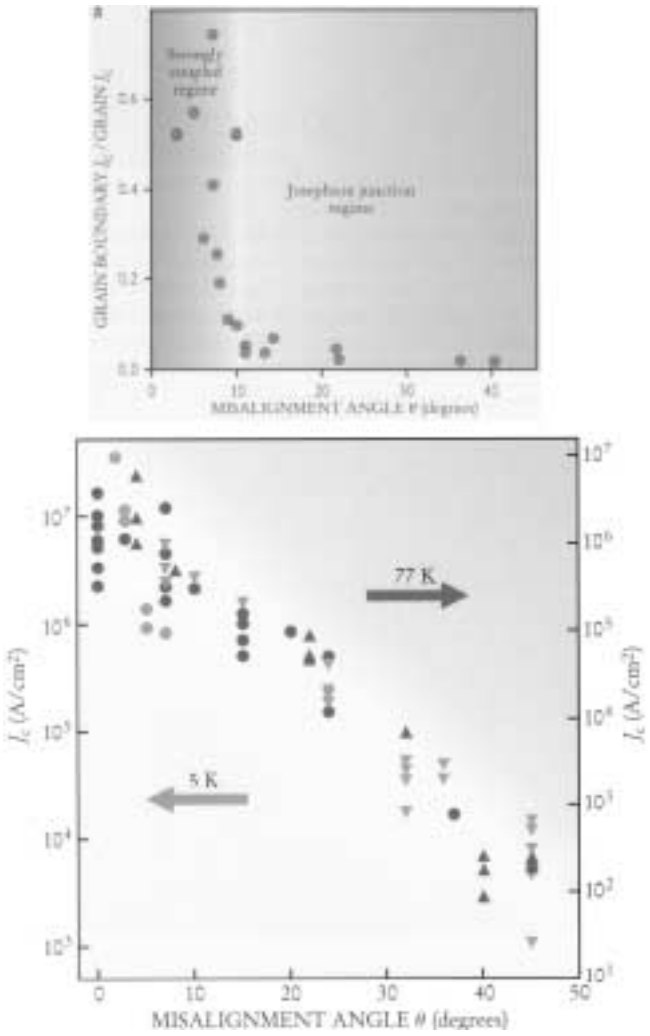

Figure 10.12: (Top) Behavior of grain boundary vs. angle showing crossover between Josephson coupling and strong coupling. (Bottom) Critical current density vs. grain misalignment angle [59].

---

to a few grain boundaries could be present. A bigger difficulty with modeling the high-T_c nanowire results in terms of grain boundary JJ's is the simple fact that the critical current densities of grain boundary JJ's are too small to account for the critical current densities observed. Mannhart et al. [59], have done an extensive study of grain boundaries JJ's in cuprates. This work has shown that if the angle between the grains is small, or if the grains are twinned, then they are not Josephson coupled but are strongly coupled. A diagram demonstrating this is shown if Figure 10.12. If grain boundaries are present between the leads of our samples then they must be very low angle or twins, meaning they would not form a Josephson junction. This must be the case since our J_c's are much too high for the presence of grain boundaries with misalignment angles large enough to create a Josephson junction.

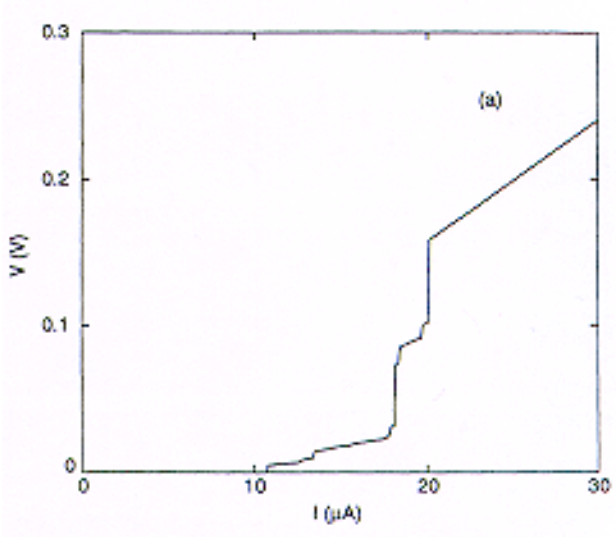

Figure 10.13: Current-Voltage Characteristics of lead-indium microbridge measured by Giordano [61].

10.2.2 Microbridge and Phase Slip Center Models

Numerous studies on narrow wires of conventional superconductors have been carried out over the years. The term microbridge refers to a narrow superconducting wire, whose width is on the order of a coherence length, that connects two larger banks of superconductor. In recent years, the term nanowire has been used instead. The studies of indium and tin microbridges by Orr [60] and the study of lead-indium microbridges by Giordano [61] have current-voltage characteristics which are strikingly similar to those of the cuprate nanowires we've measured. Representative IVs from Giordano and Orr are shown in Figure 10.13 and 10.14. (Note: the y-axis in Figure 10.13 is voltage). The strong resemblance makes it tempting to explain the features in our cuprate nanowires using ideas similar to those used for conventional microbridges.

The models for conventional SC microbridges mostly incorporate the ideas of Josephson dynamics. The starting point for many of the models is the RCSJ tilted washboard model. The basic premise is that somewhere along the length of the microbridge the order parameter fluctuates to zero creating a Josephson junction like scenario. This is equivalent to the idea of phase slip centers mentioned in chapter 5. Researchers in general agree on the interpretation of microbrigde results, but there are some disagreements on the nomenclature. Some who have studied microbridges make fine distinctions between their interpretations and the PSC idea. All of the interpretations are however quite similar. In general, samples with widths on the order of a coherence length behave as if JJ's are present.

The presence of PSC's produces IVs that are remarkably similar to those we've measured for our cuprate

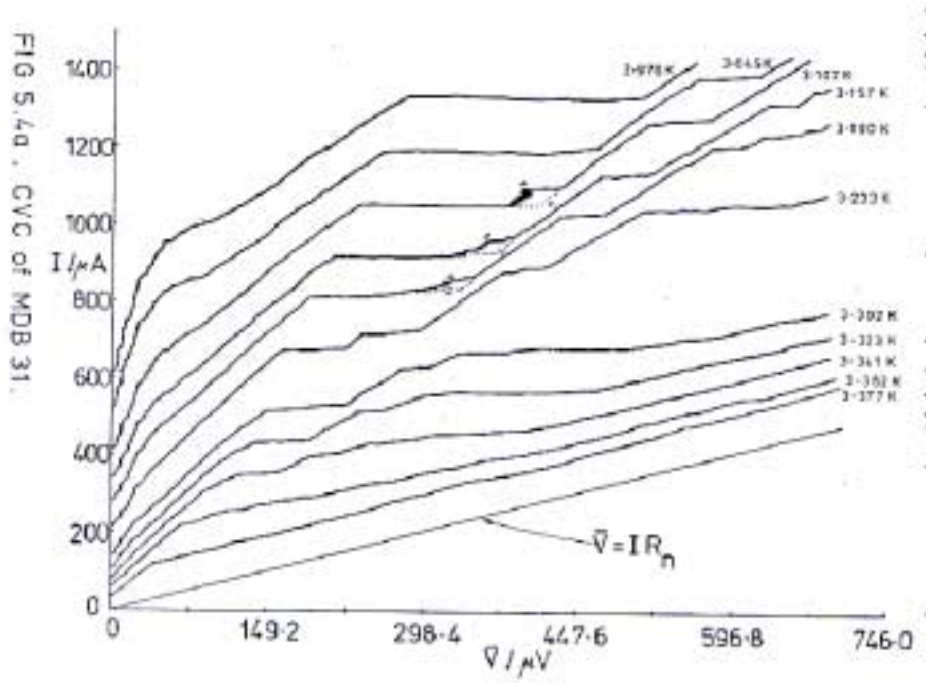

Figure 10.14: Current-Voltage characteristics of indium microbridge measured by Orr [60].

nanowires. An example of an IV exhibiting PSC's is shown in Figure 10.15. A successful model of PSC's was developed by Skocpol, Beasley and Tinkham (SBT) [46, 62] in the early $1970s$. The core of a PSC will be roughly a coherence length in width. And on both sides of the region in which the OP has fluctuated to zero, non-equilibrium quasi-particles will extend out to a distance, Λ, known as the quasi-particle diffusion length. The dynamics of the PSC occur at the Josephson frequency (typically in the GHz range). During each Josephson cycle, the OP in the core of the PSC drops to zero and each time the phase difference slips by 2π. A time averaged voltage difference, V appears across the PSC which shows up in dc IVs. This voltage is given by

$$V = 2\Lambda\rho(I - \beta I_c)/A \tag{10.1}$$

where ρ is the normal state resistivity, A is the cross sectional area of the wire, and β is a constant which is roughly $1/2$. As discussed in the previous section, the IVs for our nanowires display an excess current. It should come as no surprise that the IVs for PSC's (Figure 10.15) also display an excess current. The model by SBT naturally accounts for this excess current as can be seen in Equation (10.1). This natural explanation of excess current along with the similarities of the IVs certainly make a PSC model an attractive explanation for our cuprate nanowires. However, there are some problems associated with the idea of phase slip centers existing in our nanowire samples. The coherence length of YBCO is extremely small, $\approx$ 1nm. Thus our

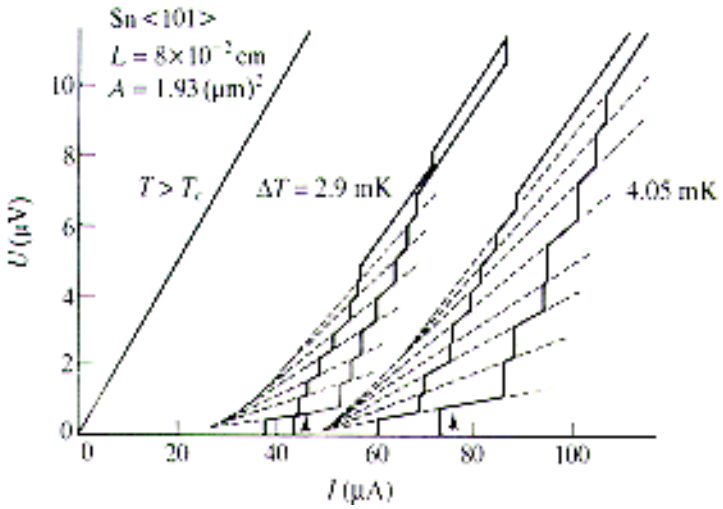

Figure 10.15: Current-Voltage Characteristics of a narrow tin whisker displaying steps created by phase slip centers. Data from Meyer et al. [63].

---

nanowires about 200 coherence lengths wide. This makes it difficult to see how PSC's could nucleate in our samples. If PSC's are present, this would imply the current distribution is non-uniform and flows along channels with widths on the order of a coherence length.

A general statement can be made concerning the presence of any type of Josephson junction (grain boundary, microbridge, PSC, etc..) by looking at the I_cR_n products of the nanowires. A well known result from Ambegaokar and Baratoff [64] states

$$I_cR_n = (\frac{\pi\Delta}{2e})\tanh(\Delta/2K_BT) \tag{10.2}$$

For low temperatures Equation (10.2) reduces to $I_cR_n = \pi\Delta/2e$. This result was originally derived for SIS junctions. For SNS junctions and grain boundary junctions, the I_cR_n products are known to be less than the ideal limit given in Equation (10.2). Interestingly, work by Kulik et al. [65] on microbridges showed that the I_cR_n can be up to 2 times greater than the ideal tunnel junction limit. The I_c's of our high-T_c nanowires range from 0.4-3mA, and the normal state resistances at low temperatures (extrapolated from R(T) curves) range between 100-500Ω. Thus the quantity I_cR_n ranges between 100-300 mV, while for YBCO $\pi\Delta/2e \approx 20$mV. Therefore we get I_cR_n products which are at least 5 times greater than the ideal limit. This fact seems at odds with modeling our nanowires as an arrangement of any type of junctions.

Given that the I_cR_n products of microbridges have been reported to be up to 2 times higher than the ideal limit, perhaps the high-T_c cuprates can have I_cR_n products that exceed the limit by an even greater amount.

This possibility coupled with that of having the current flow in narrow, coherence length sized channels, leads to an interesting explanation of our results. Such an explanation is also consistent with reports of ultra-high critical current densities discussed in chapter 8. This explanation, although exotic, accounts for the results quite well.

PSC's are generally believed to be localized. However, there are some suggestions that the nucleation of one PSC could cause other ones to nucleate nearby [66]. This sort domino effect of one PSC producing others could possibly explain the non-localized behavior from the simultaneous IVs shown in Figure 10.8.

The ideas of Josephson coupling are also relevant when discussing certain models of high temperature superconductivity. The stripe model as discussed in chapter 4, consists of narrow conducting channels "stripes" in which current flows. When the stripes Josephson couple the entire sample behaves superconducting. In addition recent STM evidence [41] shows a phase separation of the electronic structure into hole-rich and hole-depleted regions. The size scale of the hole-rich regions reported in this work were on the order of 3-5nm which are the correct size to produce phase slips centers. Such results suggest that Josephson coupling between hole-rich domains might always be at play even for structurally perfect samples. Or that the supercurrent flows in a percolative manner going from hole-rich region to hole-rich region.

10.2.3 Joule Heating

When dealing with nanoscale samples, the issue of heating is a very important, often troubling, and sometimes confusing issue. An analysis of power input and cooling needs to be performed to ensure Joule heating is not so significant that it creates a problem. In many cases the heating of small samples can be a problem because the samples are fabricated on insulators such as glass which have extremely bad thermal conductivities. Luckily the substrates incorporated for our nanowires have quite a good thermal conductivity even at very low temperatures. The substrates used for all of the nanowires were lanthanum aluminate, $LaAlO_3$. The thermal conductivity of $LaAlO_3$ was measured for the first time by Morelli [67] in 1992. His measurements were performed from room temperature down to 10K. The thermal conductivity of $LaAlO_3$ at 10 K is roughly $20 W m^{-1} K^{-1}$, which is similar to that of some metals such as lead. The choice of substrate for high-T_c films has to meet several requirements and for most applications good thermal conductivity is not one of these requriements. $LaAlO_3$ meets all of the typical requirements and is a commonly used substrate for high-T_c materials. It is rather fortunate that $LaAlO_3$ also has a good thermal conductivity. This makes it a great substrate for high-T_c nanowires. The thermal conductivity of the nanowire material, YBCO, is nearly the same as that of $LaAlO_3$. This allows for a very simple model of the heat flow in the nanowire/substrate system. The model is one of heating a rod of cross sectional area A at one end. The heating at the end in

this case is from the current supplied to the nanowire. The one dimensional heat flow equation states,

$$dQ/dt = -\kappa A \frac{\partial T}{\partial z} \tag{10.3}$$

where dQ/dt is the heat flow per unit time (the power input), κ is the thermal conductivity, and A is the cross sectional area across which the heat flows, and $\frac{\partial T}{\partial z}$ is the temperature gradient.

In this model, a very reasonable assumption is made that the substrate temperature is the same as that of the bath. In the case of the substrate and copper stage sitting in superfluid liquid helium, this temperature corresponds to 1.4 K. This is the lowest temperature at which IVs were performed. Since the nanowire has nearly an identical thermal conductivity, it is reasonable to treat the nanowire as just a small surface feature of the substrate. In other words applying current to the nanowire is equivalent to dumping heat into a localized spot on the substrate surface. If the nanowires are being driven above T_c by Joule heating, then a large temperature gradient between the nanowire and substrate would need to exist. Equation (10.3) can be used to calculate the temperature gradient needed for a known power input.

The slopes of the linear sections between steps in the IVs correspond to resistances of roughly those seen at room temperature or higher. If the temperature of the nanowire were sitting at room temperature while the substrate was at 10K, then a temperature difference of 300 K exists over some distance, which will be estimated using Equation (10.3). The power input is known simply from looking at the IVs. The power input of interest is that which is being supplied just when the first step occurs. Looking at Figure 10.3 shows the power input at the switching current is $1.4mA$x$14mV \approx 20\mu$W. The area of the nanowire making contact to the substrate is roughly 200 nm x 2μm (or 4x10$^{-13}m^2$), and the thermal conductivity of the nanowire and substrate at 10 K are both roughly $20Wm^{-1}K^{-1}$. Using Equation (10.3) and these numbers shows that the temperature gradient would be 2.5K/μm. If the IVs are to be explained by sections becoming normal, then a temperature difference between the nanowire and a spot deep inside the substrate would need to be 300 K. Using the calculated temperature gradient, shows that the substrate temperature would be at 297.5K at a depth of 1μm below the surface, 295K at a depth of 2μm , and so forth. Thus the substrate would not reach the base temperature of 10K until a depth of roughly 120μm below the surface. This depth is about $1/4$ of the substrate thickness. Since the substrate has a fairly good thermal conductivity, and is well thermally anchored to the copper stage, it is hard to imagine such a large temperature gradient could exist within the substrate. Another way to approach this problem is to make a reasonable guess at what depth below the nanowire the temperature has reached the bath temperature. One guess at this number would be the depth at which the heat flow becomes three dimensional instead of one dimensional. This should occur at a depth of roughly one width of the nanowire, or 200 nm. If we use 5 times the width for the depth at which the

temperature of the substrate should be at bath temperature, this is 1μm. This gives a temperature gradient of 300K over 1μm. Plugging this number into Equation (10.3) shows that the power required to maintain such a temperature gradient is a little less than 2.5mW, which is two orders of magnitude greater than input power of 20μW supplied at the first step. This model underestimates the total cooling power. The direct cooling of the nanowire from the bath (sometimes superfluid helium) is not accounted for. Also the nanowire itself is a small section of a larger cuprate film. Thus the heat flow out of the nanowire into the larger portions of the cuprate film have not been included in this estimate.

A thermal contact resistance between the nanowire and substrate could be added into the estimate. However, the cuprate films are deposited onto the substrate at high temperature and are epitaxial. Thus the crystal structures of the cuprate and substrate are strongly bound and form a seamless boundary in terms of thermal conductivity. In general thermal boundary resistance is determined by how well the phonon spectra are matched . Since the cuprates are grown epitaxially on very well matched lattices, the thermal boundary resistance is small. The thermal boundary resistance between cuprate film and substrate has been measured by a few researchers [68, 69, 70] and has been found to be negligible. This is a distinctly different scenario than that in which an amorphous metal is deposited onto a glass substrate, as is the case for conventional microbridges.

Multiple steps exist in the IVs between linear regions. These linear regions have high dynamic resistance of roughly 500-800Ω. If these resistances were due to sections being normal, then a large temperature gradient would need to exist inside of the nanowire itself. In other words, if after the first step a section were truly normal, then other sections must still be superconducting since more steps occur later. This would require a gigantic temperature gradient of a few hundred Kelvin over a distance of a few hundred nanometers. Also if the linear sections were due to truly normal sections then they should not retrace and they should extrapolate to zero. The IVs clearly show that the linear portions retrace, and that the slopes do not extrapolate to zero.

Finally, an experimental verification demonstrating that heating is not significant comes from the degraded IV shown in Figure 10.9. The power input into this sample is similar to that in the high quality samples, yet the degraded sample shows no steps.

In light of the numerous arguments presented here, it seems unlikely that heating could be causing the features in the IVs. However, it is certainly possible that some factor has not been taken into account and that the heating could be more significant than estimated. The calculation of cooling power was deliberately underestimated for this reason.

10.2.4 Vortex Flow

The motion of vortices inside of a superconductor creates a voltage across the sample in accordance with Faraday's Law. When vortices move they create an effective electric field, E, which is given by

$$\mathbf{E} = \mathbf{B} \times \mathbf{v_{ff}} \tag{10.4}$$

where $\mathbf{B}$ is the magnetic field penetrating the sample, and $\mathbf{v_{ff}}$, is the vortex velocity. It is conceivable that at some threshold current, vortices nucleated at the edge could suddenly jump across the sample once they became depinned. Such a flux avalanche would produce hysteretic voltage-steps in the IV. Also if different sections along the nanowire experience such a flux avalanche at different currents, then multiple steps would occur. These ideas also account nicely for the observation that some of the voltage steps are localized while others are not.

However, a quick analysis of the actual numbers involved, shows such a flux avalanche cannot account for the voltage steps. Vortices rushing across the sample would create an electric field given by Equation (10.4). This electric field is known from measurements and is simply the size of the voltage step divided by the lead spacing. This number gives an electric field of $300\frac{mV}{\mu m}$. The self field at the edge using an Ampere's Law estimate is about 2mT. Even if a magnetic field an order of magnitude higher than this estimate is put into Equation (10.4), one can show that in order to generate an electric field of $300\frac{mV}{\mu m}$, the speed of the vortices would need to be on the order of the speed of light. Given these numbers it seems unlikely vortex flow could be the cause of the steps.

Equation (10.4) and a frictional damping term from vortex motion can be used to derive an expression for the effective resistivity due to flux flow. This is called the flux flow resistivity, ρ_{ff}, and is given by

$$\rho_{ff} = \frac{B}{H_{c2}}\rho_n \tag{10.5}$$

where ρ_n is the normal state resistivity, H_{c2} is the upper critical field and B is the applied field. Since H_{c2} of the cuprates is enormous (> 100T), and since the applied field in our case is a small self field, the resistance due to flux flow will be a tiny fraction of the normal state resistance.

10.2.5 Models Unique to Cuprates

Some of the models discussed so far could possibly explain our cuprate nanowire results. However these models all seem to have problems or seem to fail in some way. This leaves open the possibility the results may be unique to the cuprates.

There are numerous proposals that coexisting and/or competing order parameters are present in the high-T_c cuprates [43, 44, 45]. Such OP's would presumably form domain structures. One such idea that has attracted considerable interest is the stripe model [33]. As mentioned in chapter 9, Mook et al. [47] and Lake et al. [40] have independently observed evidence for stripes using neutron scattering. One group measured YBCO and the other LSCO. Both observed an ordering effect and both concluded their results were suggestive of stripes. In addition both were able to measure a charge ordering, or stripe correlation length. Their results show this correlation length, ζ is $\approx 35 - 40$nm. Therefore the width of our YBCO nanowires ranges from $3 - 6\zeta$. Interestingly a recent theoretical paper [56] was able to show that stripes should break up into a micro-domain structure with domain sizes ranging from a few nanometers to "long range". This proposed domain size is consistent with those measured by Mook and Lake [47, 40]. Given the large amount of evidence for the existence of stripes, and the nature of our samples it is reasonable to interpret our nanowire results in terms of stripe domains.

There are many open questions concerning stripes. Perhaps the most important two questions are: Are stripes detrimental or beneficial to superconductivity? And, can static stripes coexist with superconductivity or must they fluctuate?

The first theoretical proposals of stripes in doped antiferromagnets viewed the stripes as insulating [34, 71, 72]. However many experiments demonstrate otherwise. For instance, in non-superconducting LSCO where the stripes are ordered and separated by ≈ 35nm the material exhibits metallic behavior [73, 74, 75]. In addition static stripes are known to coexist with superconductivity. In fact, in the LCO family static stripes are present even at the highest T_c [76, 77]. Static stripes also coexist in other superconductors but only in certain doping levels. For instance, there is evidence static stripes coexist with superconductivity for underdoped YBCO with a T_c of 39K. These results only show it is possible for static stripes to coexist with superconductivity. However, in some materials the onset of static stripes has been shown to decrease T_c leading to the idea that static stripes are detrimental to superconductivity. It has been proposed [78] that static stripes are good for pairing, while fluctuating stripes are good for Josephson coupling and weaken pairing. Thus the fluctuating versus static question may have a complex, material-dependent answer. It has also been proposed [79] that in cases in which stripes are believed to be fluctuating, that what is needed experimentally is some way to slow down or stop the stripe dynamics. Nanoscale samples with widths on the order of the purported stripe domain size [47, 56] may be a way to accomplish this goal. If this is true, then our results would indicate that stripe dynamics can be slowed by geometrical constraint, and that superconductivity can still exist given such constraint.

The evidence for stripes from numerous experiments is overwhelming. Even for the material we have

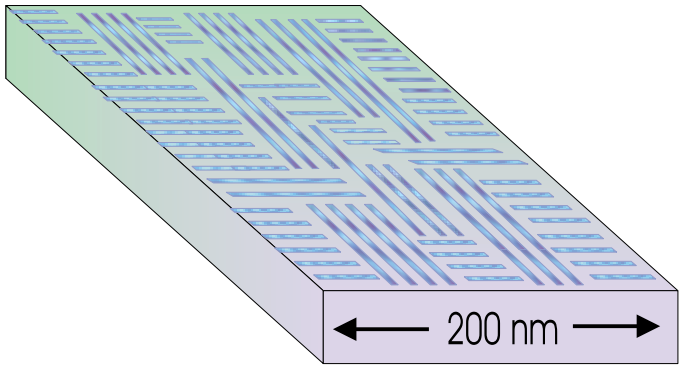

Figure 10.16: Artist's conception of stripe domains

studied a large body of evidence exists (see chapter 13 of reference [78]). Thus it is hard to imagine that the stripes would not play a role in determining the nature of our nanowires given the purported size scales. It is possible that in our nanowires the stripes have been artificially pinned. However we do not know if this is the case. The answer to this question is vital for any type of modeling of our nanowires in terms of stripe domains. For this reason we have begun developing two models, one for each case.

In the case of static domains we have developed a model in which the domains perpendicular to supercurrent flow behave as SIS Josephson junctions. The justification for this is that the regions between stripes are composed of insulating AF material. Thus it is natural to model them as such. The stripe domains parallel to current flow are modelled simply as narrow superconducting channels with higher critical current than the perpendicular domains. It is interesting to note that the parallel domains would be consistent with the ideas mentioned earlier about phase slip centers since in this case the supercurrent would be flowing in a region of reduced width. A schematic diagram of the proposed domains is shown in Figure 10.16.

We have created a simple 1D simulation of the nanowires based on stripe domains which generates IVs that agree qualitatively with the data. One dimensional in this case means each domain extends across the entire nanowire width. This model naturally produces excess current and steps and by extending the model to 2 or 3 dimensions we feel we could account for the non-local behavior seen in some steps. The diagram and results for the 1D model are shown in figures 10.17 and 10.18. Figure 10.17.

As mentioned it is not known whether in our case the stripe domains are static. If they are not then the above model would not apply and a different approach would be needed. If the stripe domains are not static in the superconducting state we envision that for currents below I_c the stripes are fluctuating. When the current gets large enough, the stipes become static or severely slowed, killing the superconductivity. This crystallization of stripes would be expected to occur more easily along the edges of the sample since near

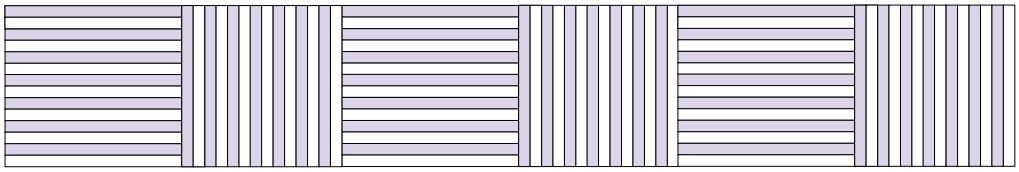

Figure 10.17: A nanowire composed of 1D stripe domains

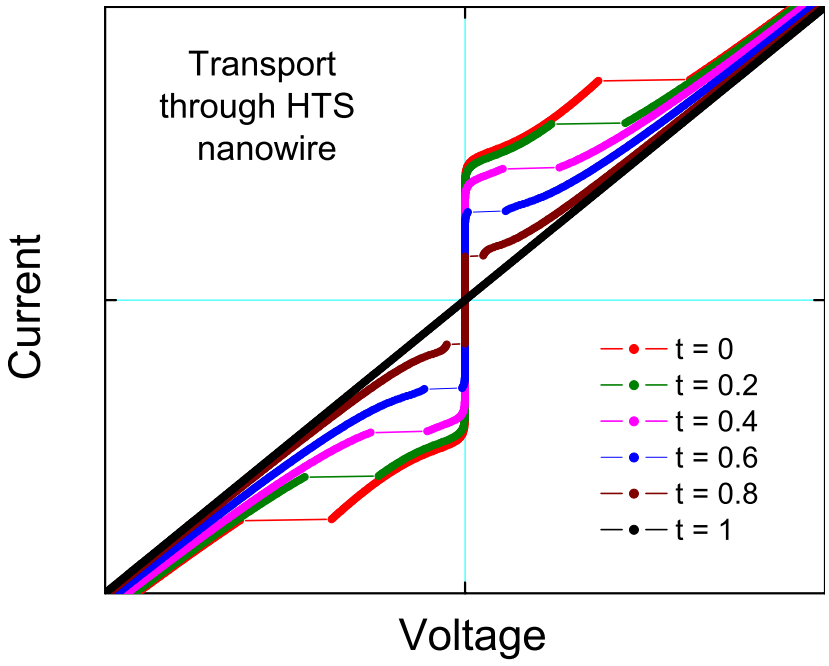

Figure 10.18: Simulated IV from 1D stripe domain model

the edge the rotation of a stripe domain would be more difficult. Such an edge effect accounts for the results from the simultaneous IVs performed on overlapping segments in Figure 10.8. In this model, the stripes at the edge crystallize first, creating the first big step which scales with length (delocalized event). At a higher current the stripes in the middle crystallize forming the remaining steps. The hysteresis is accounted for simply by the stripes melting at slightly different currents from those at which they freeze. Such a model involving fluctuating stripe domains is also not inconsistent with the percolative current flow model proposed earlier. If the stripe domains are fluctuating, perhaps the current flow is restricted to flow only on domains which have a certain orientation. Thus the supercurrent meanders across the sample always finding the best domain through which to flow.

The proposed stripe domain explanations are based on models of high-T_c superconductivity which are still being developed, as are all other high-T_c models. For this reason, no strong claims about the validity of such models can be made. However, the idea of stripes or other domain structure dynamics accounting for our results seems to qualitatively account for the features rather naturally.

Another mysterious feature seen in some of our nanowires is an oscillatory behavior (Figure 10.4) in the low voltage part of the IVs. This could simply be caused by noise. However, the features seem to onset at a certain temperature. It is difficult to explain how the features could be noise given such a temperature dependence. An explanation of this result eludes us at present and may require some aspect unique to the cuprates.

Chapter 11

Conclusions and Future Work

11.1 Conclusions

A major component of this thesis was developing the technique for fabricating the high-T_c nanowires. This took nearly 2 years of research and development. Several key steps were discovered to be necessary. These are: The dual use of a carbon layer as a buffer and milling mask, cooling with liquid nitrogen during ion milling, baking the electron beam resist at reduced temperatures, and finally, ion milling at reduced voltages and currents.

Our measurements on YBCO nanowires provide a direct way to probe the electronic structure and transport on a mesoscopic length scale. Although the results may possibly be explained in terms of models not unique to the cuprates, all such models and ideas seem to fail in some way. This leaves open the possibility of the results being unique to high-T_c nanowires and explainable only in terms of high-T_c concepts. One such concept which our results tend to support is that of coexisting orders and their associated domain structures. In particular the results seem to fit the idea of charge stripe domains quite well. It should be pointed out that the concept of stripe domains accounts for the results in the R(T), R(time) and the IV data quite naturally. Anytime a model can account for numerous behaviors and different types of measurements its likelihood of being correct is enhanced. Therefore we feel it is reasonable to conclude our results are a possible signature of stripe domains. In order to resolve these issues and further explore this area we have proposed several experiments to be carried out in the near future by myself and one of the new students in the group.

11.2 Future Work and Experiments

One of the parameters we would like to adjust and study is doping. By systematically varying the doping and performing similar measurements a strong doping dependence may be discovered. The reasons this hasn't been done already are two fold. Creating overdoped YBCO films by pulsed-laser deposition (PLD) is not easily done or perhaps not possible. Thus the only thing which can possibly be done using PLD made films is to go to very low doping. However low doping has difficulties as well. The fabrication process itself de-oxygenates the samples to a certain degree. However if the starting film is too far underdoped then only a small decrease in oxygen results in the sample losing its superconducting properties. The reason for this can be seen by remembering the superconducting state in the cuprate phase diagram is shaped like a dome. If the processing is begun with a starting film on the steep part of the dome then the nanowire will likely not be superconducting. One way to solve this problem is to use cation doping. This can be realized by using MBE grown films. Therefore one of the future projects will be performing similar experiments using MBE grown BSCCO films. This will be a collaborative effort with the MBE films coming from Professor Jim Eckstein's group and the measurements performed by the Van Harlingen group. Not only will this provide a way to systematically control the doping, it will provide a different material to study.

Another avenue we wish to explore is magnetic field dependence. We plan to perform a very well controlled study as a function of magnetic field. In addition to simply studying the field strength dependence a study of the field orientation would likely provide much insight. Results from field angle dependence of YBCO single crystals suggests it is possible to align stripes with large magnetic fields [80]. In these single crystal results the resistance changes on the order of 1% when the current is aligned versus being parallel to the field direction. This effect may be larger if a similar experiment is done with a nanoscale sample.

Finally, we have plans to carry out what we call the high-T_c nanodot experiment. This will be a direct test for resistance anisotropy. The idea is to fabricate a dot as small as possible with eight leads allowing for two, $4-$point measurements in orthogonal directions to be carried out simultaneously. The cross-correlation spectrum of the resistance fluctuations will be measured using a 2-channel spectrum analyzer. Three possible results can be obtained. The fluctuations could be correlated, uncorrelated, or anti-correlated. Correlated fluctuations would be indicative of isotropic behavior while anti-correlated would suggest the rotation or resizing of anisotropic domains. Uncorrelated fluctuations would be a null result and would likely indicate the dominate noise source was not coming from the sample. A schematic diagram of the experimental setup is shown in Figure 11.1.

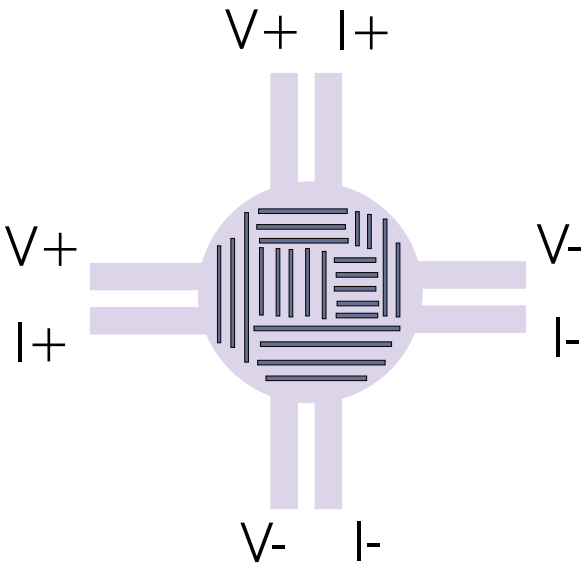

Figure 11.1: Schematic for nanodot cross correlation experiment

List of References

[1] H. K. Onnes, Commun. Phys. Lab. Univ. Leiden **124c**, 1 (1911).

[2] W. Meissner and R. Ochsenfeld, Naturwissenschaften **21**, 787 (1933).

[3] J. Bardeen, L. N. Cooper, and J. R. Schrieffer, Phys. Rev. **108**, 1175 (1957).

[4] V. L. Ginzburg and L. D. Landau, Zh. Eksp. Teor. Fiz. **20**, 1064 (1950).

[5] B. D. Josephson, Phys. Rev. Lett. **1**, 251 (1962).

[6] J. G. Bednorz et al., Z. Phys. **64**, 189 (1986).

[7] N. E. Bickers, D. J. Scalapino, and S. R. White, Phys. Rev. Lett. **62**, 961 (1989).

[8] P. Monthoux, A. V. Balatsky, and D. Pines, Phys. Rev. Lett. **67**, 3448 (1991).

[9] P. Monthoux and D. Pines, Phys. Rev. Lett. **72**, 1874 (1994).

[10] D. A. Wollman, D. J. VanHarlingen, W. C. Lee, D. M. Ginsberg, and A. J. Leggett, Phys Rev. Lett. **71**, 2134 (1993).

[11] C. C. Tsuei et al., Phys. Rev. Lett. **73**, 593 (1994).

[12] H. Takagi, Phys. Rev. B. **40**, 2254 (1989).

[13] I. Giaever, Rev. Mod. Phys **46**, 245 (1974).

[14] C. Renner et al., Phys. Rev. Lett. **80**, 149 (1998).

[15] W. W. Warren et al., Phys. Rev. Lett. **62**, 1193 (1989).

[16] R. E. Walstedt et al., Phys. Rev. B. **41**, 9574 (1990).

[17] T. Timusk and B. Statt, Rep. Prog. Phys. **762**, 61 (1999).

[18] B. O. Wells et al., Phys. Rev. B **46**, 11830 (1992).

[19] Z.-X. Shen et al., Phys. Rev. Lett. **70**, 3999 (1993).

[20] M. Randeria and J. C. Campuzano, Condmat **9709107**, 1 (1997).

[21] A. G. Loeser et al., Science **273**, 325 (1996).

[22] H. Ding et al., Nature **382**, 51 (1996).

[23] H. Takagi et al., Phys. Rev. Lett. **69**, 2975 (1989).

[24] T. Ito et al., Phys. Rev. Lett. **70**, 3995 (1993).

[25] M. Randeria, Condmat **9710223**, 1 (1997).

[26] V. J. Emery and S. A. Kivelson, Nature **374**, 4347 (1995).

[27] M. Suzuki and T. Watanabe, Phys. Rev. Lett. **85**, 4787 (2000).

[28] V. M. Krasnov et al., Phys. Rev. Lett. **84**, 5860 (2000).

[29] R. A. Klemm et al., Physica C **341-8**, 1663 (2000).

[30] P. W. Anderson, Science **235**, 1196 (1987).

[31] A. Paramekanti, M. Randeria, and N. Trivedi, Phys. Rev. Lett. **87**, 217002 (2001).

[32] R. B. Laughlin, Condmat **0209269**, 1 (2002).

[33] V. J. Emery and S. A. Kivelson, Phys. Rev. B **56**, 6120 (1997).

[34] J. Zaanen and O. Gunnarson, Phys. Rev. B **40**, 7391 (1989).

[35] J. Zaanen, Science **286**, 251 (1999).

[36] S. A. Kivelson, E. Fradkin, and V. J. Emery, Nature **393**, 550 (1998).

[37] S. Truggman, Phys. Rev. B. **37**, 1597 (1988).

[38] J. P. Eisenstein, Solid State Commun. **117**, 123 (2001).

[39] N. Ichikawa et al., Phys. Rev. Lett. **85**, 1738 (2000).

[40] B. Lake et al., Nature **415**, 299 (2002).

[41] K. M. Lang, V. Madhavan, J. E. Hoffman, E. W. Hudson, H. Eisaki, S. Uchida, and J. C. Davis, Nature **415**, 412 (2002).

[42] A. J. Millis, H. Monien, and D. Pines, Phys. Rev. B **42**, 167 (1990).

[43] S. Chakravarty et al., Phys. Rev. B **63**, 094503 (2001).

[44] D. A. Ivanov et al., Phys. Rev. Lett. **34**, 3958 (2000).

[45] Q. Wang et al., Phys. Rev. Lett. **87**, 7004 (2001).

[46] W. Skocpol, M. R. Beasley, and M. Tinkham, J. Low Temp. Phys. **16**, 145 (1974).

[47] H. A. Mook, P. Dai, and F. Dogan, Phys. Rev. Lett. **88**, 097004 (2002).

[48] H. Jiang et al., Phys. Rev. Lett. **66**, 1785 (1991).

[49] I. Zaquine et al., J. of Appl. Phys. **72**, 270 (1992).

[50] P. Larsson et al., J. Vac. Sci. Technol. B **18**, 25 (2000).

[51] H. Assink et al., IEEE Trans. Appl. Supercond. **3**, 2983 (1993).

[52] S. Tahara et al., Phys. Rev. B **41**, 11203 (1990).

[53] T. P. Orlando, *Foundations of Applied Superconductivity*, Addison-Wesley, 1991.

[54] N. Giordano and E. R. Schuler, Phys. Rev. B **41**, 11822 (1990).

[55] V. M. Vinokur and S. P. Obukhov, Sov. Phys.-JETP **68**, 126 (1989).

[56] S. J. L. Billinge and P. M. Duxbury, Phys. Rev. B **66**, 064529 (2002).

[57] M. M. Abdelhadi, Cond-mat **0206007**, 1 (2002).

[58] M. J. M. E. deNivelle et al., Phys. Rev. Lett. **70**, 1525 (1993).

[59] J. Mannhart et al., Physics Today **54**, 48 (2001).

[60] P. Orr, PhD thesis, Cambridge University, 1979.

[61] N. Giordano, Phys. Rev. B **43**, 160 (1991).

[62] M. Tinkham, *Introduction to Superconductivity, 2nd Edition*, McGraw-Hill, 1996.

[63] J. D. Meyer and R. Tidecks, Solid State Comm. **24**, 639 (1977).

[64] V. Ambegaokar and A. Baratoff, Phys. Rev. Lett. **10**, 486 (1963).

[65] I. O. Kulik and A. N. Omel'yanchuk, trans. Sov. J. Low Temp. Phys. **3**, 459 (1978).

[66] J. D. Meyer and R. Tidecks, Solid State Comm. **24**, 643 (1977).

[67] D. Morelli, J. Mater. Res. **7**, 2492 (1992).

[68] G. L. Carr et al., Appl. Phys. Lett. **57**, 2725 (1990).

[69] M. Nahum et al., Appl. Phys. Lett. **59**, 2034 (1991).

[70] C. G. Levey et al., Appl. Phys. Lett. **60**, 126 (1992).

[71] H. J. Schulz, J. de Physique **50**, 2833 (1989).

[72] K. Machida, Phyica C **158**, 192 (1989).

[73] Y. Ando et al., Phys. Rev. Lett **88**, 137007 (2002).

[74] M. Matsuda et al., Phys. Rev. B **62**, 9148 (2000).

[75] A. N. Lavrov, Phys. Rev. Lett. **87**, 017007 (2001).

[76] B. O. Wells et al., Science **277**, 1067 (1997).

[77] Y. S. Lee et al., Phys. Rev. B **60**, 3643 (1999).

[78] E. W. Carlson, V. J. Emery, S. A. Kivelson, and D. Orgad, Cond-mat **0206217**, 1 (2002).

[79] S. A. Kivelson, Private Communication (2002).

[80] Y. Ando et al., Phys. Rev. Lett **83**, 2813 (1999).

Vita

Joseph Anthony Bonetti was born in Rock Hill, SC on February 3, 1974. In 1993 he entered the Georgia Institute of Technology (Georgia Tech) in Atlanta, GA and graduated with highest honors in June of 1996 with a B.S. degree in Physics. He immediately began his graduate studies at the University of Illinois, supported as a teaching assistant until he joined the research group of Professor Dale Van Harlingen in the Spring of 1997. He initially worked on an applied physics project involving high-T_c micro-coils for the use in microscopic nuclear magnetic resonance imaging. Joseph later decided on a more fundamental project and began investigating high-T_c nanowires. In 2000, Joseph received his M.S. degree in physics and in 2002 was awarded the Center for Nanoscale Science and Technology Fellowhsip. Since 1999, Joseph has given presentations of his work at many scientific conferences, including the International Conference on Low Temperature Physics in Hiroshima, Japan in 2002.

After completing the Ph.D. program at the University of Illinois, Joseph will continue his studies in condensed matter physics as a postdoctoral research associate at the California Institute of Technology (Caltech) working in the area of 2D electron gases with Professor Jim Eisenstein.